



Buckling of high-strength steel beams

Author:

Le, Tuan

Publication Date:

2020

DOI:

<https://doi.org/10.26190/unsworks/21836>

License:

<https://creativecommons.org/licenses/by-nc-nd/3.0/au/>

Link to license to see what you are allowed to do with this resource.

Downloaded from <http://hdl.handle.net/1959.4/66847> in <https://unsworks.unsw.edu.au> on 2024-04-29

BUCKLING OF HIGH-STRENGTH STEEL BEAMS

by

Tuan Manh Le



A thesis submitted as partial fulfilment of
the requirements for the degree of

DOCTOR OF PHILOSOPHY

School of Civil and Environmental Engineering
The University of New South Wales
Sydney, Australia

October 2019

COPYRIGHT STATEMENT

I hereby grant the University of New South Wales or its agents the right to archive and to make available my thesis or dissertation in whole or part in the University libraries in all forms of media, now or here after known, subject to the provisions of the Copyright Act 1968. I retain all proprietary rights, such as patent rights. I also retain the right to use in future works (such as articles or books) all or part of this thesis or dissertation.

I also authorise University Microfilms to use the 350 word abstract of my thesis in Dissertation Abstract International.

I have either used no substantial portions of copyright material in my thesis or I have obtained permission to use copyright material; where permission has not been granted, I have applied/will apply for a partial restriction of the digital copy of my thesis or dissertation.

Signed

Date09/10/2019.....

AUTHENTICITY STATEMENT

I certify that the Library deposit digital copy is a direct equivalent of the final officially approved version of my thesis. No emendation of content has occurred and if there are any minor variations in formatting, they are the result of the conversion to digital format.

Signed

Date09/10/2019.....

ORIGINALITY STATEMENT

I hereby declare that this submission is my own work and to the best of my knowledge it contains no materials previously published or written by another person, or substantial proportions of material which have been accepted for the award of any other degree or diploma at UNSW or any other educational institution, except where due acknowledgement is made in the thesis. Any contribution made to the research by others, with whom I have worked at UNSW or elsewhere, is explicitly acknowledged in the thesis.

I also declare that the intellectual content of this thesis is the product of my own work, except to the extent that assistance from others in the project's design and conception or in style, presentation and linguistic expression is acknowledged.

Signed

Date09/10/2019.....

INCLUSION OF PUBLICATIONS STATEMENT

UNSW is supportive of candidates publishing their research results during their candidature as detailed in the UNSW Thesis Examination Procedure.

Publications can be used in their thesis in lieu of a Chapter if:

- The student contributed greater than 50% of the content in the publication and is the “primary author”, ie. the student was responsible primarily for the planning, execution and preparation of the work for publication
- The student has approval to include the publication in their thesis in lieu of a Chapter from their supervisor and Postgraduate Coordinator.
- The publication is not subject to any obligations or contractual agreements with a third party that would constrain its inclusion in the thesis

Please indicate whether this thesis contains published material or not.

- This thesis contains no publications, either published or submitted for publication (if this box is checked, you may delete all the material on page 2)*
- Some of the work described in this thesis has been published and it has been documented in the relevant Chapters with acknowledgement (if this box is checked, you may delete all the material on page 2)*
- This thesis has publications (either published or submitted for publication) incorporated into it in lieu of a chapter and the details are presented below*

CANDIDATE’S DECLARATION

I declare that:

- I have complied with the Thesis Examination Procedure
- where I have used a publication in lieu of a Chapter, the listed publication(s) below meet(s) the requirements to be included in the thesis.

Name	Signature	Date (dd/mm/yy)
Tuan Le		09/10/2019

<p>Postgraduate Coordinator's Declaration (to be filled in where publications are used in lieu of Chapters)</p> <p>I declare that:</p> <ul style="list-style-type: none"> • the information below is accurate • where listed publication(s) have been used in lieu of Chapter(s), their use complies with the Thesis Examination Procedure • the minimum requirements for the format of the thesis have been met. 		
<p>PGC's Name</p> <p>Dr. Mitchell Harley</p>	<p>PGC's Signature</p>	<p>Date (dd/mm/yy)</p> <p>04/10/2019</p>

For each publication incorporated into the thesis in lieu of a Chapter, provide all of the requested details and signatures required

Details of publication #1:						
<i>Full title:</i> RESIDUAL STRESSES IN WELDED HIGH-STRENGTH STEEL I-BEAMS						
<i>Authors:</i> Tuan Le, Anna Paradowska, Mark A. Bradford, Xinpei Liu, Hamid R. Valipour						
<i>Journal or book name:</i> Journal of Constructional Steel Research						
<i>Volume/page numbers:</i>						
<i>Date accepted/ published:</i>						
Status	<i>Published</i>		<i>Accepted and In press</i>		<i>In progress (submitted)</i>	X
The Candidate's Contribution to the Work						
The candidate has conducted the experiments and numerical modelling, analysed data and prepared manuscript.						
Location of the work in the thesis and/or how the work is incorporated in the thesis:						
This publication was incorporated in Chapter 3 of the thesis.						
Primary Supervisor's Declaration						
I declare that:						
<ul style="list-style-type: none"> • the information above is accurate • this has been discussed with the PGC and it is agreed that this publication can be included in this thesis in lieu of a Chapter • All of the co-authors of the publication have reviewed the above information and have agreed to its veracity by signing a 'Co-Author Authorisation' form. 						
<i>Supervisor's name</i>	<i>Supervisor's signature</i>		<i>Date (dd/mm/yy)</i>			
Prof Mark Bradford			03/10/19			

Details of publication #2:						
<i>Full title:</i> BUCKLING OF WELDED HIGH-STRENGTH STEEL I-BEAMS						
<i>Authors:</i> Tuan Le, Mark A. Bradford, Xinpei Liu, Hamid R. Valipour						
<i>Journal or book name:</i> Journal of Constructional Steel Research						
<i>Volume/page numbers:</i>						
<i>Date accepted/ published:</i>						
Status	<i>Published</i>		<i>Accepted and In press</i>		<i>In progress (submitted)</i>	X
The Candidate's Contribution to the Work						
The candidate has conducted the experiments and numerical modelling, analysed data and prepared manuscript.						
Location of the work in the thesis and/or how the work is incorporated in the thesis:						
This publication was incorporated in Chapter 4 of the thesis.						
Primary Supervisor's Declaration						
I declare that:						
<ul style="list-style-type: none"> • the information above is accurate • this has been discussed with the PGC and it is agreed that this publication can be included in this thesis in lieu of a Chapter • All of the co-authors of the publication have reviewed the above information and have agreed to its veracity by signing a 'Co-Author Authorisation' form. 						
<i>Supervisor's name</i>	<i>Supervisor's signature</i>		<i>Date (dd/mm/yy)</i>			
Prof Mark Bradford			03/10/19			

Details of publication #3:						
<i>Full title:</i> EXPERIMENTAL AND NUMERICAL STUDIES ON LATERAL-TORSIONAL BUCKLING OF WEB-TAPERED HIGH-STRENGTH STEEL I-BEAMS						
<i>Authors:</i> Tuan Le, Mark A. Bradford, Xinpei Liu, Hamid R. Valipour						
<i>Journal or book name:</i> Journal of Constructional Steel Research						
<i>Volume/page numbers:</i>						
<i>Date accepted/ published:</i>						
Status	<i>Published</i>		<i>Accepted and In press</i>		<i>In progress (submitted)</i>	X
The Candidate's Contribution to the Work						
The candidate has conducted the experiments and numerical modelling, analysed data and prepared manuscript.						
Location of the work in the thesis and/or how the work is incorporated in the thesis:						
This publication was incorporated in Chapter 5 of the thesis.						
Primary Supervisor's Declaration						
I declare that:						
<ul style="list-style-type: none"> • the information above is accurate • this has been discussed with the PGC and it is agreed that this publication can be included in this thesis in lieu of a Chapter • All of the co-authors of the publication have reviewed the above information and have agreed to its veracity by signing a 'Co-Author Authorisation' form. 						
<i>Supervisor's name</i>	<i>Supervisor's signature</i>		<i>Date (dd/mm/yy)</i>			
Prof Mark Bradford			03/10/19			

ABSTRACT

This thesis presents experimental and numerical studies on the buckling behaviour of I-section beams fabricated from high-strength steel (HSS) plates having nominal yield stresses greater than 450 MPa. The research program contains three major tests including the assessment of residual stress distributions in welded HSS I-sections, the buckling of HSS I-beams and the lateral-torsional buckling of web-tapered HSS beams.

The measurement of residual stresses induced in welded HSS I-sections was firstly undertaken using the neutron diffraction (ND) technique, based on which a unified residual stress pattern applicable for I-section beams is suggested. The residual stress specimens consisted of two prismatic I-sections fabricated from Australian BISPLATE-80 steel plates with a nominal yield stress of 690 MPa and BISPLATE-100 steel plates with a nominal yield stress of 890 MPa, and one web-tapered I-beam made of BISPLATE-100 plates. A high spatial resolution of residual stresses in the cross-sections is obtained, and especially the high stress gradient in the weld bead, as a consequence of the deep penetration of the neutron particles into the material. It is revealed that the tensile stresses peak at the flange-web junctions at an average of 70% of the parent material yield stresses, and that the compressive stresses have an approximately uniform distribution that dominates large regions of the flange and web. In addition, the compressive residual stresses appear to be related to the geometry of the cross-section and independent of the steel grade. The interaction of the residual stresses in the flange and web was found to be negligible for both prismatic and web-tapered

beams. A residual stress model is proposed by fitting the test results and collective data available in the literature.

The second part of this study presents experiments and a numerical investigation of the buckling response of the HSS I-beams. For the experimental program, three BISPLATE-80 and five BISPLATE-100 prismatic I-beams were fabricated and tested under scenarios of uniform bending and moment gradient. The specimens developed either lateral-torsional buckling or flange local buckling, with tensile fracture not being observed during the tests. The buckling capacity so obtained significantly exceeded the predictions of Eurocode 3 and of the Australian AS4100, especially for intermediate beam slendernesses, while the ANSI/AISC 360-16 guidelines marginally estimated the buckling resistance of specimens. It was also found that lateral-torsional buckling initiated after partial yielding of the compression flange. The numerical studies consisted of two ABAQUS finite element (FE) models, being a test simulation model as well as a generic representation, to facilitate extending the pool of experimental data, which showed that Eurocode 3 and AS4100 underestimate the buckling strength of intermediate and slender beams, while the ANSI/AISC 360-16 curves overestimate the FE predictions for lateral-torsional buckling capacities of beams in inelastic portions. A parameter that is dependent on the material properties is introduced in the AS4100 beam buckling strength formula and a new curve for the buckling of HSS flexural members is proposed.

In the third part, a preliminary experimental study on lateral-torsional buckling web-tapered I-section beams was conducted. Four tapered beams were welded built-up from BISPLATE-100 plates and tested in uniform bending moment and moment gradient loading conditions. All tapered beams failed in lateral-torsional buckling without

tensile rupture occurring. The strength of the beams was found to be governed by the interaction of buckling and yielding (inelastic buckling) at the section whose twist displacement was greatest. The buckling moment resistance of the specimens noticeably exceeded the predictions of the Eurocode 3 and Australian AS4100, especially in the case of uniform bending when the smallest tapered cross-section is taken for calculating the nominal section capacity. An ABAQUS finite element model for web-tapered HSS beams was developed based on the test results, and subsequent parametric studies were undertaken to elucidate the effects of the tapering topology, residual stresses and flange compactness on the buckling strength of web-tapered beams.

Supporting papers

- Le T., Paradowska A., Bradford M. A., Liu X. and Valipour H. R. (2019). “Residual stresses in welded high-strength steel I-beams”. (Submitted for publication).
- Le T., Bradford M. A., Liu X. and Valipour H. R. (2019). “Buckling of high-strength steel I-beams”. (Submitted for publication)
- Le T., Bradford M. A., Liu X. and Valipour H. R. (2019). “Experimental and numerical studies on lateral-torsional buckling of web-tapered high-strength steel beams”. (Submitted for publication).

Proceeding and symposium

- Le T. and Bradford M. A. (2018). “Experimental and numerical study of flexural-torsional buckling of web-tapered high-strength steel I-beams”, 16th East Asia-Pacific Conference on Structural Engineering & Construction (EASEC16), Brisbane, Australia, December 3-6. 2019.
- Le T., Paradowska A., Bradford M. A. (2018). “Neutron diffraction for welding residual stresses in high-strength steel beams”, The 2018 ANBUG-AINSE Neutron Scattering Symposium, ANSTO, Sydney, 19-21 November 2018.
- Le T. (2018). “Buckling of high-strength steel beams”, UNSW Engineering Postgraduate Research Symposium. ISBN: 978-0-9953910-2-4, UNSW, Sydney, Australia, Sep 2018.

ACKNOWLEDGMENTS

The study presented in this thesis was undertaken in the Centre for Infrastructure Engineering and Safety (CIES) in the School of Civil and Environmental Engineering at the University of New South Wales, Sydney, Australia.

I would like to express my sincerest thanks to my supervisor Professor Mark Andrew Bradford for his inspiration, profound guidance and generous support throughout the course. I am grateful to my co-supervisor Associate Professor Hamid Reza Vali Pour Goudarzi for his encouragement and insightful suggestions, Dr. Xinpei Liu with whom I had valuable discussions, and Dr. Anna Paradowska for her great support. Their support and belief in my abilities in accomplishing the project are very much appreciated.

I would also like to thank the technical staff at the Heavy Structure Laboratory, including Dr. Zhen-Tian Chang, Mr. Ron Moncay, Mr. Greg Worthing and Mr. Sanjeewa Herath for their help on my experimental program, and I am also grateful to the academic and administrative staff of the School of Civil and Environmental Engineering for their great assistance during my PhD.

The Australian Research Council is gratefully acknowledged for funding this research project through grant DP150100446 “Buckling capacity of high-strength steel flexural members” awarded to Professor Mark Andrew Bradford. Funding from the Australian Nuclear Science and Technology Organisation through Proposals 6397 and 7531 is also acknowledged.

*My deepest gratitude to my family
for their love, support and encouragement.*

TABLE OF CONTENTS

ABSTRACT	IX
ACKNOWLEDGMENTS	XIII
TABLE OF CONTENTS	XV
LIST OF TABLES	XIX
LIST OF FIGURES	XX
NOTATION	XXV
CHAPTER 1 INTRODUCTION	
1.1. Statement of the problem	1
1.2. Aim and scope of the thesis	3
1.3. Layout of the thesis	4
CHAPTER 2 LITERATURE REVIEW	
2.1. Introduction	6
2.2. High-strength steel materials	7
2.3. Residual stresses in high-strength steel I-sections	9
2.4. High-strength steel flexural members	14
2.5. Members with non-uniform cross-section	18
2.6. Conclusions	22

**CHAPTER 3 RESIDUAL STRESSES IN WELDED HIGH-STRENGTH
STEEL I-BEAMS**

3.1.	Introduction	28
3.2.	Neutron diffraction method	29
3.3.	Experimental program	31
3.3.1.	Specimen preparation	31
3.3.2.	Material properties of BISPLATE structural plates	32
3.3.3.	Neutron diffraction procedure	33
3.4.	Test results and discussion	35
3.4.1.	Residual stresses in uniform beams	35
3.4.2.	Residual stresses in web-tapered beams	37
3.4.3.	Residual stresses in weld bead	38
3.4.4.	Error of measurements	38
3.4.5.	Equilibrium consideration	39
3.5.	Residual stress model	39
3.5.1.	Proposed formulation	39
3.5.2.	Verification	42
3.6.	Conclusions	43

**CHAPTER 4 BUCKLING OF WELDED HIGH-STRENGTH STEEL I-
BEAMS**

4.1.	Introduction	71
4.2.	Experimental proram	72
4.2.1.	Specimen preparation	72
4.2.2.	Material properties	73
4.2.3.	Residual stresses	73

4.2.4.	Geometric imperfection	74
4.2.5.	Buckling test set-up	75
4.2.6.	Instrumentation	76
4.3.	Test results and discussion	76
4.4.	Numerical study	79
4.4.1.	Finite element model	79
4.4.2.	Validation of FEM	82
4.5.	Comparison of test results and FE model with design standards	83
4.5.1.	ANSI/AISC 360-16	83
4.5.2.	Eurocode 3	85
4.5.3.	AS4100	86
4.6.	Revision to AS4100 for high-strength steels	87
4.7.	Conclusions	88

CHAPTER 5 BUCKLING OF WELDED WEB-TAPERED HIGH-STRENGTH STEEL I-BEAMS

5.1.	Introduction	125
5.2.	Experimental program	126
5.2.1.	Specimen preparation	126
5.2.2.	Material properties	127
5.2.3.	Residual stresses	127
5.2.4.	Geometric imperfection	128
5.2.5.	Buckling test set-up	128
5.2.6.	Instrumentation	130
5.3.	Test results and discussion	130
5.4.	Numerical study	132

5.4.1. Finite element model	132
5.4.2. Validation of FEM	133
5.4.3. Parametric study	134
5.4.3.1. Effects of web-taper constant	134
5.4.3.2. Effects of residual stresses	135
5.4.3.3. Effects of flange-width	135
5.5. Comparison of test results and FE model with design standards	136
5.5.1. Eurocode 3	136
5.5.2. AS4100	138
5.6. Conclusions	140
 CHAPTER 6 SUMMARY, CONCLUSIONS AND RECOMMENDATIONS	
6.1. Summary and conclusions	163
6.2. Recommendations for future research	167
 REFERENCES	 169

LIST OF TABLES

Table 2.1: Standardised high-strength steels (Ban <i>et al.</i> , 2011).....	24
Table 3.1: Geometric dimensions of residual stress specimens.....	45
Table 3.2: Material properties of BISPLATE-80 and BISPLATE-100 structural plates.....	45
Table 3.3: Specifications of gas metal arc welding (GMAW).....	46
Table 3.4: Average peak tensile residual stresses $\bar{\sigma}_{rsz}$ in the longitudinal direction.....	46
Table 3.5: Longitudinal tensile residual stresses in the weld beads of specimen RS-I-890.....	47
Table 3.6: Compressive residual stress parameters.....	47
Table 3.7: Experiment data for compressive residual stresses in welded high-strength steel I-sections.....	48
Table 3.8: Flexural strength of high-strength steel I-beams.....	50
Table 3.9: Material properties of high-strength steel plates.....	52
Table 4.1: Specimen cross-section dimensions.....	91
Table 4.2: Average tensile and compressive residual stresses.....	91
Table 4.3: Buckling strength of high-strength steel beams with uniform cross-section.....	92
Table 4.4: Validation of the finite element models.....	93
Table 4.5: Cross-sections for parametric study.....	93
Table 5.1: Specimen cross-section dimensions.....	142
Table 5.2: Average tensile and compressive residual stresses in the tapered sample RS- TB-890.....	142
Table 5.3: Bucking resistance of tapered beam specimens.....	143

LIST OF FIGURES

Figure 2.1: Historical development of steels (Willms, 2009)	25
Figure 2.2: Stress-strain curves of different high-strength steel grades	25
Figure 2.3: Residual stress models of normal-strength steel I-sections.	26
Figure 2.4: Residual stress models of high-strength steel I-sections.	27
Figure 3.1: Schematic of Bragg’s law in the neutron diffraction.....	53
Figure 3.2: The neutron diffraction technique.	53
Figure 3.3: Determination of the residual strain from the diffraction angle.	54
Figure 3.4: Geometry of the uniform I-section specimens and the principle coordinate system (xyz).....	54
Figure 3.5: Geometry of the web-tapered specimen RS-TB-890 and locations of cross- sections for residual stress measurement.	55
Figure 3.6: Fabrication procedure of residual stress specimens.	55
Figure 3.7: Prismatic and tapered residual stress specimens.	56
Figure 3.8: BISPLATE-100 stress-free reference sample.....	56
Figure 3.9: Tensile coupon dimensions.	57
Figure 3.10: Stress-strain relations of BISPLATE structural plates.	57
Figure 3.11: Tensile coupon test.	58
Figure 3.12: Tensile coupons of 12 mm BISPLATE-100 plates.	58
Figure 3.13: Test set-up (a) SScanSS for virtual sample and test simulation, and (b) a sample positioned in the Kowari neutron diffraction strain scanner.....	59

Figure 3.14: Orientation program for scanning residual strains in the flange, (a) longitudinal, (b) through-thickness, and (c) transverse direction.	60
Figure 3.15: Orientation program for scanning residual strains in the web, (a) longitudinal, (b) transverse, and (c) through-thickness direction.	60
Figure 3.16: Lattice spacing in the flanges of BISPLATE-100 stress-free sample and of specimen RS-I-890.....	61
Figure 3.17: Residual stresses in specimen RS-I-890.....	62
Figure 3.18: Residual stresses in specimen RS-I-690.....	63
Figure 3.19: Residual stresses in specimen RS-TB-890.....	64
Figure 3.20: Measurement positions in the weld beads of specimen RS-I-890, (a) top flange-web intersection, and (b) bottom flange-web intersection.....	65
Figure 3.21: Residual stress self-balancing deviation in specimen RS-I-690.....	66
Figure 3.22: Residual stress self-balancing deviation in specimen RS-I-890.....	66
Figure 3.23: Proposed residual stress model.....	67
Figure 3.24: Compressive residual stresses in the flange.	68
Figure 3.25: Compressive residual stresses in the web.....	68
Figure 3.26: Material model.....	69
Figure 3.27: Deformed configurations of the specimens at failure in the numerical simulation: (a) specimen HSA800-II-6, (b) specimen Q460GJ-C5, and (c) specimen NIONICRAL70-E.....	69
Figure 3.28: Finite element results versus test data.	70
Figure 4.1: Cross-sectional dimensions of I-beams.	94
Figure 4.2: Fabrication procedure of HSS beams.	94
Figure 4.3: High-strength steel beam specimens.	95
Figure 4.4: Locations of residual stress specimens RS-I-690 and RS-I-890.	95

Figure 4.5: Midspan sections of residual stress specimens RS-I-690 and RS-I-890.	95
Figure 4.6: Longitudinal residual stresses in RS-I-690 vs RS-I-890.	96
Figure 4.7: The set-up for out-of-plumbness assessment.....	97
Figure 4.8: The out-of-plumbness measurement positions (Xiong <i>et al.</i> , 2016).	97
Figure 4.9: Test arrangement for buckling of the beams under gradient bending moment.	98
Figure 4.10: Test arrangement for buckling of the beams under uniform bending moment.....	99
Figure 4.11: Loading box: (1) outer box, (2) inner box, (3-5) roller bearings, (6) spherical roller bearings, (7) modified spherical thrust roller bearing, and (8) I- beam specimen.	100
Figure 4.12: The assembly of the loading box.....	101
Figure 4.13: End restraint: (1) roller bearings, (2) flat plates attached to stiffeners, (3) semi-circle bar, (4) rollers, and (5) I-beam specimen.	102
Figure 4.14: LVDT layouts.	103
Figure 4.15: Strain gauge layout.	103
Figure 4.16: Draw-wire transducer arrangement.	104
Figure 4.17: Load-displacement evolutions of I-beam specimens.....	105
Figure 4.18: Longitudinal strain development in compression flanges.	109
Figure 4.19: Buckling modes: (a) LTB of an I-beam under UM, (b) LTB of an I-beam under MG, and (c) FLB of an I-beam under UM.....	113
Figure 4.20: Finite element models of HSS beams.....	114
Figure 4.21: Effective length of the tested span.....	115
Figure 4.22: Stress-strain multi-linear relation model.	115
Figure 4.23: Normalised load-displacement relations.	116

Figure 4.24: Deformation of the I-beam specimens at critical buckling load.....	119
Figure 4.25: Comparison between test results and ANSI/AISC360-16 model.....	120
Figure 4.26: Comparison between the generic FE predictions and ANSI/AISC360-16 model.....	120
Figure 4.27: Comparison between test results and EC3 limited method.	121
Figure 4.28: Comparison between the generic FE predictions and EC3 limited method.	121
Figure 4.29: Comparison between test results and AS4100.	122
Figure 4.30: Comparison between the generic FE predictions and AS4100.	122
Figure 4.31: New LTB curve for the AS4100 in the case of uniform bending moment.	123
Figure 4.32: New LTB curve for the AS4100 in the case of moment gradient.	123
Figure 5.1: Geometry of web-tapered beams.....	144
Figure 5.2: Specimen TB-890-2.....	144
Figure 5.3: Residual stresses in the web-tapered beam RS-TB-890.....	145
Figure 5.4: LTB test set-up for web-tapered beams.....	146
Figure 5.5: Loading box in the test of web-tapered beams.....	147
Figure 5.6: End restraint in the test of web-tapered beams.....	148
Figure 5.7: LVDT layout for web-tapered beams.....	149
Figure 5.8: Strain gauge layout at a cross-section.....	149
Figure 5.9: Load-displacement relations of web-tapered beams.	150
Figure 5.10: Longitudinal strain development in compression flange of the specimen TB-890-1.....	152
Figure 5.11: Deformed shape of the specimen TB-890-2.....	153
Figure 5.12: Finite element model of web-tapered beams.....	153

Figure 5.13: Normalised load-displacement relations of web-tapered beams.	154
Figure 5.14: Effects of web-taper constant α_w on buckling resistance of web-tapered beams.....	156
Figure 5.15: Effects of residual stresses on buckling resistance of web-tapered beams.	157
Figure 5.16: Effects of flange-width on buckling resistance of web-tapered beams. ...	158
Figure 5.17: Comparison between test results and EC3 limited method.	159
Figure 5.18: Comparison between FE predictions and EC3 limited method in the case of moment gradient loading ($\beta = -1/3$).	160
Figure 5.19: Comparison between FE predictions and EC3 limited method in the case of uniform bending moment ($\beta = -1$).	160
Figure 5.20: Comparison between test results and AS4100.	161
Figure 5.21: Comparison between FE predictions and AS4100 in the case of moment gradient loading ($\beta = -1/3$).	162
Figure 5.22: Comparison between FE predictions and AS4100 in the case of uniform bending moment ($\beta = -1$)	162

NOTATION

A_f	The area of the flange
A_w	The area of the web
a_0, a_1, a_2, a_3	Parameters of compressive residual stresses in the flange
B	The width of the beam
b_0, b_1, b_2, b_3	Parameters of compressive residual stresses in the web
b_f	Clear width of the flange outstand from the face of the web
C_b	Moment modification factor
$D_{ai}, D_{bi}, D_{ci}, D_{di}$	The distance from the central line connecting the flange centres at the beam ends to the flange tip at a measurement location
D_i	The average out-of-plumbness at a position
$D_{i,max}$	The maximum magnitude of out-of-plumbness of the beam
$d_0, d_{0,hkl}$	Stress free/reference lattice spacing
d_{0x}, d_{0y}, d_{0z}	Reference lattice spacing in x, y, z directions
d_0^f	Reference lattice spacing used for the flange
d_0^w	Reference lattice spacing used for the web
$d_{a1}, d_{a2}, d_{a3}, d_{a4}, d_{a5}$	The distance from a baseline to a flange tip
d_{hkl}	The distance between atomic planes (hkl) in a crystalline material
d_x, d_y, d_z	Lattice spacings in x, y, z directions of a stressed sample
E, E_{hkl}	Elastic modulus
f_u	Nominal tensile strength
f_y	Nominal yield strength

G	Shear modulus
H	The depth of a cross-section
H_1	The depth of the largest cross-section
H_2	The depth of the smallest cross-section
H_{cr}	The depth of the critical cross-section
h_{o1}	The distance between top and bottom flange centroids of the largest cross-section
h_{o2}	The distance between top and bottom flange centroids of the smallest cross-section
h_w	The height of a web
I_w	Warping constant
J	Torsion constant
K	Beam slenderness parameter
k_r	Effective length factor for restraint against lateral rotation
L	Total length of a specimen/sample
L_e, L_{oc}	Effective length of a tested span
L_o	Length between points of effective bracing or restraint
L_p	The unbraced length limit for the yielding limit state
L_r	The unbraced length limit for the inelastic lateral torsional buckling limit state
M	External bending moment
M_b	Buckling moment
M_m	Maximum moment carrying capacity
M_{nFLB}	Nominal moment capacity for flange local buckling limit state

M_{nLTB}	Nominal moment capacity for lateral torsional buckling limit state
M_{nP}	Nominal moment capacity for yielding limit state
M_{oa}	Reference elastic buckling moment excluding the effect of non-uniform moment distribution
M_{ob}	Elastic buckling moment
M_p	Nominal plastic moment
$M_{p,cr}$	Nominal plastic moment of critical cross-section
M_{Rk}	Nominal bending moment capacity of the most critical section
M_s	Nominal bending moment capacity of the most critical section
M_y	Nominal yielding moment
$M_{y,cr}$	Nominal yielding moment of critical cross-section
P	Transverse load
R	Rotational capacity
r_y	Radius of gyration about minor principal y-axis
S_x	Plastic section modulus
t	Nominal thickness of a steel plate
t_f	Thickness of a flange
t_w	Thickness of a web
u_x, u_y, u_z	Displacements in x, y, z directions
Y/T	Yield to tensile strength ratio
Z_x	Elastic section modulus
α_L	Transverse load ratio
α_{LT}	The imperfection factor with respect to the height-to-width ratio
α_m	Moment modification factor

α_s	The slenderness reduction factor
α_w	Web-taper constant
β	Ratio of smaller to larger bending moment at the ends of a member
γ_m	Coefficient with respect to steel material properties
ε_e	Elongation
ε_u	Ultimate strain
ε_y	Yield strain
θ_{hkl}	Bragg's angle
λ	Wavelength of a radiation
λ_f	Flange slenderness
λ_s	Modified slenderness
λ_w	Web slenderness
$\bar{\lambda}_{LT}$	Non dimensional slenderness for lateral torsional buckling
$\bar{\lambda}_{op}$	Global non dimensional slenderness of a structural component for out-of-plane buckling
ν	Poisson's ratio
σ_{rf}	Residual stress in a flange
σ_{rfc}	Compressive residual stress in a flange
σ_{rft}	Tensile residual stress in a flange
$\sigma_{rsx}, \sigma_{rsy}, \sigma_{rsz}$	Residual stresses in x, y, z directions
σ_{rw}	Residual stress in a web
σ_{rwc}	Compressive residual stress in a web
σ_{rwt}	Tensile residual stress in a web
σ_u	Ultimate stress

σ_y	Yield stress
$\bar{\sigma}_{rsz}$	Average peak tensile longitudinal residual stress
Φ_{LT}	Value to determine the reduction factor χ_{LT}
ϕ_x, ϕ_y, ϕ_z	Rotations about x, y, z direction
χ_{op}	Reduction factor for the non-dimensional slenderness $\bar{\lambda}_{op}$
$\chi_{op,mod}$	Modified reduction factor for lateral-torsional buckling
χ_{LT}	Reduction factor for lateral-torsional buckling
$\chi_{LT,mod}$	Modified reduction factor for lateral-torsional buckling

CHAPTER 1 INTRODUCTION

1.1. Statement of the problem

High-strength steels (HSS), defined herein as having a nominal yield stress f_y greater than 450 MPa and with good weldability and notch toughness, have received much recent interest within the construction industry. The use of HSS in construction produces lighter structures that can be erected more rapidly with lower labour costs in comparison to mild steels. Using high-strength steels as a replacement for mild steels reduces undesirable emissions and waste during steel manufacture because less of it is needed, and the lighter structural frame needs less emissions-producing concrete in the foundations. However, national constructional steel design standards preclude many high-strength quenched and tempered steel grades, and with the growth update of such steels in structural applications, revision or new guidance is needed.

As being often available in the form of structural plates, high-strength steels are commonly welded into shapes, and such a fabrication procedure induces residual stresses which are a major influence on the ultimate strength limit states design of steel structures. Studies of residual stresses in wide flange I-sections having steel grades up to 690 MPa have been reported extensively in the literature. However, very little experimental data is available on the magnitude and distribution of residual stresses in I-sections with yield stresses exceeding 690 MPa. In addition, previous models for residual stresses proposed by Wang *et al.* (2012) and Ban *et al.* (2013a, 2013b) may only be applicable to HSS I-section columns (with wide flanges) rather than I-section

beams in which the flange tip regions develop compressive stresses after the cooling process (Yang *et al.*, 2016). Because of this, a reliable residual stress model applicable to HSS I-beams is much needed for structural analysis and modelling, as is a reliable measurement of the tensile stress distribution in the heat-affected zone (HAZ) because the results obtained from the destructive sectioning technique can vary due to the difficulty of accessing the weld region.

It has been noted that the residual stresses induced in HSS sections is significantly less than that of mild steel sections when normalised with respect to their yield strength (Rasmussen and Hancock, 1995; Lee *et al.*, 2012), resulting in the less pronounced effects of such imperfections, which in turn may lead to a higher normalised load carrying capacity. However, very few studies of the flexural strength of HSS members with yield stresses in excess of 500 MPa can be found, and very less in the case of steel grades higher than 690 MPa. Furthermore, the major focus of available studies in the literature was the in-plane strength and ductility of HSS flexural members in which the beam developed its full plastic moment and for which failure was heralded by the onset of local buckling and/or tensile rupture. Research findings on the lateral-torsional buckling of HSS are very limited, and it appears no experimental studies have been reported on HSS beams with steel grades higher than 690 MPa. To address the design procedures for the buckling resistance of a member in bending established in Eurocode 3 (EC3) (2005) and AS4100-1998 (2016), experimental and numerical studies of the buckling of HSS I-section beams having yield stresses greater than 690 MPa are presented in this thesis.

On the other hand, non-uniform cross-section members are commonly used in steel structural applications since the distribution of stress resultants is often not constant

along their length. Such design not only fully exploits the section capacity of the member but is also economic in the sense of enabling aesthetic and light weight structures and saving resources, i.e. less materials and low erection costs. However, it is known that steel structural components are typically slender, and their strength is governed by their buckling resistance. Accordingly, the stability of non-uniform cross-section steel members and of frames incorporating such components has received considerable research interest, but very few studies on the behaviour of non-uniform cross-section members made of HSS can be found in the literature, and no experimental investigation on the stability of non-prismatic members has been reported. Research studies are therefore in need. In this thesis, preliminary experimental and numerical studies on the lateral-torsional buckling of web-tapered I-section beams fabricated from Australian BISPLATE-100 plates with the nominal yield stress $f_y = 890$ MPa are presented.

1.2. Aim and scope of the thesis

The aim of this thesis is to study the stability of high-strength steel flexural members. The research program is mainly based on experimental investigations for the residual stress pattern induced in welded HSS I-beams and for the buckling behaviour of prismatic and web-tapered beams fabricated from HSS structural plates with nominal yield stresses greater than 690 MPa. To augment the test data, 3-dimensional finite element models (FEMs) for thin-walled I-beams were constructed and calibrated against the tests and used to provide parametric studies. Accordingly, the specific objectives of the study are highlighted as follows:

- To develop a unified residual stress model applicable for welded thin-walled I-section beams having steel grades between 460 MPa and 1000 MPa, which is accurate and efficient for structural analysis and modelling;
- To provide experimental evidence for global and local buckling of prismatic and tapered HSS beams with steel grades exceeding 690 MPa;
- To develop efficient finite element models of thin-walled flexural I-section members used to facilitate extending the pool of experimental data and to carry out parametric studies;
- To evaluate the extrapolation of the national constructional design standards, which were constructed for mild steel structural members, to HSS flexural members; and finally
- To develop new design formulae for HSS beam buckling strengths where the misfit of design provisions and the test results is observed.

1.3. Layout of the thesis

This thesis is organised into six chapters. The significance and objectives of the study are introduced in Chapter 1. An overview of the current state of knowledge of HSS materials and flexural strength of HSS members is given in Chapter 2. A brief review of the literature addressing non-uniform cross-section structural members is also included in Chapter 2.

Chapter 3 presents an experimental program investigating residual stresses in welded HSS I-sections made of Australian BISPLATE-80 ($f_y = 690$ MPa) and BISPLATE-100

($f_y = 890$ MPa) structural plates using the non-destructive neutron diffraction technique. Details of this neutron diffraction method for measuring residual stresses are given. By interpolating the test results and additional data obtained from the literature, a residual stress model appropriate for welded I-section beams is recommended.

Chapter 4 reports experiments and presents numerical studies of welded HSS I-section beams fabricated by welding BISPLATE-80 and BISPLATE-100 plates. ABAQUS (2014) finite element models of the beams were then built and calibrated against the tests and used to provide parametric studies that underpin a design proposal based on a generalised buckling strength formula consistent with the AS4100.

In Chapter 5, an experimental study of lateral-torsional buckling of web-tapered beams shaped by welding BISPLATE-100 plates is presented. An ABAQUS finite element model of web-tapered high-strength steel beams was constructed based on the test results and parametric studies were carried out, based on which the effects of taper topology, residual stresses and flange compactness on the buckling strength of the web-tapered HSS beams were revealed.

Chapter 6 summarises the thesis with the main conclusions drawn and recommendations for future research are provided.

CHAPTER 2 LITERATURE REVIEW

2.1. Introduction

Contemporary high-strength steels (HSS) manufactured based on the thermo-mechanical (TM) and quenching and tempering (QT) controlling processes offer superior strength, excellent weldability, acceptable ductility and high notch toughness (Kern *et al.*, 2005; Shikanai *et al.*, 2008). With typical nominal yield stresses being from 460 MPa up to 1000 MPa, HSS can provide double to triple the yield strength of mild steel ensuring lighter structures with more useable and saleable space, lower erection costs and smaller carbon footprints. Successful applications of HSS in bridges and buildings worldwide have been reviewed in (Miki *et al.*, 2002; Ban and Shi, 2017) and hence research interests into the behaviour of HSS structures and structural components have also been stimulated.

This chapter presents a review of high-strength steel materials and research studies of the structural behaviour of high-strength steel flexural members. In particular, it begins with an overview of characteristics of high-strength fine grained steels and of steel grades specified in national constructional steel standards, followed by some successful applications of HSS in construction. Next, the studies of residual stress patterns in welded built-up HSS I-sections are reviewed. Then, investigations on the flexural strength of HSS beams from the early works by McDermott (1969) up to date are summarised. In addition, a brief review of important contributions in theoretical and experimental developments of members with non-uniform cross-section is given, based

on which experimental and numerical studies on web-tapered HSS I-beams were conducted and are presented in this thesis.

2.2. High-strength steel materials

The material properties of steel products can be improved during the manufacturing processes by the modification of the alloy constitution and/or thermo-mechanical treatment (Shikanai *et al.*, 2008). During the TM or QT metallurgical processes, the atomic structure of conventional low carbon steels (or mild steels) is converted into a finer atomic arrangement, resulting in high strength and high performance steels which have special mechanical properties (Miki *et al.*, 2002; Schröter, 2006).

QT steel plates with nominal yield stresses of 690 MPa were commercial about five decades ago, and those of over 1100 MPa are now available (Schröter, 2006). A diagram of the historical development of steel grades and corresponding production processes shown in Figure 2.1 is given by Willms (2009) and high-strength steel grades standardised in national constructional steel standards are summarised in Table 2.1 (Ban *et al.*, 2011).

Mostly being produced in the form of plates, the weldability of high-strength steels is a major concern for fabrication. It is indicated that successful welding connections of HSS component plates can be achieved by following appropriate welding parameters and sequences (Schröter, 2006; Willms, 2009). Besides, the toughness of HSS is shown to be better than mild steels based on Charpy tests although the ductility of the steels decreases as the steel grade increases (Ban *et al.*, 2011). Figure 2.2 compares the stress-strain relations of different steel grades, in which higher strength steels inherit smaller elongations at fracture and higher yield to tensile strength ratios (Y/T) with no distinct

yield plateaux. The economic aspect of using HSS in construction is discussed in (Johansson and Collin, 2005). In general, the material cost reduces with the increase of the yield strength and the saving is significant when the strength of HSS members is fully utilised. In addition, HSS materials enable aesthetic and light structures. Compared to conventional mild steels, ArcelorMittal announced a weight reduction of 32% in columns and 19% in beams in its HSS applications, and up to 30% of CO₂ emission was eliminated during construction processes.

A brief historical development of steels, focusing on high-performance steels (HPS) in the United States, was given by Bjorhovde (2004). It was reported the A514 being the first ATSM QT steel standard, although research studies demonstrated that beams and girders made of such steels did not have sufficient deformation capacity. Nowadays, the ASTM A913 and A702 steels have been extensively used for building and bridge structures respectively with the first successful application of HPS 70W (ASTM A702) being Synder Bridge in Nebraska, which has five girders of 1.37 m deep and 45.7 m span, carrying four traffic lanes (Pocock, 2006). The use of high-performance steels for bridges in Japan was reviewed by Miki *et al.* (2002), and the first building utilising steels having nominal tensile strength of 600 MPa for its structural elements was the Landmark Tower in Yokohama (Pocock, 2006).

In Europe, applications of high-strength steels vary from hybrid girder bridges to offshore platforms. The girders of bridge Z1207 in Mittådalen were fabricated with S690 steel plates for the bottom flange and S460 for the web and top flange to optimise material usage and costs (Johansson and Collin, 2005). The Sony Center in Berlin employed S460 and S690 for its roof truss to minimise the cross-section size (Johansson and Collin, 2005). The steel grade S500M was applied in the Valhall offshore platforms

in Norway, sections of which required high yield strengths and good processing properties due to welding in severe conditions (Willms, 2009).

Further examples of high-strength steels utilised in iconic civil applications were given in a review paper of Ban and Shi (2017), particularly Q460 steels in the National Stadium, CCTV Headquarters and Phoenix International Media Center in Beijing; HSA800 steels in SNU Kwangjeong Library and Lotte World Tower in Seoul; and Australian BISPLATE-80 (Grade 700) steels in the Latitude Building in Sydney.

2.3. Residual stresses in high-strength steel I-sections

Residual stresses are a major influence on the ultimate strength limit state design of steel structures and their distributions in hot-rolled and welded normal-strength I-section steel members have been widely reported in the literature (Bradford and Trahair, 1985; Shayan *et al.*, 2014; Abambres and Quach, 2016; Subramanian and White, 2017) with some of commonly used patterns summarised in Figure 2.3. Furthermore, residual stresses induced during the shaping process of wide flange I-sections with steel grades up to 690 MPa have been extensively investigated. Studies of the residual stress patterns in HSS I-members are summarised in the following paragraphs.

The measurement of residual stresses in ASTM A514 steel ($f_y = 690$ MPa or 100 ksi) welded I-sections was reported initially by Odar and Nishino (1965) and Nishino and Tall (1970) some five decades ago. Two different sections were investigated using the method of sectioning. The tensile residual stresses were reported predominantly at the flange-web junction, whilst the compressive residual stresses having a uniform distribution dominated the middle regions of the flange and web. The peak tensile stresses developed in the heat-affected zone (HAZ) at the weld location, and their

magnitude was slightly less than the yield strength of the parent plate, decreasing with a high gradient to become compressive residual stresses outside the HAZ. The magnitude of compressive residual stresses was slightly higher than those of the I-section fabricated from ASTM A7 steel ($f_y = 250$ MPa). This indicated a much smaller ratio of compressive residual stresses to the yield strength in HSS members and consequently an expectation of a less pronounced effect of these stresses on the dimensionless compression strength curve with the HSS members.

Rasmussen and Hancock (1992, 1995) measured compressive residual stresses in four different I-sections fabricated from Australian BISPLATE-80 structural steel plates ($f_y = 690$ MPa), which is a QT low-alloy high-strength steel equivalent to ASTM A514, using the sectioning method. It was observed that the compressive stresses decreased with an increase of the slenderness of the cross-section.

In a study on the flexural strength of HSS I-beams fabricated from Slovenian QT NIONICRAL 70 steel plates ($f_y = 700$ MPa), Beg and Hladnik (1996) reported the magnitude of compressive residual stress distribution in the flange of two different I-sections.

Lee *et al.* (2012) conducted an experimental study on the flexural strength and rotation capacity of HSS I-beams in which the measurement for residual stresses in an I-section fabricated from Korean HSA800 steel having the nominal tensile strength f_u of 800 MPa using the instrumented indentation method. The results were compared with normal strength steel SM490 ($f_u = 490$ MPa) and a much lower ratio of residual stresses to the yield strength was observed in the HSS section.

Wang *et al.* (2012) investigated residual stresses in three I-sections fabricated from Chinese Q460 steel ($f_y = 460$ MPa), using both the sectioning and hole drilling methods. The flange and web components were made of 21 mm and 11 mm plates respectively with the flange slenderness varying from 3.4 to 7.1 and web slenderness from 10.9 to 23.8. It was observed that the increase in flange width among the specimens resulted in a decrease of compressive residual stresses and the increase of tensile residual stresses at the flange tips. In particular, the average magnitude of compressive residual stresses induced in the flanges decreased from 40.8% to 19.5% of the yield stress corresponding to the increase of flange slenderness, and the peak tensile residual stresses were in between 73.1% to 103.9% of the yield strength. It was also concluded that the average values of residual stresses from the two methods were similar, but patterns obtained from the section method were more convenient for numerical analysis. In addition, a simplified model was proposed in Figure 2.4a in which the magnitudes of the residual stresses were obtained from the yield strength of parent plates.

Further studies on welded Q460 sections were carried out by Ban *et al.* (2013a) using the sectioning method. Eight different I-sections were fabricated from flame-cut 10, 12 and 14 mm thick plates assembled using 6 mm fillet welds with single pass except one specimen using a combined butt and fillet weld. The flange slenderness varied from 6 to 14, and web slenderness from 13 to 33.6. It was observed that the magnitude of the compressive residual stresses was approximately uniform and dependent largely on the cross-sectional dimensions rather than the yield strength of the parent material. The interaction of residual stresses induced in the flange and web was insignificant, and the stresses at the flange tips were tensile. A residual stress pattern (Figure 2.4b) was proposed in which the peak tensile was taken as 75% of the yield strength of parent material and tensile stresses at flange tips as 7.6%. By approximating the lower bound

of the experimental data, the magnitudes of the compressive residual stresses in the flange and web were formulated as a function of slenderness and thickness of the component plate. This model was then modified by Ban *et al.* (2013b) to extend the applicability of the model to steel grades with yield strengths up to 960 MPa.

Li *et al.* (2015) investigated residual stresses in Q690 ($f_y = 690$ MPa) welded I-sections with three different specimens fabricated from 16 mm steel plates using the sectioning method. An unchanged width of the tensile zone was observed when the section slenderness varied. This was explained based on a thermal envelope model proposed by Barroso *et al.* (2010) that under the same heat input intensity, the parent metal properties and the thickness identical heat envelope curves around the weld beads were achieved for different sectional dimensions of the specimens. A simplified residual stress pattern similar to the proposal of Wang *et al.* (2012) was recommended.

Yang *et al.* (2016) reported the residual stress distribution in Q460GJ HSS plates and welded I-sections, in which five doubly symmetric and three singly symmetric I-shapes were investigated using the sectioning method. The specimens were designed representing the beam sectional dimension with the depth to width ratio (H/B) varying from 1.5 to 2.5. High tensile stresses up to the yield stress were distributed at the edge of flame-cut plates initially, but compressive stresses rather than tensile stresses were observed at these regions after the fabricating process. The average peak tensile stress at the flange centre was 50% of the yield strength of the parent material, and 83% for the average peak tensile stress at the ends of web at the weld. It was also reported the considerable interaction of flange and web as the self-equilibrium condition of individual component plates was not negligible. Based on the test results, a residual

stress pattern was proposed as shown in Figure 2.4c in which the parameters were the ratios of residual stresses and the yield strength.

Investigations on residual stresses in welded medium-walled Q460GJ HSS I-sections were presented in (Zhu *et al.*, 2017). Four different sections with the flange and web thicknesses of 25 mm and 12 mm respectively were measured for residual stress distributions using the sectioning method. Tensile stresses were observed at the flange and web junction and the flange tips, and the thermal strains induced by the welding reduced through the thickness of the flange, resulting in a reduction of stresses through the flange thickness toward the outer surface. Furthermore, the self-equilibrium of individual plates was not satisfied so that the interaction of the flange and web should not be neglected. Similar conclusions were drawn in the study for the residual stress distribution in thick-walled Q460GJ HSS I-sections presented by Yang *et al.* (2018).

However, very few experimental data are available for sections with steel grades greater than 690 MPa, more research on the residual stress distribution in such structural components is needed, as is a reliable measurement of tensile stress distribution in the HAZ because the results obtained from the sectioning technique can vary due to the difficulty in accessing the weld region. A reliable residual stress model applicable to HSS I-beams is also necessary for structural analysis and modelling as previous models (Ban *et al.*, 2013b; Li *et al.*, 2015) may only be applicable to HSS I-section columns (with wide flanges) rather than the I-section beams in which flange tip regions develop compressive stresses after the cooling process (Yang *et al.*, 2016). Accordingly, an experimental investigation on the residual stress distribution in the welded BISPLATE-80 ($f_y = 690$ MPa) and BISPLATE-100 ($f_y = 890$ MPa) I-beam sections using the non-

destructive neutron diffraction method was undertaken and obtained results are given in Chapter 3 of this thesis.

2.4. High-strength steel flexural members

An overview of the literature on the laboratory testing and numerical modelling of flexural members made of HSS is provided in the following, in which concerns regarding the compliance of HSS structural members with national constructional design standards are raised.

McDermott (1969) investigated the flexural strength and rotation capacity of ASTM A514 steel beams some fifty years ago with a yield strength of $f_y = 690$ MPa (100 ksi). The results of these tests revealed that HSS beams have sufficient rotation capacity under pure bending and moment gradient loading regimes for plastic methods of design to be used. Furthermore, a flange slenderness ratio of $b/t_f \leq 5$ and an unsupported minor axis slenderness ratio $L/r_y \leq 21$ for pure bending and $L/r_y \geq 36$ for linear moment gradient was reported to be adequate for safeguarding HSS beams from plastic buckling.

Much later, Kato (1990) presented an analytical study of the relations of stress-strain curves and the yield to tensile strength ratio to the plastic deformation capacity of steel members. It was demonstrated that the deformation capacity of steel members is reduced significantly with the increase of the yield to tensile stress ratio and hence an upper limit of the yield strength and/or yield to tensile ratio imposed for each steel grade to secure a reliable deformation capacity was recommended (Kato, 1990). Also, Kato proposed an interaction formula of flange and web slendernesses to the rotation capacity of flexural members.

Beg and Hladnik (1996) studied the demarcation of non-compact and slender I-section beams fabricated from NIONICRAL-70 HSS ($f_y = 700$ MPa) based on Kato's interaction formula (Kato, 1990). In their work, ten beams with different flange slendernesses were tested, while the variation of the web slenderness was considered in their finite element modelling. The section slenderness limit defined with respect to the interaction of the flange and web slendernesses was addressed.

Galambos *et al.* (1997) reviewed the attributes of high-performance steel with yield strengths between 480 MPa and 690 MPa (70 ksi and 100 ksi) based on relevant studies of the topic up to that time and concluded the feasibility of such new steel material applicable for the civil engineering structures, but noted the necessity of further experiments and numerical simulations for structural behaviour of HSS members.

Green *et al.* (2002) presented the inelastic flexural strength of I-beams fabricated from HSLA-80 high-performance steel with a yield strength $f_y = 550$ MPa (80 ksi). Ten beams were tested under monotonic moment gradient, uniform moment and cyclic moment gradient, with the objective to assess the effects of the material and geometric properties on the in-plane behaviour and of structural HSLA-80 members subjected to seismic action in comparison to three A36 normal strength steel members ($f_y = 248$ MPa or 36 ksi). Only HSLA-80 members with ultra-compact webs achieved the minimum rotation ductility of $R = 3$ required in ANSI/AISC 360-16 (2016), and none satisfied the ductility limit of $R = 7$ required for seismic design (AASHTO, 2016).

Ricles *et al.* (1998) evaluated the application of the United States compactness criteria to HSS beams and beam-columns by reviewing a number of analytical and experimental studies of HSS flexural members. The effect of web and flange slenderness criteria, mechanical properties of the steel and the axial force were considered by Ricles, and it

was shown that the rotation capacity of HSS members decrease with an increase of the web and compression flange slenderness. It was further found that generalising the US compactness ratio to HSS beams and beam-columns overestimates their flexural ductility and that this ductility is affected significantly by the yield to tensile strength ratio.

Earls (1999) carried out a numerical study of HSLA-80 wide flange beams under three-point loading to examine the correlation between the buckling mode shape and the ductility. Two distinct asymmetrical failure modes were identified; the first being characterised by flange local buckling in the mid-span region with slight flexural-torsional buckling, whereas the second mode involved highly coupled local-global buckling in which the flange local buckling component took place half the beam depth from the mid-span stiffener. Bracing at such positions was recommended as the beam with the second mode of buckling had significantly lower rotation capacity.

Lee *et al.* (2012) undertook flexural tests of sixteen Korean HSB800 and HSB800 HSS I-shaped beams, having $f_y = 690$ MPa, and they reported high flexural strength but marginal rotation capacity for the plastic design of HSS beams due to the absence of distinct yield plateaux and the high yield to tensile strength ratio of HSS materials. In addition, partial-height stiffeners, rather than full-height stiffeners, were recommended in order to avoid tensile rupture which is directly related to the welding heat input.

Xiong *et al.* (2016) investigated the flexural-torsional buckling of Chinese Q460GJ welded structural steel beams ($f_y = 460$ MPa), testing eight members under moment gradient. It was noted that the ANSI/AISC 360-16 design guidance may be unsafe for the global stability of Q460GJ beams, but the provisions of EC3 (2005) for rolled sections or equivalent welded cross-sections were reasonably applicable for Q460GJ

welded beams. Similar conclusions were drawn from the experimental and numerical investigations of singly symmetric Q460GJ beams (Yang *et al.*, 2017; Kang *et al.*, 2018).

Bradford and Liu (2016) presented a numerical parametric study of the flexural-torsional buckling of a wide range of HSS I-beams with compact sections under uniform bending. The effects of beam span to depth ratio (L/H), steel grade, geometric imperfection, residual stresses and size of cross-section were investigated. In particular, the initial stiffness and bending strength of the HSS beams increase with the decrease of L/H ratio while the peak displacements at critical load increase as the L/H ratio decrease. The dimensionless buckling resistance of beams with intermediate slendernesses increase substantially with the increase of steel grade. The dimensionless buckling strengths reduce as the out-of-plumbnesses increase, and the reduction become significant for beams with slenderness less than 1.75. The greatly adverse effects of residual stresses to the buckling resistance of beams with steel grade of 460 MPa were demonstrated while such effects were less pronounced for beams with higher yield strengths. This can be reasoned that the ratios of compressive residual stresses (only dependent on the cross-sectional dimensions) to the yield strength are smaller in the cases of higher strength steels, and so is in the cases of beams with wider flanges with the reduction of compressive residual stresses (Bradford and Liu, 2016). New beam curves with respect to the provisions in EC3 (2005) and AS4100-1998 (2016) were proposed.

The benefit of hybrid beams in which HSS is used for the flanges and mild steel for the web (or vice versa) has also been discussed. Suzuki *et al.* (1994) investigated local buckling of hybrid beams by examining the plastic deformation capacity versus the

slope of the collapse curves. Nine specimens having the component plates of steel grades SS400 ($f_u = 460$ MPa), SM570 ($f_u = 570$ MPa) and HT780 ($f_u = 780$ MPa) were tested under linear bending moment gradients. It was revealed the higher plastic deformation capacity of hybrid beams with HSS webs and mild steel flanges compared to those of HSS homogeneous beams. Experiments of hybrid beams with HSS flanges and mild steel webs were reported by Shokouhian and Shi (2015, 2016). Three hybrid specimens fabricated from Q460 steel plates for flanges and Q345 steel plates for webs were tested under uniform bending moment conditions. It was observed a limited rotation capacity and a reduction of dimensionless section capacity of HSS beams compared to those of homogeneous beams made of Q345 steel plates.

It can be seen that available studies focused on the in-plane strength and ductility of HSS flexural members in which the beam developed its full plastic moment and for which failure was heralded by the onset of local buckling and/or tensile rupture.

Research findings on the lateral-torsional buckling of HSS are very limited, and it appears no experimental studies have been reported on HSS beams with steel grades higher than 690 MPa. Accordingly, the buckling behaviour of HSS I-section beams is addressed in Chapter 4 of this thesis.

2.5. Members with non-uniform cross-section

Non-uniform cross-section members are commonly used in steel structural applications since the distribution of the force resultants is often not constant along their length. The use of such members not only fully exploits their section capacities, but also enables aesthetic and light weight structures, as well as savings of materials and erection costs. However, steel structural components are typically slender, and their strength is governed by their stability so that the structural behaviour of non-uniform cross-section

steel members and of frames incorporated by such components has been being received numerous research attentions. A review of studies on the topic from the early 20th century up to 2010 can be found in (Ziemian, 2010; Kaehler *et al.*, 2011; Bradford, 2006), and some of noticeable contributions to the non-prismatic flexural members are briefly given in the following paragraphs.

Theories and numerical solutions for elastic buckling of variable cross-section flexural members have been developed to some extent, beginning with the fundamental studies of Lee (1956) and Lee and Szabo (1967) on the torsional behaviour of tapered I-beams (Tankova *et al.*, 2018). Subsequently, Kitipornchai and Trahair (1971, 1972, 1975) provided important developments of differential equations for the elastic lateral-torsional buckling of stepped and tapered, symmetric and monosymmetric I-beams in which first-order bending and torsion were incorporated, and presented numerical solutions of critical buckling loads based on the finite integral method (Brown and Trahair, 1968) , which were validated with small-scale tests.

Brown (1981) derived a fourth-order differential equation in the angle of twist for elastic lateral-torsional buckling of tapered I-beams and presented some specific solutions for simply supported beams by using the finite difference method. Yang and Yau (1987) formulated a finite element from the differential equations derived for doubly symmetric tapered I-beams, in which a number of simplifications were adopted (Kaehler *et al.*, 2011).

Bradford and Cuk (1988) introduced a finite line element which provided for the nonuniformity and monosymmetry by using the web mid-height as a reference axis for twists and lateral deflections. The accuracy and rapid convergence of the method compared to those based on uniform finite elements were demonstrated. Ronagh *et al.*

(2000a) developed nonlinear equilibrium equations for variable cross-section beam-columns in which second order terms corresponding to large twists are included in the axial strains to derive the total potential, and based on which finite element formulations were derived and applications were demonstrated in (Ronagh *et al.*, 2000b). Ronagh and Bradford (1996) proposed a method for distortional buckling analysis of tapered beams by considering the coupling of local and lateral buckling.

Andrade and Camotim (2005) developed a rigorous variational formulation for elastic lateral-torsional buckling of singly symmetric web-tapered I-beams with a precise geometrical description of the member and a careful derivation of the total potential. Andrade and Camotim also provided an overview of contributions investigating the buckling behaviour of non-prismatic beams based on one-dimensional analytical formulations. Zhang and Tong (2008) proposed a new theory for lateral buckling of web-tapered I-beams by introducing a second-order term of taper effects in the strain-displacement formulation, providing appropriate solutions for beams with high taper angles (Tankova *et al.*, 2018).

Recently, Trahair and Ansourian (2016) reconsidered the distribution of internal stresses in tapered beams in which a wedge radial model was proposed for normal stress trajectories. Based on this model, Trahair (2017) developed a taper linear element for in-plane bending and out-of-plane lateral buckling analysis of tapered monosymmetric I-section members.

Furthermore, research efforts on developing design methods for buckling strength of non-prismatic I-beams have been carried out through analytical and experimental investigations (Lee *et al.*, 1971; Morrell and Lee 1974; Lee and Morrell 1975). An early experimental study was conducted by Prawel *et al.* (1974). Fifteen full-scale

beams fabricated from ASTM 242 component plates ($f_y = 290$ MPa or 42 ksi) with the weld taken only on one side of the web, which generated initial warp and bend of flanges, were investigated for bending and buckling strengths. These beams were placed in a small inclination from the horizontal, fixed at the larger end and loaded at the free end in the vertical direction. It was observed a higher buckling resistance in beams with flame-cut plates compared to beams with shear-cut plates due to the difference of residual stress patterns. In most of beams, failure occurred with the onset of local buckling in the compression flange near the fixed end. The test results were used to evaluate a moment-curvature formulation developed for bending strengths of beam-columns.

Shiomi and Kurata (1984) investigated the ultimate strength of a series of twenty four tapered beam-columns loaded by end moments in order to develop an equivalent length factor used in an interaction formula for the ultimate strength of tapered beam-columns. It was shown that the proposed formulation estimated the lower bound of experimental results.

Bradford (1988) employed the finite element model developed in (Bradford and Cuk, 1988) to obtain accurate elastic solutions of tapered I-beams used in a parametric study, based on which a design approach for the bending and buckling strength curves of tapered beams consistent with BS5950 (2000) and AS4100-1998 (2016) was proposed.

In a recent study, Marques *et al.* (2013) proposed a new design method consistent with the General Method in EC3 (2005) in which the buckling resistance is defined by the first yield stress obtained from the incorporation of first and second order forces. The design method was then reinforced by experiment studies carried out by Tankova *et al.* (2018), in which two full-scale tests on lateral-torsional buckling of web-tapered beams

were reported. One beam having stocky cross-sections along its length and the other having slender cross-sections were tested under moment gradient loadings, based on which numerical models were calibrated and used to generate test simulations.

On the other hand, the design guideline for web-tapered I-section members and frames incorporated by such tapered components with respect to the American standard ANSI/AISC360-16 (2016) is provided in (Kaehler *et al.*, 2011) with limitations specified applicable only for homogeneous members having yield stresses lower than 55 ksi (or 380 MPa).

Apparently, very few studies on the behaviour of non-uniform cross-section members fabricated from HSS can be found in the literature, and even no experimental investigation on the stability of non-prismatic members has been reported. Research efforts are therefore in need. In Chapter 5 of this thesis, preliminary experimental and numerical studies on the global buckling behaviour of web-tapered I-section beams fabricated from Australia BISPLATE-100 HSS plates with the nominal yield stress $f_y = 890$ MPa is presented and the design provisions of EC3 and AS4100 for web-tapered HSS I-beams are reviewed.

2.6. Conclusions

A brief review of studies related to high-strength steel (HSS) flexural members has been given, according to which the gaps in research studies on the structural behaviour of HSS steel beams have been indicated as follows:

- Due to the differences in stress-strain relations, higher strength steel members may not comply with design provisions which were constructed for lower strength steel

members. Unfortunately, very few experimental data are available for flexural members with the steel grade greater than 690 MPa;

- A residual stress model for HSS I-beams is needed as available proposed formulations are only applicable for HSS I-section columns (with wide flanges). Also, a reliable measurement of tensile residual stress distribution within the HAZ is necessary;
- Research findings on the buckling behaviour of HSS are very limited, and it appears no experimental studies have been reported on HSS beams with steel grades higher than 690 MPa;
- Although being common structural components in steel constructions, non-uniform cross-section members fabricated from HSS have received very little research attention; especially even no experimental investigation on the stability of non-prismatic members has been reported. Studies on such topics are therefore in need.

Table 2.1: Standardised high-strength steels (Ban *et al.*, 2011)

Country	Standard	Steel grade	Class
Europe	EN 10025-6:2004	S460, S500, S550, S620, S690, S890, S960	Q, QL, QL1
America	ASTM A514/A514M-14	A514/514M (690 MPa)	-
	ASTM A709/A709M-16	HPS 70W (485 MPa), HPS 100W (690 MPa)	Zone 1, Zone 2, Zone 3
	ASTM A913/A913M-15	70 (485 MPa)	-
Japan	JIS G 3106:2015E	SM570 (460 MPa)	-
	JIS G 3128:2009E	SHY685	N, NS
	JIS G 3140:2011E	SBHS500, SBHS700	-
China	GB/T 1591-2008	Q460, Q500, Q550, Q620, Q690	C, D, E
	GB/T 19879-2005	Q460GJ, Q500GJ, Q550GJ, Q620GJ, Q690GJ	C, D, E
Korea	KS D 5994:2011	HSA800 (650 MPa)	-
Australia	AS 3957-2008	Grade 500, 600, 700, 900, 1000	-

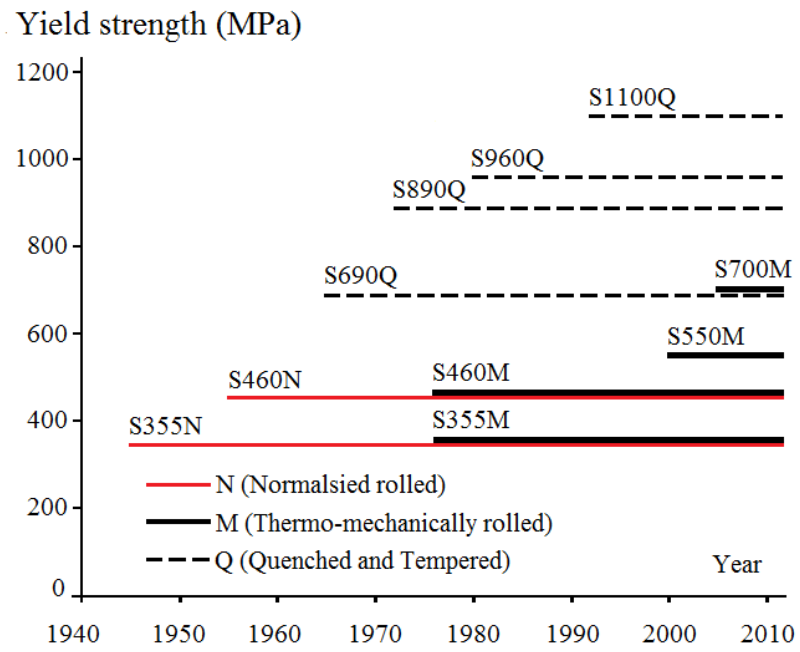


Figure 2.1: Historical development of steels (Willms, 2009)

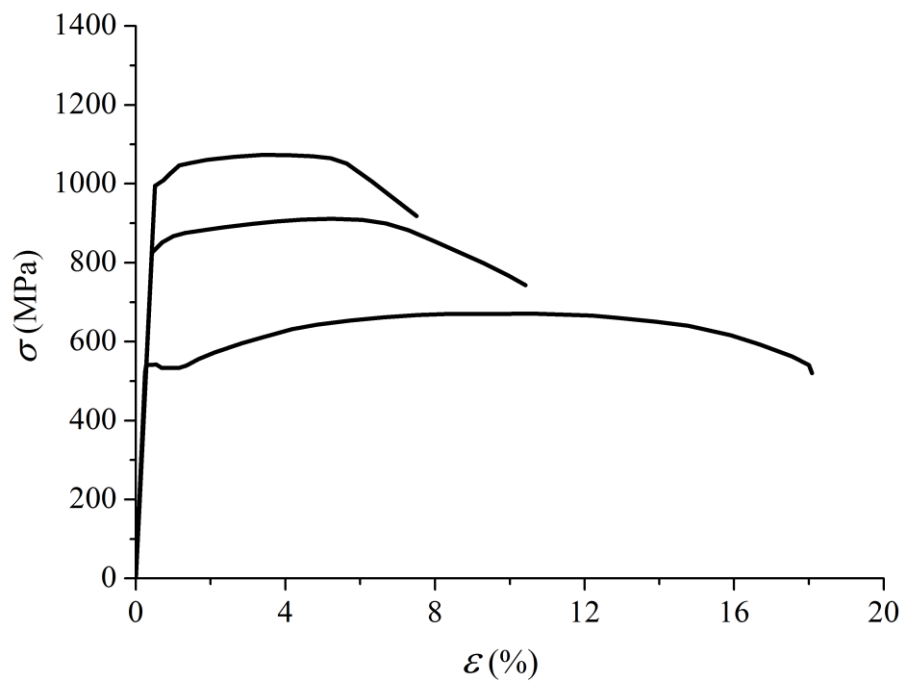
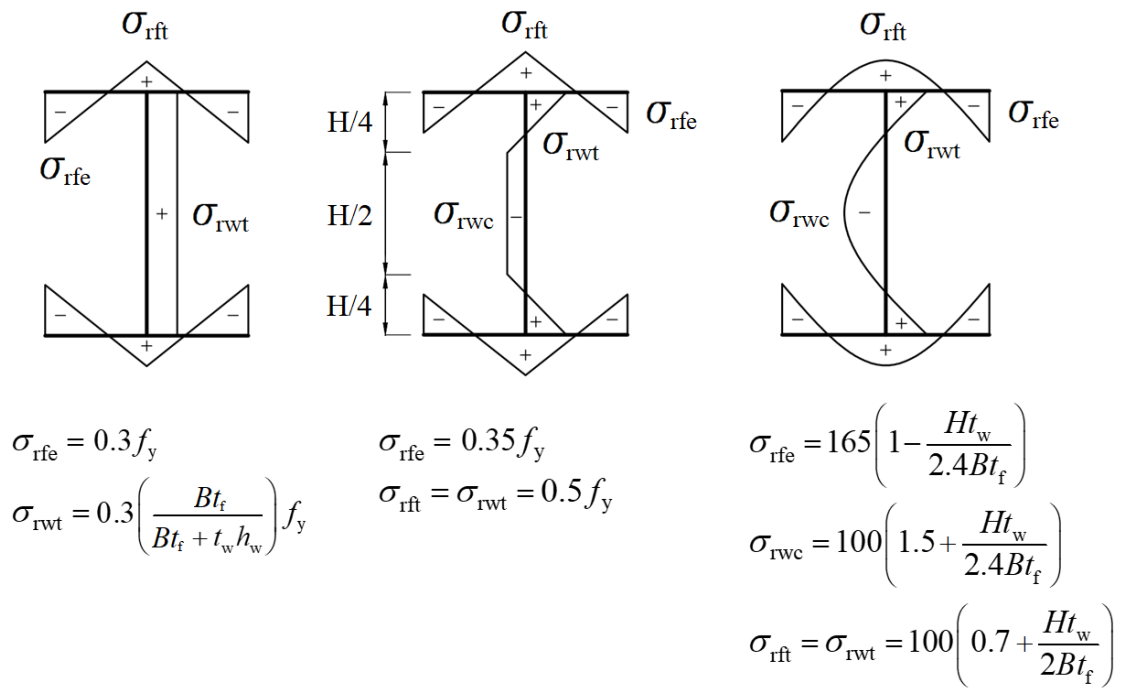
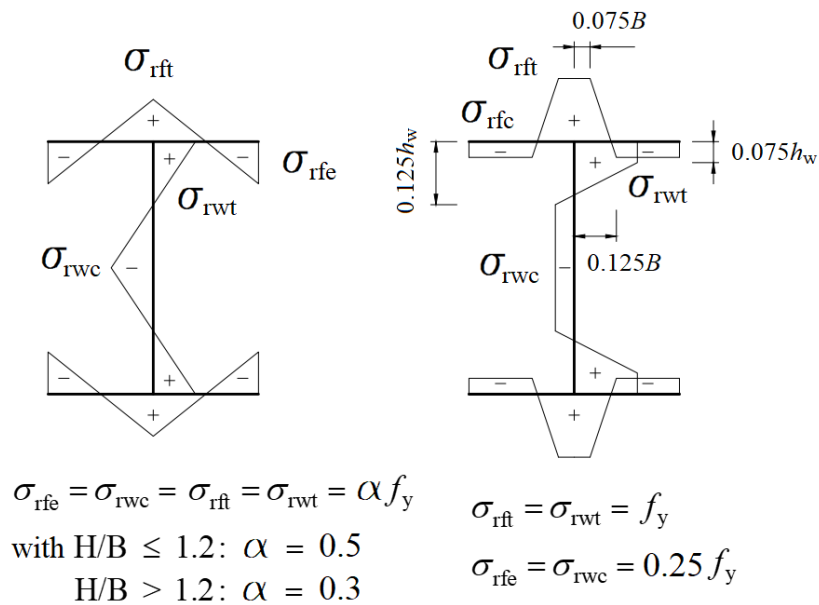


Figure 2.2: Stress-strain curves of different high-strength steel grades.

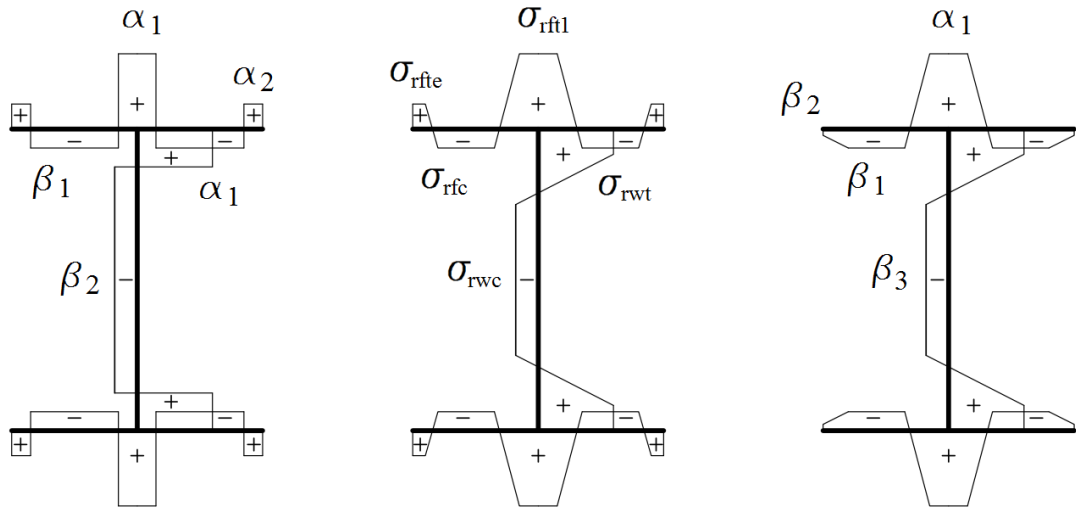


(a) (Galambos and Ketter, 1959) (b) (Bild and Trahair, 1989) (c) (Young, 1972)



(d) (ECCS, 1976) for hot-rolled sections (e) (ECCS, 1976) for welded sections

Figure 2.3: Residual stress models of normal-strength steel I-sections.



(a) (Wang *et al.*, 2012)

(b) (Ban *et al.*, 2013)

(c) (Yang *et al.*, 2016)

Figure 2.4: Residual stress models of high-strength steel I-section.

CHAPTER 3 RESIDUAL STRESSES IN WELDED HIGH-STRENGTH STEEL I-BEAMS

3.1. Introduction

Because the load carrying capacity of a steel member is largely affected by residual stresses induced during its shaping process and high-strength steel (HSS) sections are normally fabricated by welding HSS plates, it is necessary to elucidate the characteristics of residual stress patterns in welded HSS I-sections to obtain a better understanding of the buckling behaviour of HSS I-beams. Accordingly, an experimental study investigating the residual stresses in welded HSS I-section beams is presented in this chapter. The specimens included two uniform cross-section samples and a web-tapered I-beam fabricated from Australian BISPLATE-80 with nominal yield stress $f_y = 690$ MPa and BISPLATE-100 with $f_y = 890$ MPa structural steel plates that were inspected for their residual stress distribution using the non-destructive neutron diffraction method.

The neutron diffraction procedure for residual stress measurement is briefly presented in the next section, followed by the description of the experiment and a discussion of the test results. By interpolating the experimental results and collective data available in the literature, a unified residual stress model suitable for welded flexural I-section members is recommended. The proposed residual stress formulation is integrated in ABAQUS (2014) finite element models of the full-scale HSS beams and the accuracy of the

numerical model for predicting the ultimate flexural strength of HSS I-beams is demonstrated.

3.2. Neutron diffraction method

While the sectioning and other destructive methods such as slitting or hole drilling are commonly employed to assess residual stresses in steel sections, non-destructive approaches using X-ray, synchrotron X-ray, neutron diffraction (ND) are also well-developed (Withers *et al.*, 2001; Paradowska *et al.*, 2010; Alipooramirabad *et al.*, 2017). Although each technique may suit specific structural component and measurement objectives, non-destructive methods are seemingly more attractive regarding the preservation of the specimens as well as the high spatial resolution and the accuracy of the obtained residual stress pattern. Particularly, in the neutron scattering technique the chargeless particles are able to penetrate several centimetres inside the interior of the crystalline material (Allen *et al.*, 1985; Hutchings *et al.*, 2005), which provides the possibility of measuring the residual stresses in steel sections. Practical aspects of using the ND method for residual stress measurement have been reviewed by Schajer (2013) and documented in ISO/TS 21432 (2005), with a recent successful application of the method in studying the residual stress in welded HSS box-sections reported by Khan *et al.* (2016).

The principal assumption of the diffraction method is the distance between atomic planes (hkl) in a crystalline material, the so-called lattice spacing d_{hkl} , corresponding to the state of strain in the material. Accordingly, the elastic strain ε_{hkl} in a stressed sample can be obtained from

$$\varepsilon_{hkl} = \frac{d_{hkl} - d_{0,hkl}}{d_{0,hkl}}, \quad (3.1)$$

where d_{hkl} and $d_{0,hkl}$ are the lattice spacing in a stressed sample and a stress-free reference sample, respectively.

The diffraction Brag's law, which asserts that reflection of electromagnetic radiation on a crystalline lattice plane has a strong emission at a certain orientation (Schajer, 2013) as illustrated in Figure 3.1 and formulated in Eq. (3.2), is employed to determine the lattice spacing d_{hkl} .

$$\lambda = 2d_{hkl} \sin \theta_{hkl}, \quad (3.2)$$

where λ is the wavelength of the electromagnetic radiation and θ_{hkl} the Bragg angle with $2\theta_{hkl}$ being the diffraction angle.

The important characteristic of neutron radiation is its zero electronic charge which significantly reduces the interaction between neutrons and atoms of the target material, resulting in a high penetration of the neutron radiation. Because of this, measuring strains at positions of several centimetres into the thickness of a steel sample with spatial resolution of less than one millimetre is possible (Schajer, 2013). A typical set-up of strain measurement using neutron diffraction is illustrated in Figure 3.2, in which the measurement gauge volume is an intersection of incident and diffracted beams, and the gauge volume size is defined by the height and width of incident-beam slits and the collimator on the detector side. Typically, the gauge volume is fixed in space by fixing the incident beam and the detection collimator while the measuring position inside the sample is brought into the gauge volume by using a computer-controlled table capable of rotation and moving in three orthogonal directions. The scattering of neutrons

concentrates at a certain position in the detector, which can be approximated by a normal distribution with the mean representing the intensity peak as shown in Figure 3.3, and the intensity peak corresponds to the diffraction angle. It is also seen in Figure 3.3 that the shift in diffraction peaks correlates the change of diffraction angles of stress-free and stressed samples. When the lattice spacings are obtained, the residual strain ε_{hkl} can be derived and so are the residual stresses.

To calculate the principal residual stresses (σ_{xx} , σ_{yy} , σ_{zz}) in accordance with the generalised Hooke's law in Eq. (3.3) the residual strains in the three principal directions (ε_{xx} , ε_{yy} , ε_{zz}) need to be measured.

$$\begin{Bmatrix} \sigma_{xx} \\ \sigma_{yy} \\ \sigma_{zz} \end{Bmatrix} = \frac{E_{hkl}}{(1+\nu_{hkl})(1-2\nu_{hkl})} \begin{bmatrix} 1-\nu_{hkl} & \nu_{hkl} & \nu_{hkl} \\ \nu_{hkl} & 1-\nu_{hkl} & \nu_{hkl} \\ \nu_{hkl} & \nu_{hkl} & 1-\nu_{hkl} \end{bmatrix} \begin{Bmatrix} \varepsilon_{xx} \\ \varepsilon_{yy} \\ \varepsilon_{zz} \end{Bmatrix}, \quad (3.3)$$

where (x, y, z) is the principal coordinate system and E_{hkl} and ν_{hkl} the elastic constants of the crystal lattice plane.

3.3. Experimental program

3.3.1. Specimen preparation

The prismatic residual stress samples RS-I-690 and RS-I-890 were fabricated from BISPLATE-80 and BISPLATE-100 plates respectively, while the web-tapered beam RS-TB-890 was made from BISPLATE-100 plates. In detail, the prismatic samples were saw-cut from uniform cross-section beams parts of which are the specimens I-690-2 and I-890-2 used in bucking tests as shown in Figure 4.4. The geometry of the prismatic samples is depicted in Figures 3.4 with the principal coordinate system (x, y, z) , and the geometry of the tapered beam in Figure 3.5. The nominal 12 mm HSS plates

were used for the flanges and the 8 mm HSS plates for the webs, with the actual dimensions of the residual stress specimens given in Table 3.1. The strain scanning was undertaken at the mid-span of the prismatic specimens, whilst three cross-sections along the axis of the tapered beam were inspected for residual stress distributions as seen in Figure 3.5.

The component plates were flame-cut and welded together following the welding guidelines specified in AS/NZS1554.4 (2010). Gas metal arc welding with the specifications provided in Table 3.3 was applied in the fabrication of the specimens. Figure 3.6 introduces the fabricating procedure, in which the plate components were first aligned and preassembled by tack welds and steel rods. The flange-web intersection regions were then preheated to about 150 °C prior to the welding, which was performed by two accredited welding technicians on opposite sides at the same time in order to reduce the distortion caused by the unbalanced heat transfer.

The spatial restraint of the strain scanner necessitated saw cutting the tapered beam into three segments, whose mid-spans were considered for the residual stress measurements. The prismatic and tapered specimens are shown in Figure 3.7. In addition, a BISPLATE-100 stress-free sample was also prepared as seen in Figure 3.8 by cutting a 5 mm thin slice from a sample identical to the specimen RS-I-890 in the longitudinal direction to release the longitudinal stresses. The electrical-discharge machining process was employed to minimise the undesirable thermal and mechanical effects.

3.3.2. Material properties of BISPLATE structural plates

A tensile coupon test was carried out in accordance with AS1391 (2007) to determine the material characteristics of the BISPLATE-80 and BISPLATE-100 structural plates

used in fabricating the specimens. The samples were cut from the nominal 8 mm and 12 mm virgin plates by laser cutting with the gauge length of the coupon aligning with the hot-rolling direction of the parent material. Figure 3.11 shows a tensile test of a coupon using the 250 kN Instron machine, and the tensile rupture deformation of BISPLATE-100 12 mm thick coupons is shown in Figure 3.12. A low strain rate 150 $\mu\text{e/s}$ was applied up to an elongation of 1%, followed by a strain rate of 1000 $\mu\text{e/s}$ until the occurrence of tensile fracture. Typical stress-strain curves are shown in Figure 3.10 from which it can be seen that the HSS material has tensile strength ratios ($Y/T > 0.92$) and low elongation with approximately 10% in a 100 mm gauge length compared to 20% – 25% for mild steel, as well as no distinct plateaux. The mean values of the mechanical properties of the BISPLATE-80 and BISPLATE-100 structural plates are given in Table 3.2.

3.3.3. Neutron diffraction procedure

The neutron diffraction (ND) test was conducted using the Kowari Strain Scanner located at The Centre for Neutron Scattering in The Australian Nuclear Science and Technology Organisation in Sydney. The specimens were scanned for membrane residual strains distributed at the mid-plane of the flanges and webs. At regions of high stress gradient such as the flange-web junctions, weld beads and the flange tip regions, the measurement was repeated every 5 mm; however, in the compressive stress regions the measurements were repeated at 10 to 20 mm intervals.

Based on the thickness of the component plates and the proposed spatial resolution, an experimental gauge volume of $3 \times 3 \times 3 \text{ mm}^3$ was chosen to optimise the scanning time, and the measured strain was the average within the gauge volume. The incident

neutron beam having a wavelength of 1.67 Å was extracted from the Kowari monochromator. The scattering plane was α -Fe (211) with $E_{211} = 223.8$ GPa and $\nu_{211} = 0.27$, and the diffraction angle $2\theta_{211} = 90^\circ$ was positioned according to the specifications of the ISO/TS 21432 (2005).

A virtual laboratory simulation was carried out prior to the test. For this, a 3 - dimensional model of the sample was generated using a coordinate measuring machine fitted with a laser arm scanner and cooperated with “SScanSS”, the virtual Kowari instrument software for strain scanning simulation as shown in Figure 3.13. The sample was then placed on the Kowari computer-controlled table in the position at which the scattering vector was parallel to a principal strain as illustrated in Figures 3.14 and 3.15. Next, this position was mapped into SScanSS through fiducial points and the test simulation was run within the SScanSS software, based on which a script for the computer-controlled table orienting the movement of the sample in order to bring the measuring points into the gauge volume was constructed. This allows the scanning process to be ascertained as operating smoothly without collisions or off-target points.

The script was executed in the Kowari control software “GumTree” to run the actual test. The scanning time of each position was dependent on the geometry and the expected attenuation, with a longer time being applied where high attenuation was expected (mostly in the weld beads). In addition, it can be seen from Figures 3.14 and 3.15 that in order to obtain the three principal strains, the sample needed to be reoriented several times. The three principal strains in the stress-free reference sample were also measured in a similar fashion.

3.4. Test results and discussion

3.4.1. Residual stresses in uniform beams

The diffracted neutron signals scattered but concentrated at a certain point in the detector. This neutron scattering can be fitted with a normal distribution (Figure 3.3) in which the mean value defines the diffraction angle. With the diffraction angle and radiation wavelength available, Eq. (3.2) can be invoked to determine the lattice spacing d_{hkl} .

The BISPLATE-100 reference sample was scanned to obtain the reference lattice spacing (d_{0x} , d_{0y} , d_{0z}) in the three principal directions. The longitudinal stress in the reference sample was released, i.e. $\sigma_{0zz} = 0$, and the stress-free crystal spacing was determined thereby from

$$d_0 = \frac{(1-\nu)d_{0z} + \nu(d_{0x} + d_{0y})}{1+\nu}. \quad (3.4)$$

The value of d_0 obtained along the flange of the stress-free sample is plotted in Figure 3.16 and compared with the value measured along the top flange of the RS-I-890 specimen. It is seen that the distribution of d_0 is almost flat compared with that of the sample with residual stresses, and that this flat profile of d_0 implies a stress-free condition.

The mean value of d_0 was taken as the reference lattice spacing for the strain calculation, based on which the residual stresses in specimen RS-I-890 were calculated. The distribution of these stresses is plotted in Figure 3.17, which shows that the longitudinal stresses (in the z -direction) are more significant than those in the transverse and

through-thickness directions. Because of this, longitudinal residual stresses are the only stresses considered in the analysis of steel structures. It is also noteworthy that the through-thickness stresses in the flange σ_{rsy} and web σ_{rsx} approach zero outside the HAZ. This observation confirms the assumption of through-thickness residual stresses in thin-walled sections as being negligible. An alternative approach can therefore be used to obtain the stress-free lattice spacing by assigning the through-thickness stress outside the HAZ to be zero, so that the stress-free lattice spacing can be derived as

$$d_0^f = \frac{(1-\nu)d_y + \nu(d_x + d_z)}{1+\nu} \quad (3.5)$$

for the flange, and as

$$d_0^w = \frac{(1-\nu)d_x + \nu(d_y + d_z)}{1+\nu} \quad (3.6)$$

for the web, where (d_x, d_y, d_z) are the lattice spacings measured in the stressed sample.

Using the alternative method, the residual stress distribution in specimen RS-I-690 was determined and the results are plotted in Figure 3.18.

Figures 3.17 and 3.18 show the high tensile stress gradient determined at the flange-web junction. The peak tensile stresses induced in the RS-I-690 flanges were 789 MPa and 504 MPa, and those in the RS-I-890 flanges were 774 MPa and 487 MPa. On the other hand, the compressive stresses are distributed more uniformly outside of the region near the flange-web junction. The flange tip stresses are compressive rather than tensile at the flange tips because of the significant effect of restrained shrinkage during the cooling process of these I-beam sections. The average magnitudes of the compressive

stresses in the flanges of the specimens RS-I-690 and RS-I-890 were 118 MPa and 109 MPa respectively.

The tensile stresses in the web peaked at the ends of the web at the weld region, with a magnitude of 542 MPa for RS-I-690 and 713 MPa and 683 for RS-I-890. The residual stresses decrease rapidly away from the HAZ and the compressive stresses are approximately uniform over a large middle portion of the web, the average values of which are 48 MPa for RS-I-690 and 50 MPa for RS-I-890. It is noticeable that the effect of the steel grade on the compressive residual stresses is not significant, as was noted in the tests of Ban *et al.* (2013a).

3.4.2. Residual stresses in web-tapered beams

The residual stress distributions in the three cross-sections of the tapered beam RS-TB-890 are plotted in Figure 3.19. At the smallest section RS-TB-890-1, the peak tensile stress at the top flange-web junction was 845 MPa and the average magnitude of the compressive stresses in the top flange was 102 MPa. It can be seen that the difference between the stresses in the flanges of the tapered specimen RS-TB-890 and the prismatic specimen RS-I-890 is insignificant and so the effect of tapering on the residual stresses can be ignored. Because of this, the stress measurements in sections RS-TB-890-2 and RS-TB-890-3 were only made for the webs of these sections. It is also noticeable that the compressive stresses in the web increase slightly as the web slenderness decreases in the direction of the taper.

The average of the peak tensile residual stresses $\bar{\sigma}_{rsz}$ in the flanges and webs of the specimens and their ratio when normalised with respect to the nominal yield strength f_y and measured yield stress σ_y are summarised in Table 3.4. In general, the peak tensile

residual stresses for the BISPLATE-100 specimens were slightly higher than those for the BISPLATE-80 specimens. With reasonable accuracy, the average of the peak tensile stresses can be taken as 80% of the nominal yield strength f_y , or as 70% of the measured yield stress σ_y , which are similar to the maximum tensile residual stresses suggested by Ban *et al.* (2013a) for I-sections welded from 460 MPa plates, being 75% of the nominal yield strength and 68% of the actual strength.

3.4.3. Residual stresses in weld bead

In addition to the stress distribution in the web and flange of the HSS I-sections, the residual stresses induced in the weld bead of the specimen RS-I-890 were investigated. The locations at which the stresses were measured are illustrated in Figure 3.20. The magnitude of the measured tensile stresses in the weld bead, which are tabulated in Table 3.5, was averaged as 506 MPa, which is about 60% of the nominal yield strength of the parent BISPLATE-100 plates. It is noteworthy that the nominal yield and tensile strengths of the filler material AWS A5.28:ER110S-1 (2015) were 660 MPa and 760 MPa respectively.

3.4.4. Error of measurements

The accumulated error due to the experimental uncertainty was derived using the error propagation method (Taylor, 1997). Details of calculating the deviation of the residual stress vector ($\Delta\sigma_{xx}$, $\Delta\sigma_{yy}$, $\Delta\sigma_{zz}$) are provided in (Fitzpatrick and Lodini, 2003; Noyan and Cohen, 2013; Khan *et al.*, 2016). The uncertainty of the measured residual stresses was calculated to be within the range [18 MPa, 28 MPa] with an average of 21 MPa which is a typical deviation of residual stresses in steel sections obtained by using neutron diffraction method.

3.4.5. Equilibrium consideration

Since the internal stresses distributed across the cross-section of a sample are naturally self-equilibrating, the measured residual stress verification requires this equilibrium condition to be satisfied. The self-balancing deviations for the stresses in the I-690 and I-890 specimens are plotted in Figures 16 and 17 respectively, with the errors in the whole sections being less than 3% of the nominal yield strength, which represents high accuracy of the measurement technique. It is worth noting that the counterpart deviations of the residual stresses in almost all component plates is less than 5% of the yield stress, so that the interaction between the flanges and web can be considered negligible. This is not the case for hot-rolled normal-strength steel sections (Bradford and Trahair, 1985) as well as welded medium and thick-walled sections (Zhu *et al.*, 2017; Yang *et al.*, 2018), and the residual stress closing error of individual plates of some Q460 I-section samples reported in (Yang *et al.*, 2016) was considerable.

The residual stress distributions in welded steel sections are complex and largely affected by many factors such as the fabricating procedure, welding sequence and measurement methods. Therefore, more experiments and analytical investigations for the residual stress pattern in steel sections considering various cross-sectional dimensions with different steel grades are necessary, which are the interest for future studies.

3.5. Residual stress model

3.5.1. Proposed formulation

Residual stress models for hot-rolled and welded normal-strength I-section steel members have been widely reported in the literature, e.g. (Shayan *et al.*, 2014;

Abambres and Quach, 2016; Subramanian and White, 2017), but far fewer residual stress formulations for welded HSS I-sections have been proposed, with limited application to some particular cases (Wang *et al.*, 2012; Ban *et al.*, 2013; Li *et al.*, 2015; Yang *et al.*, 2016). Ban *et al.* (2013b) introduced a unified stress model for welded wide-flange I-sections with steel grades between 460 MPa and 960 MPa and so are mainly applicable to I-section column profiles for which the flange tip stresses are tensile. However, in I-section shapes with $H/B > 1$, compressive tip residual stresses have been reported (Yang *et al.*, 2016), as have the stresses measured in the current study. Accordingly, the idealised pattern of longitudinal residual stresses in Figure 3.23 can be recommended for welded HSS I-sections with the magnitude of tensile and compressive stresses obtained from

$$\sigma_{\text{rft}} = \sigma_{\text{rwt}} = 0.7\sigma_y \quad (\text{or } 0.8f_y) \quad (3.7)$$

$$\sigma_{\text{rfc}} = a_0 + a_1 t_f + a_2 t_f^2 + a_3 / \lambda_f \geq 20 \text{ MPa}, \quad (3.8)$$

and

$$\sigma_{\text{rwc}} = b_0 + b_1 t_w + b_2 t_w^2 + b_3 / \lambda_w \geq 20 \text{ MPa}, \quad (3.9)$$

in which σ_{rft} and σ_{rwt} are the peak tensile residual stresses and σ_{rfc} and σ_{rwc} the magnitude of the uniform compressive stresses in the flanges and web respectively. In Eqs. (3.8) and (3.9), the dimensions t_f and t_w are in units of mm and the stresses in MPa. The magnitude of the compressive residual stresses depends only on cross-sectional properties, being the sum of a parabolic function of the plate thicknesses and the inverse of the slenderness ratios $\lambda_f = b_f/t_f$ and $\lambda_w = h_w/t_w$. The coefficients a_1, a_2, a_3 and b_1, b_2

and b_3 in Eqs. (3.8) and (3.9) were obtained by fitting the functions to the test results herein as well as other experimental data in the literature and are given in Table 3.6.

The test data of residual stress distribution are often scattered depending on the fabricating procedure, welding sequence and measurement method. Accordingly, it is appropriate to estimate the magnitudes of the residual stresses by approximating the upper bound of the test data. Ban *et al.* (2013a, 2013b) presented a formulation for compressive residual stresses in the flange and web with respect to the slenderness and thickness of component plates of HSS I-section columns; unfortunately, the proposed model may be too conservative for HSS I-section beams with $H/B > 1$. In the present study, the coefficients a_1 , a_2 , a_3 and b_1 , b_2 and b_3 in Eqs. (3.8) and (3.9) were obtained by fitting the functions to the upper bound of the magnitudes of compressive residual stresses induced in HSS I-section beams obtained from the test herein as well as other experimental data in the literature and are given in Table 3.7.

The experimental data for compressive stresses in I-sections welded from steel plates with yield stresses between 460 MPa and 1000 MPa are summarised in Table 3.7. The plate thicknesses vary from 6 mm to 21 mm and the plate slendernesses from 3.4 to 53.8. The predicted residual stresses for the flange and web are compared with experimental data in Figure 3.24 and Figure 3.25 respectively. It can be seen that the magnitude of the compressive stress decreases rapidly with an increase of the slenderness and, for the same value of the slenderness, the compressive stresses are comparatively lower for thicker plates. In addition, the magnitude of the compressive stresses in the component plates are never less than 20 MPa. The deviations of the test data and predictions are also quantitated in Table 3.7, which demonstrates that a good approximation of the tests has been achieved, especially for specimens having $H/B > 1$.

Noting that there is negligible interaction between the residual stresses in the flanges and web, the stress patterns can be determined by substituting Eqs. (3.7) to (3.9) into the expressions

$$\iint_{A_f} \sigma_{rf} dA = 0 \quad (3.10)$$

and

$$\iint_{A_w} \sigma_{rw} dA = 0, \quad (3.11)$$

where A_f and A_w are the flange and web areas.

3.5.2. Verification

In order to demonstrate the appropriateness and feasibility of the proposed residual stress model, the predictions obtained from Eqs. (8) and (9) are compared with the estimations of Ban *et al.* (2013b) for specimens with $H/B > 1$. In particular, the mean of the ratio of the proposal to tests for the flange and web are 1.10 (with a CoV = 10.9%) and 2.05 (CoV = 60.7%) respectively, whilst the counterpart values from Ban *et al.* (2013b) are 1.77 (CoV = 19.4%) and 2.35 (CoV = 61.6%).

Further validation of the residual stress model has been performed by integrating it with a finite element model to simulate the behaviour and flexural capacity of HSS beams reported to have failed under laboratory testing by yielding or buckling using ABAQUS simulation (2014). A Python script has been written to automatically generate the FE model of HSS I-beams within the ABAQUS software, where it makes possible to assign the residual stress value for individual finite elements with respect to the element's location and size. The geometry and dimensions of the specimens are given in Table

3.8 and details of the test span and restraint conditions can be found in (Beg and Hladnik, 1996; Lee *et al.*, 2012; Xiong *et al.*, 2016). The elastic modulus was taken as $E = 200$ GPa and Poisson's ratio as $\nu = 0.25$. The multi-linear stress-strain model in Figure 3.26 along with the material properties in Table 3.9 and von Mises' yield criterion were adopted in the non-linear inelastic analysis, using the linear shell element SR4 with reduced integration. The geometric imperfections were applied based on the fundamental eigenmode obtained from an elastic buckling analysis, with the maximum value of the out-of-plumb imperfection taken as $\max(\text{span}/1000, 3 \text{ mm})$ and with the maximum value of flange local buckling imperfection of 3 mm, as recommended in the Australian steel standard AS4100-1998 (2016). The flexural strength M_b of the specimens predicted by the FE model with the residual stresses proposed are given in Table 3.8 and they show good agreement with the test data, with the average error being less than 3% with a standard deviation of 2%. The deformed configuration of the typical specimens is plotted in Figure 3.27. A comparison of the experimental and theoretical results is shown in Figure 3.28 and any discrepancy appears to be independent of the steel grade.

3.6. Conclusions

The magnitude and distribution of the residual stresses in welded HSS I-sections obtained using the technique of neutron diffraction have been presented in this chapter. Specifically, prismatic and web-tapered beams with nominal yield strengths of 690 MPa and 890 MPa were investigated. The method is shown to be capable of obtaining a high spatial resolution of residual stresses with accuracy, especially the capacity to resolve the high stress gradient in the heat-affected zone thanks to the deep penetration of the neutron particles into the material. The following conclusions can be drawn.

- The peak tensile stresses at the flange-web junction were on average 70% of the measured yield stress, or 80% of the nominal yield stress of the parent material.
- The tensile stresses in the weld bead were on average 60% of the nominal yield strength of the parent steel.
- Compressive residual stresses were located outside of the heat affected zone and were independent of the steel grade. In deference to wide flange column-type sections, the residual stresses at the flange tips were compressive.
- Interaction of the flange and web were found to be insignificant regarding their residual stresses, so each of these elements could be assumed to be self-equilibrating. The effect of tapering had negligible effect on the residual stresses.

Based on the test results and augmented with further test data in the literature, a model of the residual stresses in HSS I-section flexural members was proposed, in which the compressive residual stresses were formulated as a function of the section thickness and slenderness. The proposal correlated well with test results and was particularly accurate when the beam depth exceeded the flange width, which is representative of bending members, and when used in a FE simulation, it predicted the failure modes of HSS members reported elsewhere. This proposed formulation can be used in numerical modelling for steel of grade 460 MPa and greater.

Table 3.1: Geometric dimensions of residual stress specimens

No.	Notation	f_y	H, H_1	H_2	B	t_f	t_w	λ_f	λ_w	L
			(mm)	(mm)	(mm)	(mm)	(mm)			(m)
1	RS-I-690	690	354	-	160	11.77	7.70	6.47	42.92	1.00
2	RS-I-890	890	354	-	160	11.80	7.95	6.44	41.56	0.80
3	RS-TB-890	890	354	184	160	11.80	7.95	6.44	41.56	3.00

Table 3.2: Material properties of BISPLATE-80 and BISPLATE-100 structural plates

BISPLATE	t	f_y	σ_y	σ_u	E	ε_y	ε_u	ε_e	Y/T
	(mm)	(MPa)	(MPa)	(MPa)	(GPa)	(%)	(%)	(%)	
80	8	690	791	862	191	0.41	5.28	10.70	0.92
	12	690	851	914	195	0.44	5.08	12.90	0.93
100	8	890	1003	1070	198	0.51	3.77	9.30	0.94
	12	890	998	1078	198	0.50	3.84	9.70	0.93

Table 3.3: Specifications of gas metal arc welding

Fillet weld	Single pass 6mm
Shielding gas	18% CO ₂ in Argon
Electrode	AWS A5.28 ER110S-1 (1.2mm wire)
Voltage	27 V
Current	260 A
Travel speed	40 cm/min
Preheat temperature	150 °C

Table 3.4: Average peak tensile residual stresses $\bar{\sigma}_{rsz}$ in the longitudinal direction

Sample	Component	f_y (MPa)	σ_y (MPa)	$\bar{\sigma}_{rsz}$ (MPa)	$\bar{\sigma}_{rsz}/f_y$	$\bar{\sigma}_{rsz}/\sigma_y$
RS-I-690	Flange	690	851	647	0.94	0.76
	Web	690	791	542	0.79	0.69
RS-I-890	Flange	890	998	631	0.71	0.63
	Web	890	1003	698	0.78	0.70
RS-TB-890-1	Flange	890	998	845	0.95	0.85
	Web	890	1003	-	-	-
RS-TB-890-2	Web	890	1003	690	0.78	0.69
RS-TB-890-3	Web	890	1003	606	0.68	0.60
Average					0.803	0.702

Table 3.5: Longitudinal tensile residual stresses in the weld beads of specimen RS-I-890

Node	f_y (MPa)	σ_{rsz} (MPa)	σ_{rsz}/f_y
1	890	504	0.57
2	890	465	0.52
3	890	574	0.64
4	890	365	0.41
5	890	793	0.89
6	890	442	0.50
7	890	358	0.40
8	890	702	0.79
9	890	347	0.39
Average		506	0.57

Table 3.6: Compressive residual stress parameters

a_0	a_1	a_2	a_3	b_0	b_1	b_2	b_3
140	-16	0.4	820	115	-10	0.0	2100

Table 3.7: Experiment data for compressive residual stresses in welded high-strength steel I-sections

No.	Ref.	Grade	f_y (MPa)	Notation	Edge	H (mm)	B (mm)	t_f (mm)	t_w (mm)	H/B	λ_f	λ_w	σ_{rfc} (MPa) Test	σ_{rfc1} (MPa) Eq. (8)	$\sigma_{rfc1} / \sigma_{rfc}$ #	σ_{rfc2} (MPa) #	$\sigma_{rfc2} / \sigma_{rfc}$ #	σ_{rwc} (MPa) Test	σ_{rwc1} (MPa) Eq. (9)	$\sigma_{rwc1} / \sigma_{rwc}$ #	σ_{rwc2} (MPa) #	$\sigma_{rwc2} / \sigma_{rwc}$ #
1		Q460	460	RH3	FC	168	156	21.4	11.5	1.1	3.4	10.9	189	224	1.19	278	1.47	77	193	2.51	239	3.10
2	Wang <i>et al.</i>		460	RH5	FC	244	225	21.2	11.3	1.1	5.0	17.8	126	143	1.13	188	1.49	119	120	1.01	162	1.36
3	(2012)		460	RH7	FC	320	314	21.2	11.6	1.0	7.1	23.8	90	96	-	134	-	66	87	-	129	-
4		Q460	460	RI1	FC	110	130	10.0	10.0	0.8	6.0	9.0	277	157	-	276	-	234	248	-	290	-
5	Ban <i>et al.</i>		460	RI2	FC	150	150	10.0	10.0	1.0	7.0	13.0	207	137	-	253	-	208	177	-	215	-
6	(2013a)		460	RI3	FC	210	210	14.0	14.0	1.0	7.0	13.0	93	112	-	190	-	124	137	-	196	-
7			460	RI4	FC	150	290	10.0	10.0	0.5	14.0	13.0	164	79	-	187	-	214	177	-	215	-
8			460	RI5	FC	276	348	12.0	12.0	0.8	14.0	21.0	51	64	-	150	-	65	95	-	140	-
9			460	RI6	FC	300	220	12.0	10.0	1.4	8.8	27.6	80	99	1.24	190	2.38	75	91	1.21	126	1.68
10			460	RI7	FC	360	280	12.0	10.0	1.3	11.3	33.6	78	78	1.00	166	2.13	91	78	0.86	111	1.22
11			460	RI8	FC	150	150	10.0	10.0	1.0	7.0	13.0	191	137	-	253	-	142	177	-	215	-
12		Q460GJ	460	H1	FC	270	180	10.0	8.0	1.5	8.6	31.3	112	115	1.03	229	2.04	102	102	1.00	133	1.30
13	Yang <i>et al.</i>		460	H2	FC	360	180	10.0	8.0	2.0	8.6	42.5	113	115	1.02	229	2.03	101	84	0.83	114	1.13
14	(2016)		460	H3	FC	450	180	10.0	8.0	2.5	8.6	53.8	98	115	1.17	229	2.34	75	74	0.99	103	1.37
15			460	H7	FC	429	200	10.0	10.0	2.1	9.5	40.9	98	106	1.08	218	2.22	77	66	0.86	100	1.30
16			460	H8	FC	432	250	16.0	10.0	1.7	7.5	40.0	84	96	1.14	162	1.93	15	68	4.53	101	6.73

Chapter 3 – Residual stresses in welded high-strength steel I-beams

17	A514	690	W-A	SC	178	152	12.7	9.5	1.2	5.6	16.0	145	147	1.01	239	1.65	131	151	1.15	187	1.43
18	Odar & Nishino	690	W-B	FC	178	152	12.7	9.5	1.2	5.6	16.0	131	147	1.12	239	1.82	131	151	1.15	187	1.43
19	(1965)	690	W-C	FC	267	229	19.1	12.7	1.2	5.7	18.0	121	125	1.03	180	1.49	48	105	2.19	154	3.21
20	BISPLATE-80	690	IIRS	SC	132	96	6.0	6.0	1.4	7.5	20.0	153	168	1.10	392	2.56	100	160	1.60	200	2.00
21	Rasmussen &	690	I2RS	SC	162	116	6.0	6.0	1.4	9.2	25.0	124	148	1.19	369	2.98	76	139	1.83	178	2.34
22	Hancock (1992,	690	I3RS	SC	192	136	6.0	6.0	1.4	10.8	30.0	146	134	0.92	353	2.42	69	125	1.81	163	2.36
23	1995)	690	IRS	FC	158	140	7.7	7.7	1.1	8.6	18.4	135	136	1.01	294	2.18	32	152	4.75	185	5.78
24	NIONICRAL-70	690	B	FC	246	270	12.4	10.4	0.9	10.5	21.3	73	81	-	167	-	-	110	-	147	-
25	Beg & H. (1996)	690	D	FC	246	220	12.4	10.4	1.1	8.5	21.3	123	100	0.81	188	1.53	-	110	-	147	-
26	Q690	690	RH6	FC	206	209	16.2	16.2	1.0	5.9	10.7	105	124	-	192	-	21	149	-	226	-
27	Li <i>et al.</i> (2015)	690	RH7	FC	240	240	16.1	16.1	1.0	7.0	12.9	60	104	-	171	-	49	117	-	192	-
28		690	RH8	FC	258	262	16.3	16.3	1.0	7.5	13.9	80	94	-	159	-	9	104	-	179	-
29	Present	BIS-80	RS-I-690	FC	354	160	12.0	8.0	2.2	6.3	41.3	118	135	1.14	231	1.96	48	86	1.79	116	2.42
30		BIS-100	RS-I-890	FC	354	160	12.0	8.0	2.2	6.3	41.3	109	135	1.24	231	2.12	50	86	1.72	116	2.32
31			RS-TB-890-1	FC	326	160	12.0	8.0	2.0	6.3	37.8	102	135	1.32	231	2.26	49	91	1.86	121	2.47
32			RS-TB-890-2	FC	269	160	12.0	8.0	1.7	6.3	30.6	-	135	-	231	-	77	104	1.35	134	1.74
33			RS-TB-890-3	FC	212	160	12.0	8.0	1.3	6.3	23.5	-	135	-	231	-	59	124	2.10	156	2.64
Average														1.10	2.05		1.77	2.35			
Standard deviation														0.12	0.40		1.07	1.45			
CoV (%)														10.94	19.44		60.66	61.63			

Note: FC = Flame-cut, SC = Shear-cut, # Ban *et al.* (2013b)

Table 3.8: Flexural strength of high-strength steel I-beams

No.	Ref.	Grade	Notation	H (mm)	B (mm)	t_f (mm)	t_w (mm)	M_p (kNm)	M_m/M_p	Failure (Test)	M_b/M_p	Failure (FEM)	M_b/M_m
1	Lee <i>et al.</i> (2012)	HSB800	I-1	400	500	17.60	17.60	3915	0.99	LB	0.92	LB	0.93
2			I-2	400	220	17.60	17.60	2048	1.14	TF	1.09	LB	0.96
3			I-3	400	220	21.10	17.60	2104	1.21	TF	1.13	LB	0.94
4			I-4	400	220	17.60	17.60	2048	1.07	LTB	1.00	LB	0.94
5			I-5	400	220	17.60	17.60	2048	1.12	TF	1.00	LB	0.89
6		HSA800	II-1	400	650	17.60	17.60	4648	0.82	LB	0.84	LB	1.03
7			II-2	400	240	15.00	17.60	1889	1.06	LB	1.07	LB	1.01
8			II-3	400	240	15.00	17.60	1889	1.07	TF	1.08	LB	1.01
9			II-4	400	200	20.00	17.60	1907	1.10	LB	1.12	LB	1.02
10			II-5	400	200	20.00	17.60	1907	1.12	TF	1.14	LB	1.02
11			II-6	400	200	20.00	17.60	1907	1.10	LB	1.11	LB	1.01
12	II-7	400	160	20.00	17.60	1632	1.12	LB+LTB	1.14	LTB	1.02		
13	II-8	400	160	20.00	17.60	1632	1.14	TF	1.15	LTB	1.01		
14	II-9	400	240	15.00	17.60	1889	1.07	LB+LTB	0.98	LB	0.91		
15	II-10	400	240	15.00	17.60	1889	1.07	LB+LTB	0.98	LB	0.91		
16	II-11	400	200	20.00	17.60	1907	1.07	LB+LTB	1.05	LB	0.98		

Chapter 3 – Residual stresses in welded high-strength steel I-beams

17	Xiong <i>et al.</i> (2016)	Q460GJ	C1	270	180	10.48	9.01	330	1.02	LTB	1.05	LTB	1.03
18			C2	270	180	10.49	9.00	330	0.99	LTB	0.99	LTB	1.00
19			C3	270	180	10.43	8.82	330	0.95	LTB	0.91	LTB	0.95
20			C4	270	180	10.40	8.74	330	0.83	LTB	0.82	LTB	1.00
21			C5	450	180	10.47	8.79	654	0.97	LTB	0.94	LTB	0.97
22			C6	450	180	10.40	8.90	654	0.89	LTB	0.81	LTB	0.91
23			C7	450	180	10.47	8.84	654	0.84	LTB	0.74	LTB	0.88
24			C8	450	180	10.47	8.38	654	0.74	LTB	0.69	LTB	0.92
25	Beg, Hladnik (1996)	NION-70	A	245	300	12.50	10.40	859	0.82	LB	0.86	LB	1.05
26			B	245	270	12.50	10.40	723	0.97	LB	0.90	LB	0.93
27			C	245	250	12.50	10.40	661	0.98	LB	0.95	LB	0.97
28			D	245	220	12.50	10.40	663	0.97	LB	0.94	LB	0.96
29			E	245	200	12.50	10.40	568	0.99	LB	0.98	LB	0.99
Average												0.97	
Standard deviation												0.05	

Table 3.9: Material properties of high-strength steel plates

Grade	t (mm)	σ_y (MPa)	σ_u (MPa)	ε_y (%)	ε_u (%)
HSB800	17.6	991	1040	0.50	6.50
	21.1	879	945	0.44	6.50
HSA800	15	956	1037	0.48	6.50
	17.6	937	1037	0.47	6.50
	20	903	961	0.45	6.50
Q460GJ	8	541	669	0.27	9.67
	10	525	613	0.28	11.55
NIONICRAL70	10 (A, B, C)	775	814	0.39	6.50
	10 (D, E)	830	864	0.42	6.50
	12 (A, D)	873	883	0.44	6.50
	12 (B, E)	797	808	0.40	6.50
	12(C)	776	808	0.39	6.50

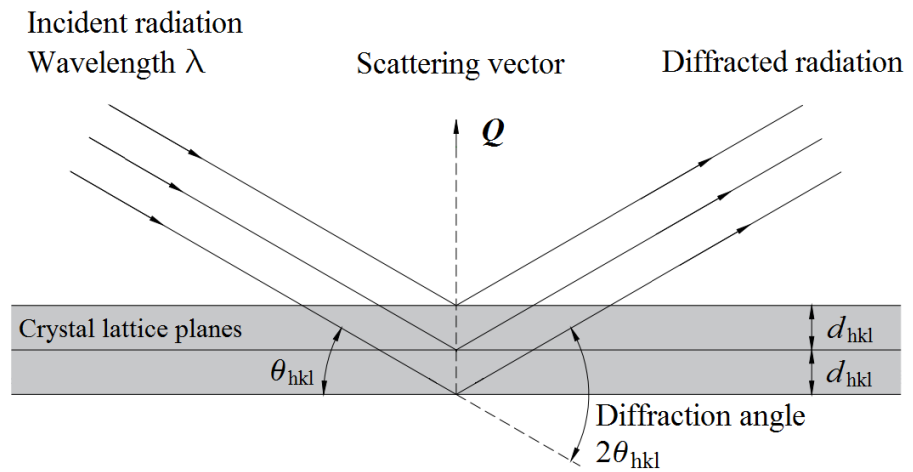


Figure 3.1: Schematic of Bragg's law in the neutron diffraction.

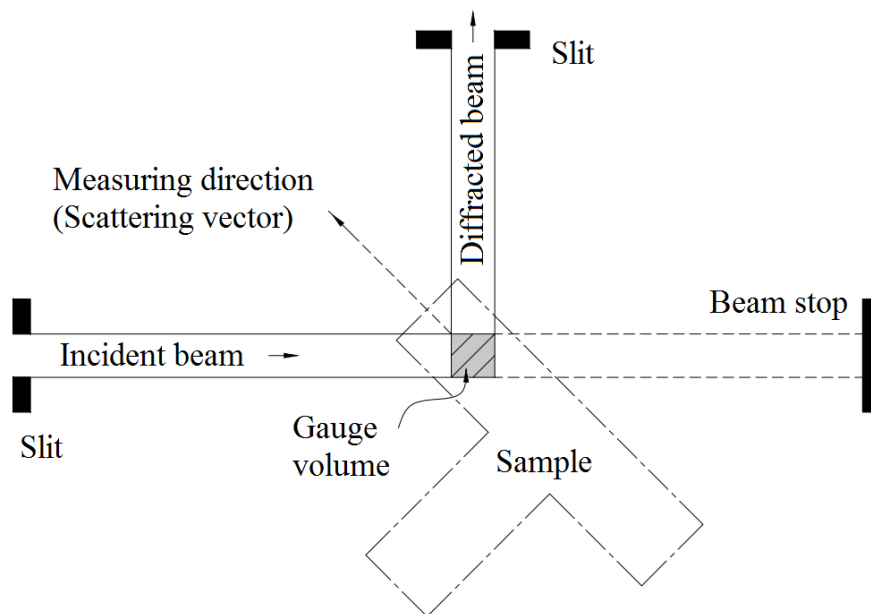


Figure 3.2: The neutron diffraction technique.

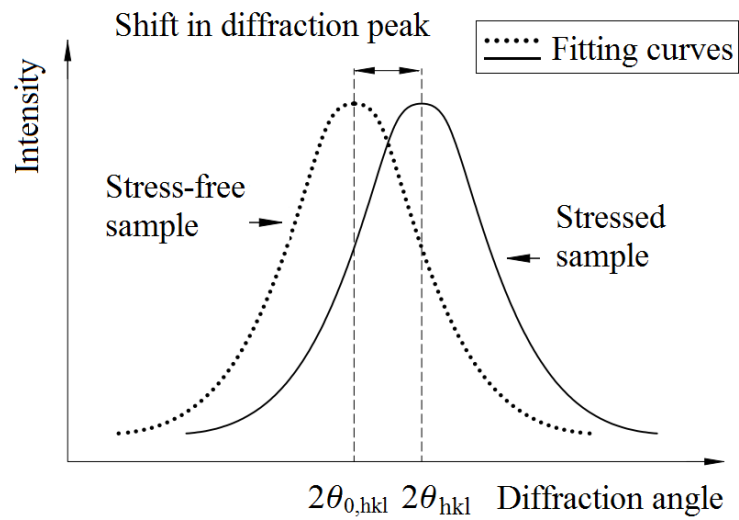


Figure 3.3: Determination of the residual strain from the diffraction angle.

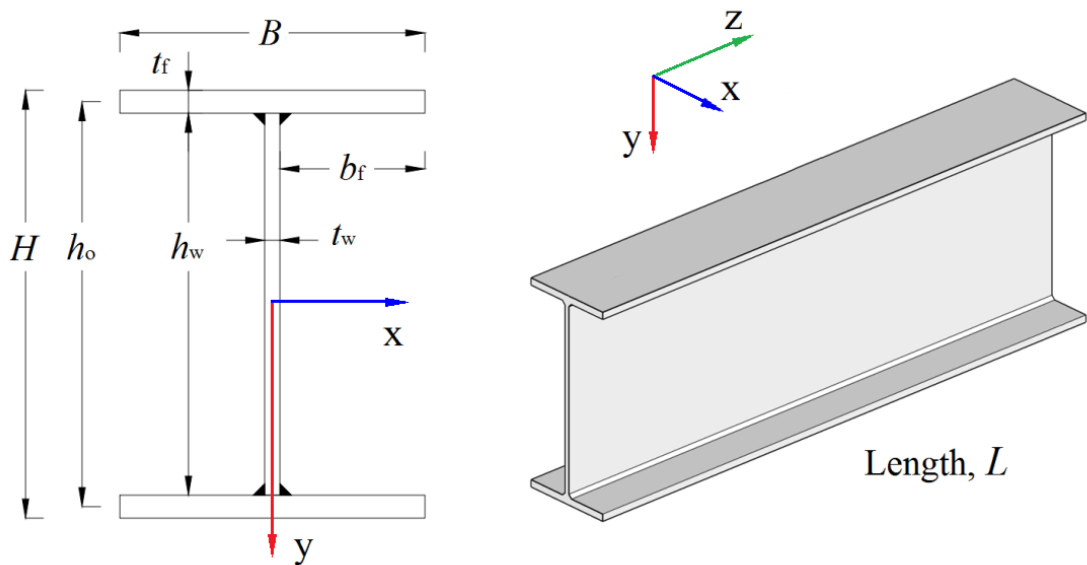


Figure 3.4: Geometry of the uniform I-section specimens and the principle coordinate system (xyz).

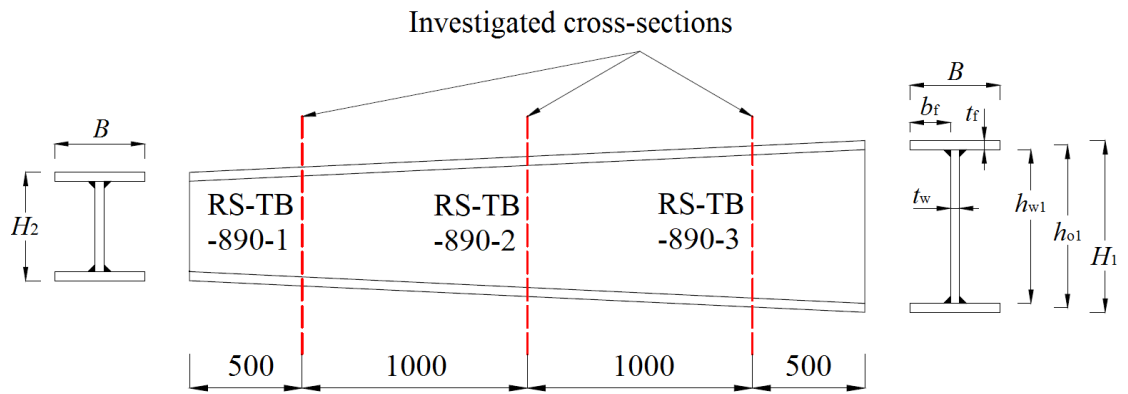


Figure 3.5: Geometry of the web-tapered specimen RS-TB-890 and locations of cross-sections for residual stress measurement.



Figure 3.6: Fabrication procedure of residual stress specimens.



Figure 3.7: Prismatic and tapered residual stress specimens.



Figure 3.8: BISPLATE-100 stress-free reference sample.

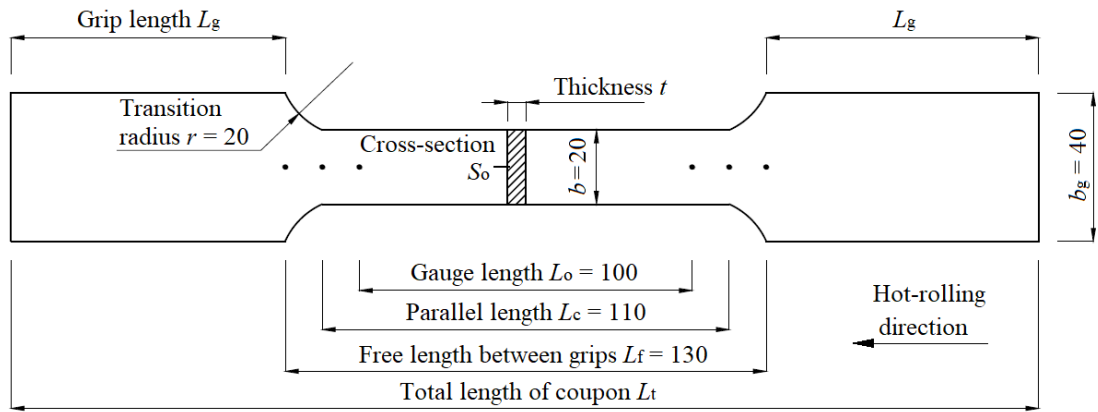


Figure 3.9: Tensile coupon dimensions.

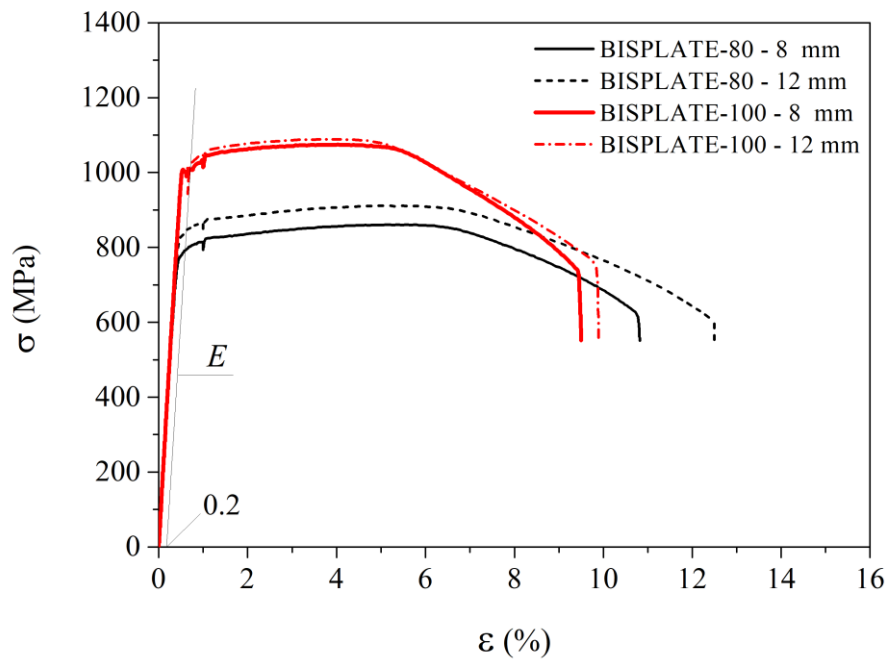


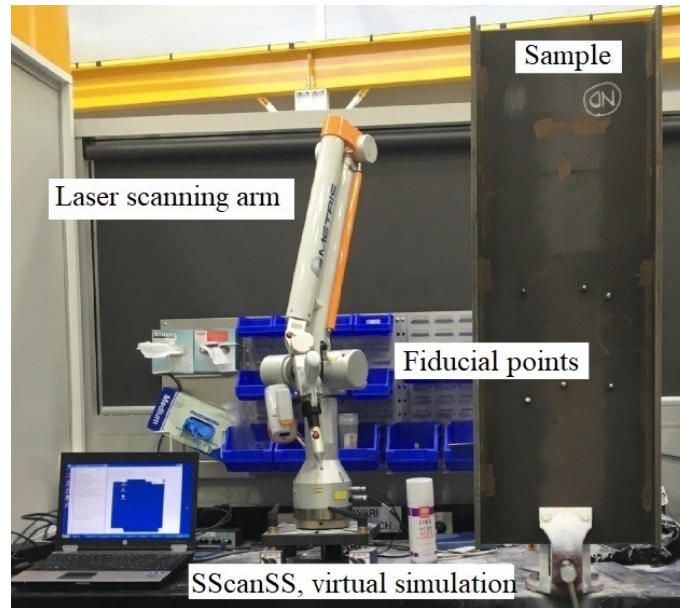
Figure 3.10: Stress-strain relations of BISPLATE structural plates.



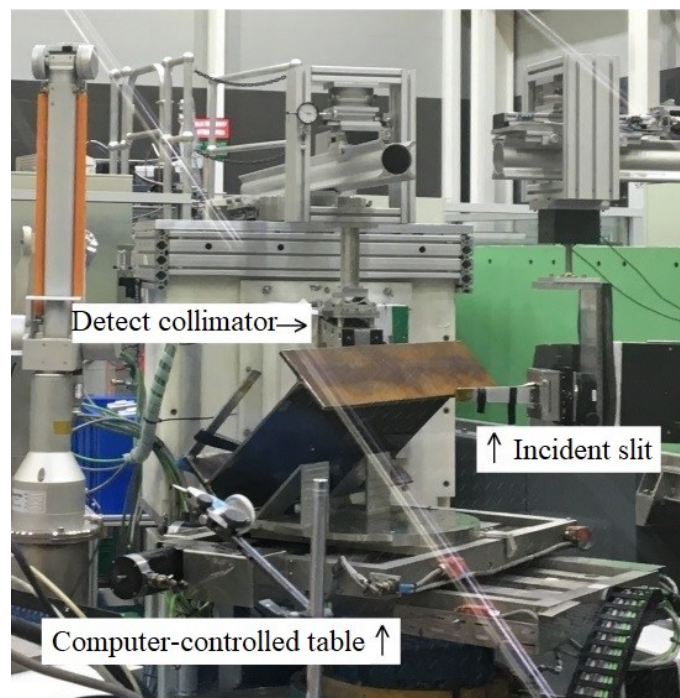
Figure 3.11: Tensile coupon test.



Figure 3.12: Tensile coupons of 12 mm BISPLATE-100 plates.



(a)



(b)

Figure 3.13: Test set-up (a) SScanSS for virtual sample and test simulation, and (b) sample positioned in the Kowari neutron diffraction strain scanner.

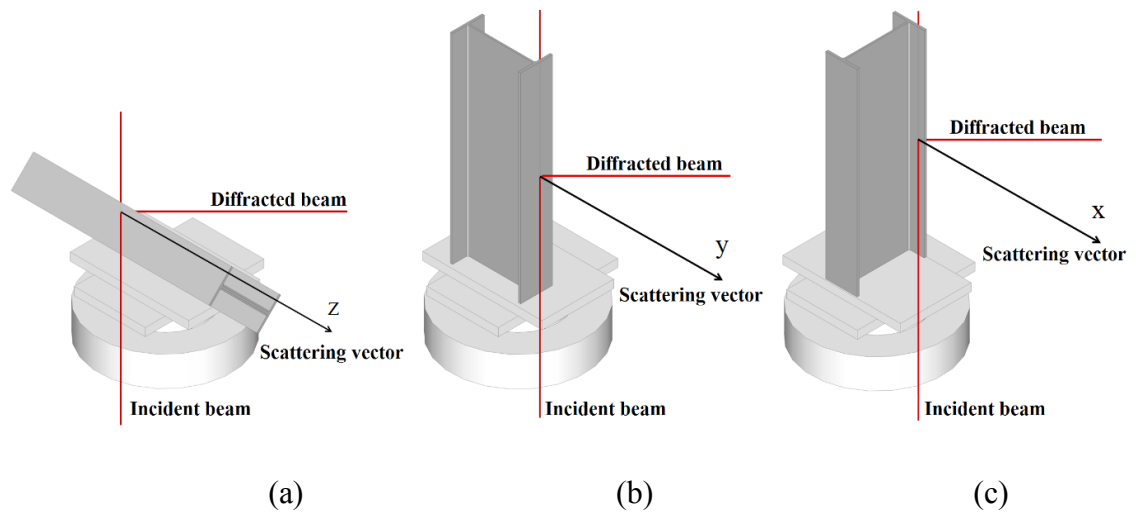


Figure 3.14: Orientation program for scanning residual strains in the flange, (a) longitudinal, (b) through-thickness, and (c) transverse direction.

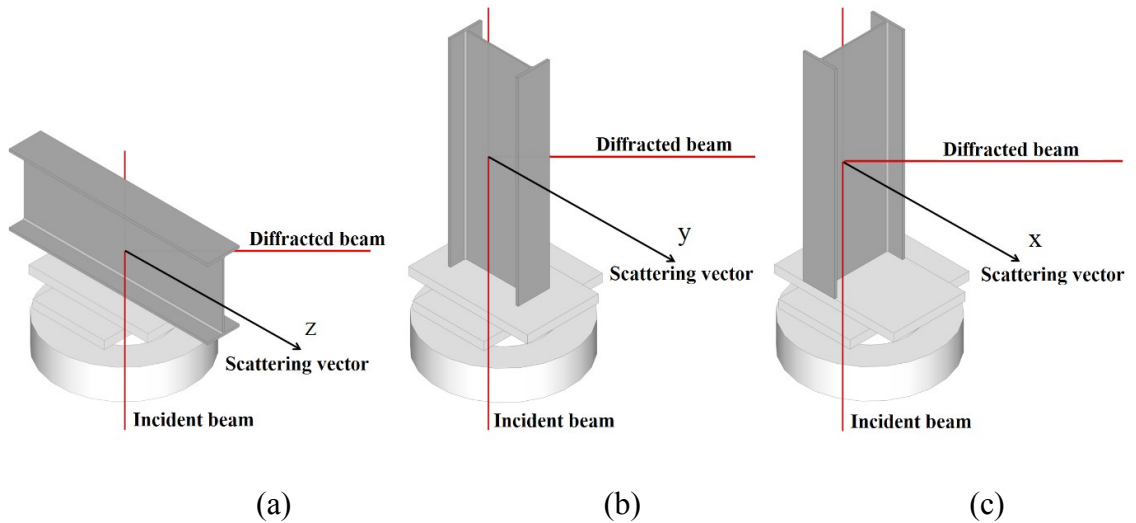


Figure 3.15: Orientation program for scanning residual strains in the web, (a) longitudinal, (b) transverse, and (c) through-thickness direction.

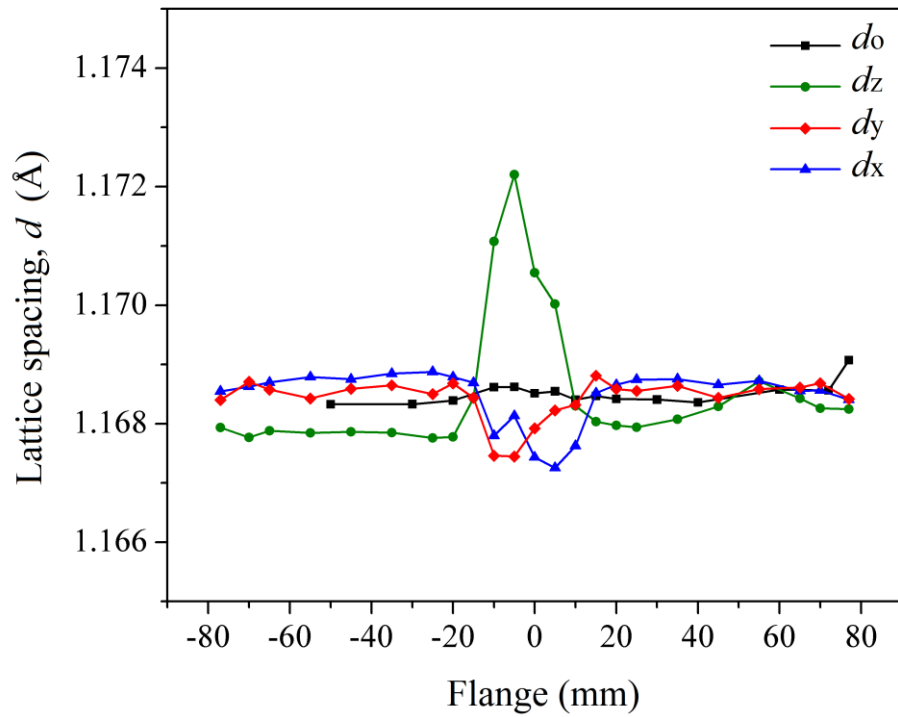


Figure 3.16: Lattice spacing in the flanges of BISPLATE-100 stress-free sample and of specimen RS-I-890.

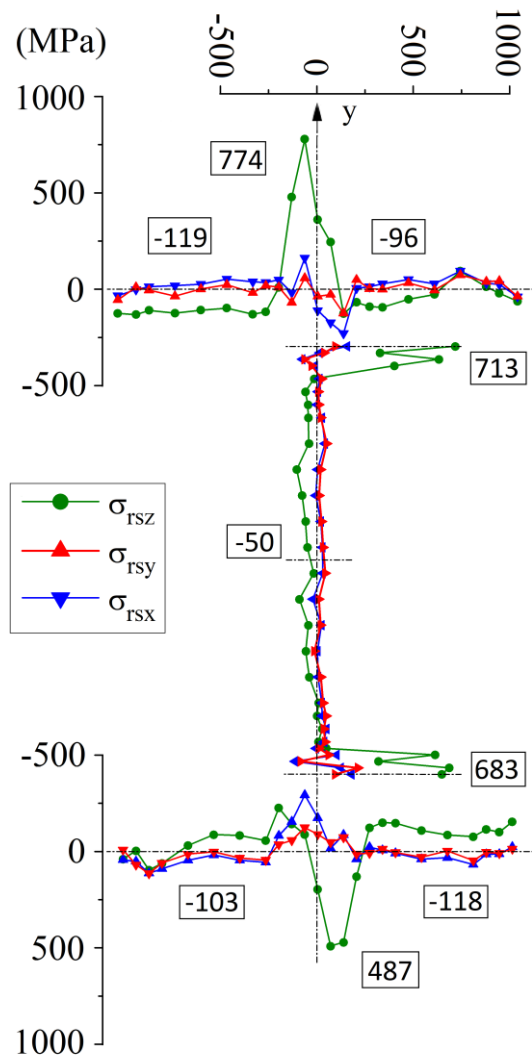


Figure 3.17: Residual stresses in specimen RS-I-890.

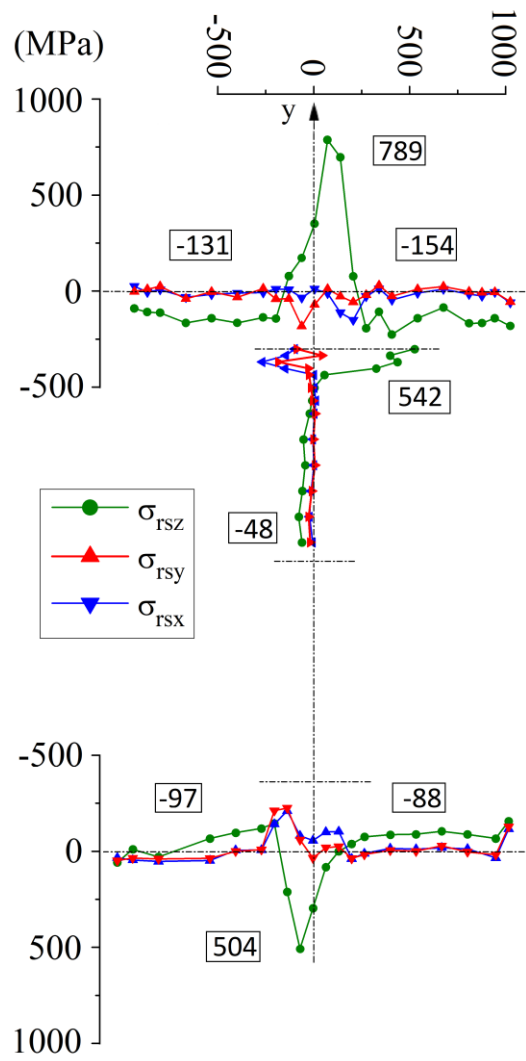


Figure 3.18: Residual stresses in specimen RS-I-690.

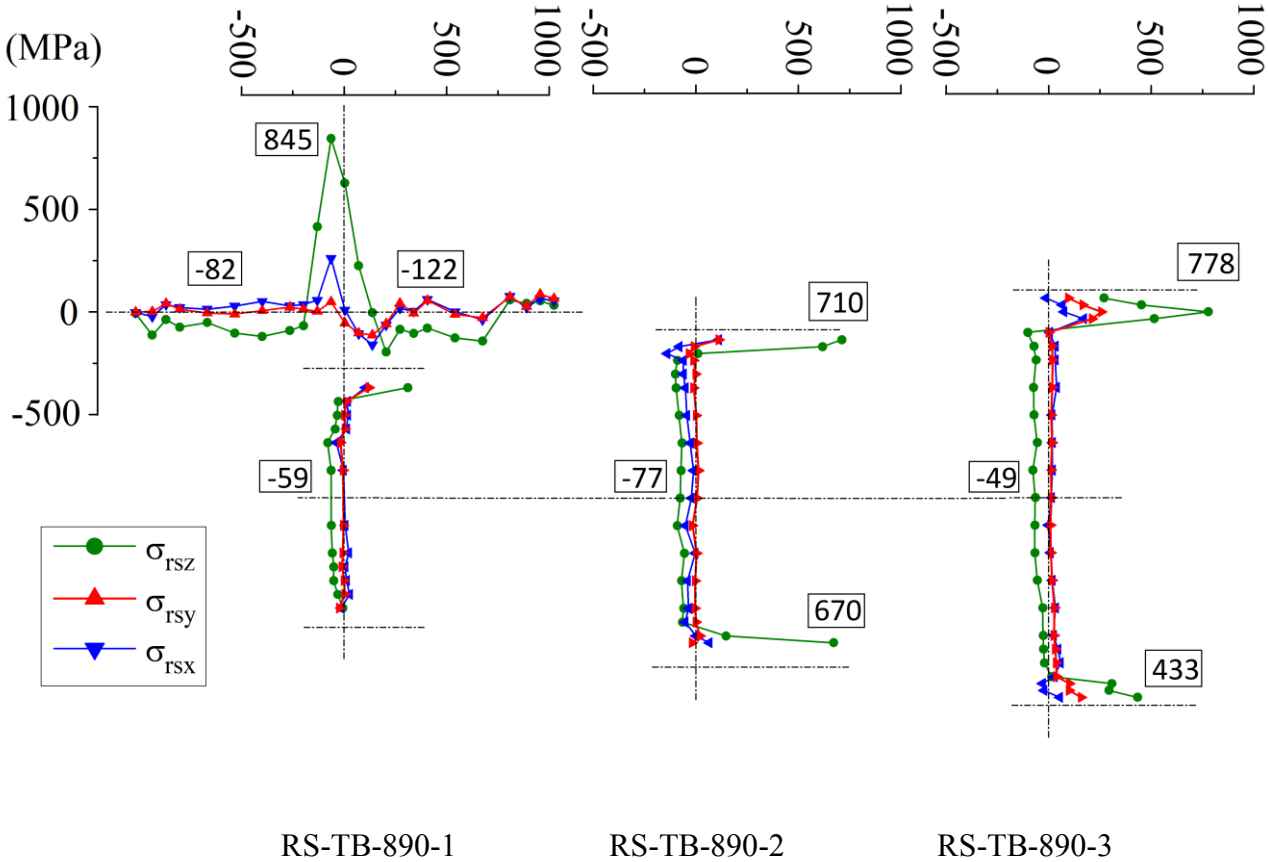


Figure 3.19: Residual stresses in specimen RS-TB-890.

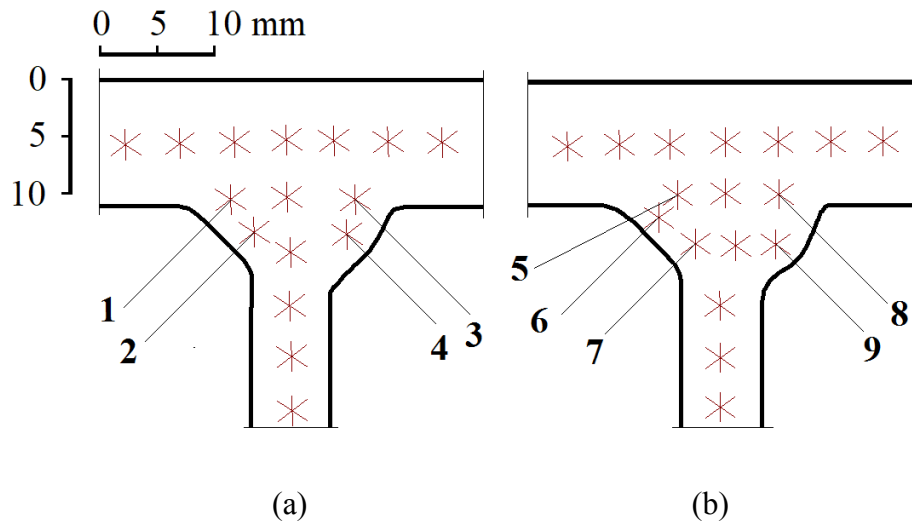


Figure 3.20: Measurement positions in the weld beads of specimen RS-I-890, (a) top flange-web, and (b) bottom flange-web intersection.

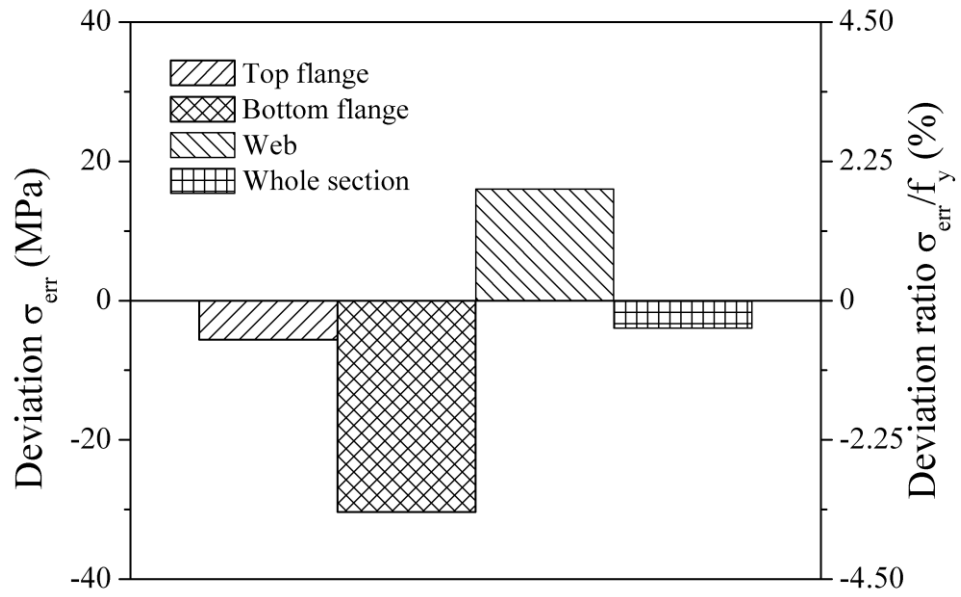


Figure 3.21: Residual stress self-balancing deviation in specimen RS-I-690.

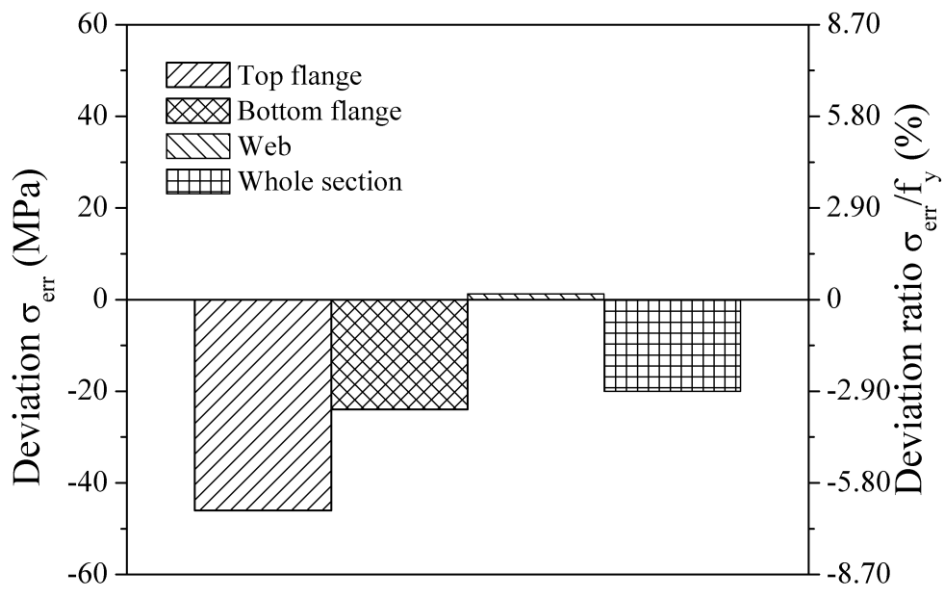


Figure 3.22: Residual stress self-balancing deviation in specimen RS-I-890.

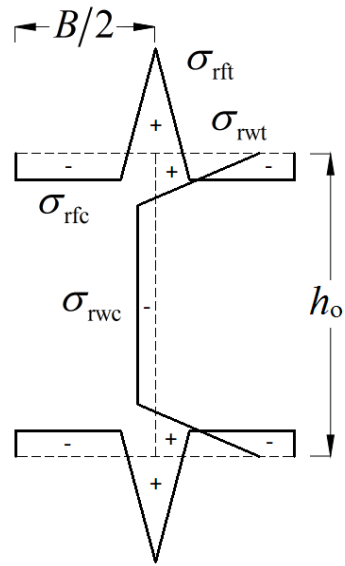


Figure 3.23: Proposed residual stress model.

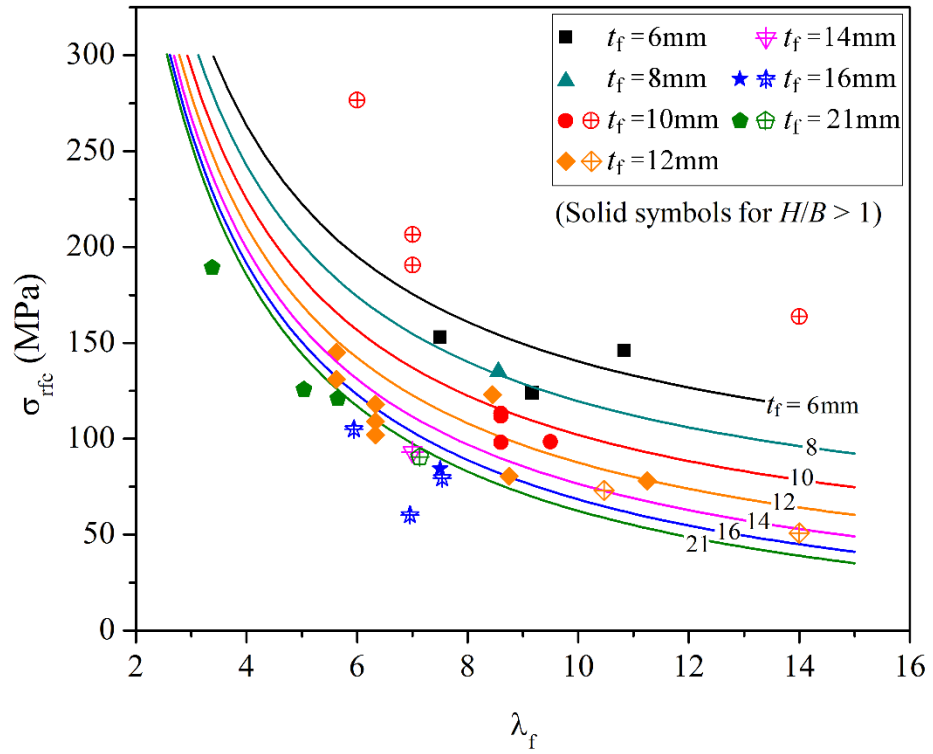


Figure 3.24: Compressive residual stress in the flange.

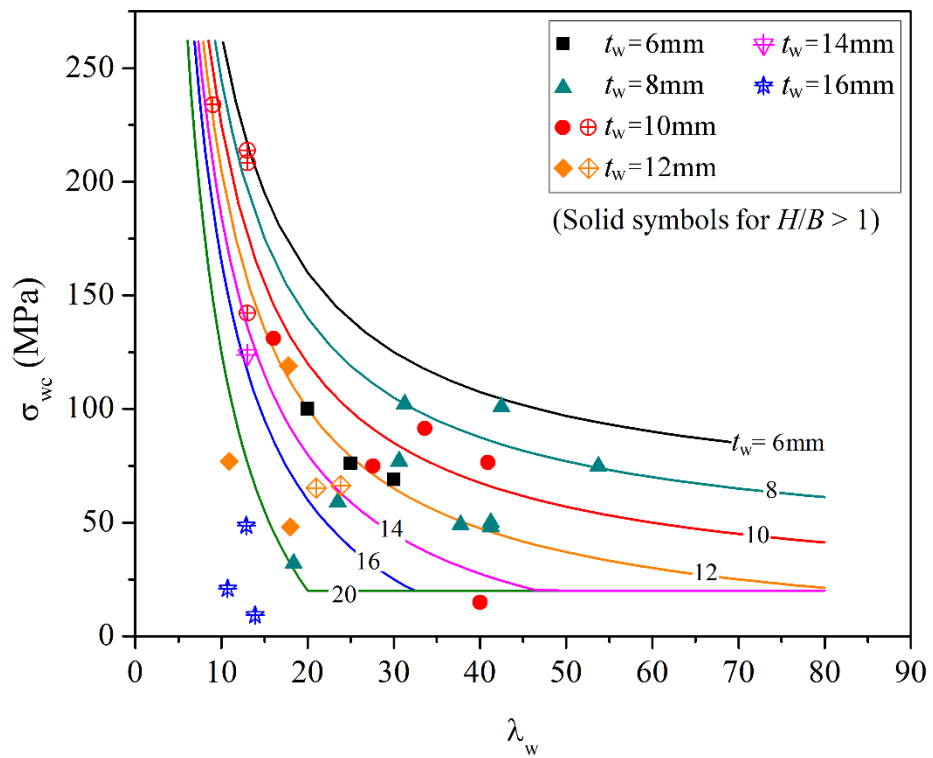


Figure 3.25: Compressive residual stress in the web.

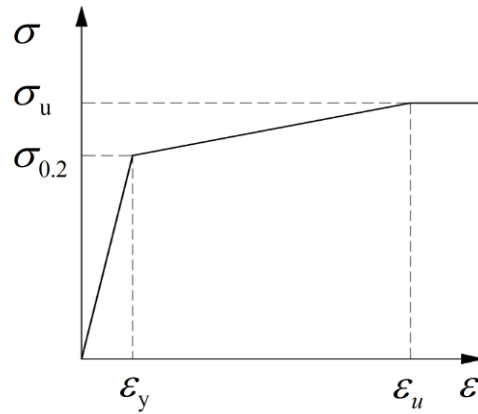


Figure 3.26: Material model.

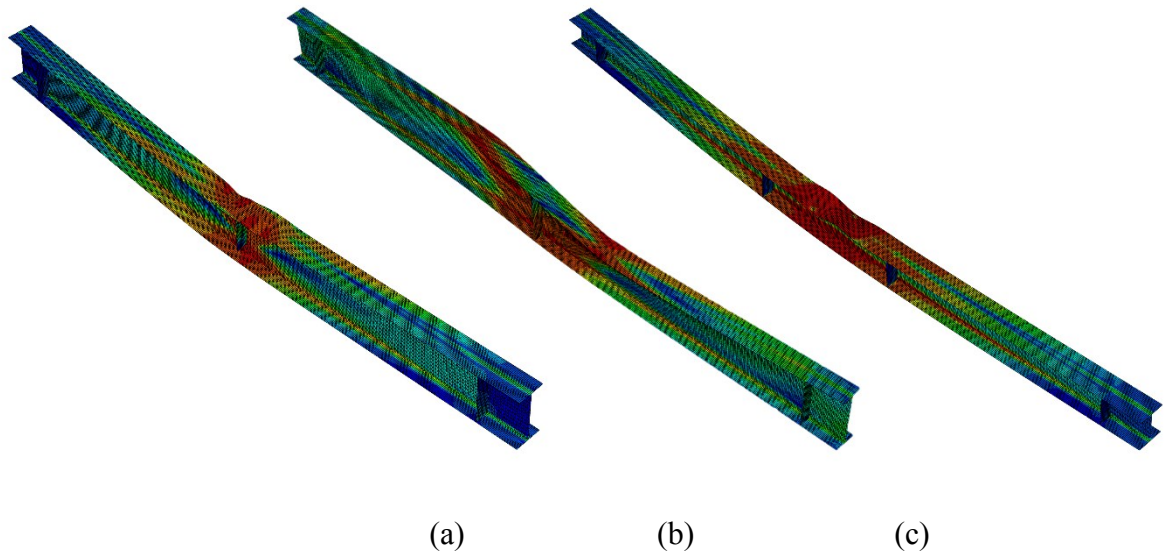


Figure 3.27: Deformed configurations of the specimens at failure in the numerical simulation: (a) specimen HSA800-II-6, (b) specimen Q460GJ-C5, and (c) specimen NIONICRAL70-E.

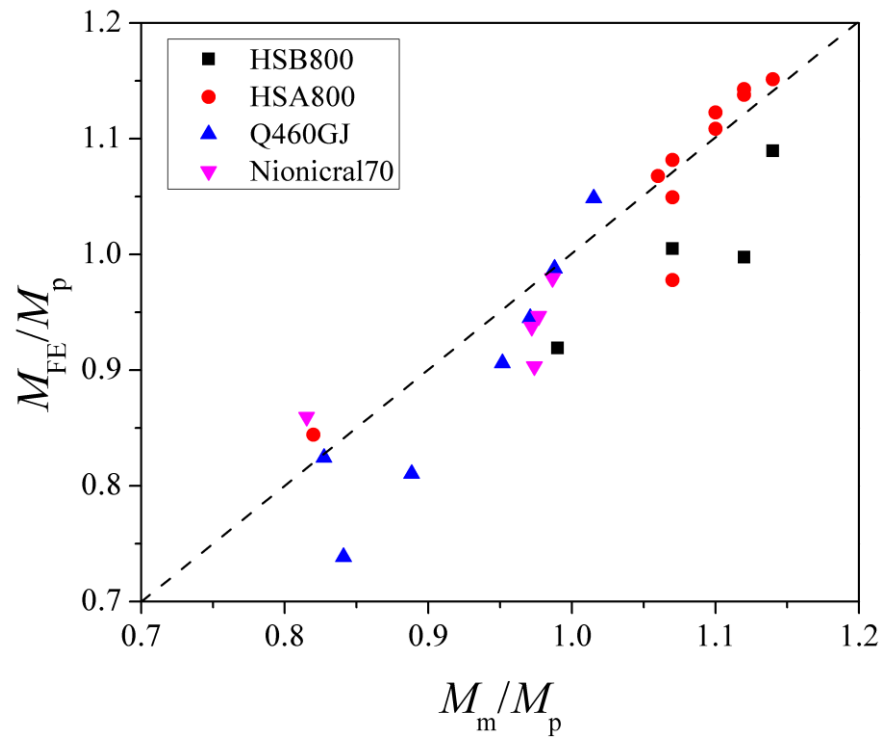


Figure 3.28: Finite element results versus test data.

CHAPTER 4 BUCKLING OF WELDED HIGH-STRENGTH STEEL I-BEAMS

4.1. Introduction

The replacement of mild steel with high-strength steel (HSS) is gaining popularity in the construction industry as contemporary HSS offers superior strength, excellent weldability, acceptable ductility and high notch toughness. With typical nominal yield strengths f_y being from 460 MPa up to 1000 MPa, HSS is double to triple the yield strength of mild steel ensuring lighter structures with more useable and saleable space, lower erection costs and smaller carbon footprints. However, very few studies of the flexural strength of HSS members with yield strengths in excess of 500 MPa can be found, and research findings on the lateral-torsional buckling of HSS beams are very limited with no experiments being reported on HSS beams with steel grades higher than 690 MPa.

This chapter presents experiments and numerical studies on the buckling of welded HSS I-section beams. Eight homogeneous beams are fabricated by welding from Australian BISPLATE-80 ($f_y = 690$ MPa or 100 ksi) and BISPLATE-100 ($f_y = 890$ MPa or 130 ksi) structural plates and tested under uniform bending and linear bending conditions. The specimens are designed to develop either lateral-torsional buckling or flange local buckling. The design procedures for the buckling resistance of a member in bending established in ANSI/AISC360-16 (2016), EC3 (2005) and AS4100-1998 (2016) are

addressed. An ABAQUS (2014) finite element model of the beams is constructed and calibrated against the tests and used to provide parametric studies that underpin a design proposal based on a generalised buckling strength formula consistent with the AS4100.

4.2. Experimental program

4.2.1. Specimen preparation

Eight full-scale homogeneous I-beams were built-up from BISPLATE-80 (I-690) and BISPLATE-100 (I-890) flame-cut plates, according to the specifications of AS/NZS 1554.4 (2010). Nominal 8 mm plates were used for the web and 12 mm plates for the flange. The cross-section of the specimens is outlined in Figure 4.1 and the actual dimensions are provided in Table 4.1. The geometry of specimens is depicted in Figures 4.8 and 4.9 with parameters given in Table 4.2. Gas metal arc welding with the specifications in Table 3.3 was used for fabricating the HSS beams.

The fabrication procedure is shown in Figure 4.2. Firstly, the plate components were aligned and preassembled by tack welds and steel rods. A preheat temperature of about 150 °C was then applied in the weld region with two accredited welding technicians simultaneously welding the flange to the web on opposite sides in order to reduce the distortion caused by an unbalanced transfer of heat. Continuous welding was performed at one flange fully then the beam was flipped over to complete welding of the other flange. Neither the component plates nor welded beams were required to be straightened. Web stiffeners were cut from the same parent plate of the web and positioned 200 mm away from the beam ends. The weld filler material was AWS A5.28:ER110S-1:2005 (2015), having a nominal yield stress of 660 MPa and tensile strength of 760 MPa. A magnetic particle inspection was carried out on the welds for

all specimens and no rejectable surface discontinuities were detected. Figure 4.3 shows some of uniform I-beams after welding.

Two residual stress specimens RS-I-690 and RS-I-890 were prepared for examining residual stresses induced in HSS I-section beams. Figure 4.4 illustrates the locations of residual stress samples saw-cut from the welded beams, parts of which are I-690-2 and I-890-2 specimens. A picture of the samples is presented in Figure 3.7 with the measured dimensions given in Table 3.1. The actual geometry of these specimens has been simulated using a laser scanner incorporated with the simulation software “SScanSS” (Figure 3.13a) and the mid-spans of the residual stress samples are plotted in Figure 4.5 on a square grid of 10×10 mm. It can be seen that the specimens were well fabricated with tolerances within the limits imposed by the AS4100-1998 (2016) specification.

4.2.2. Material properties

A tensile coupon test in accordance with AS1391 (2007) to determine the material characteristics of the parent plates from which the I-beams were fabricated was presented in Section 3.3.2 with the typical stress-strain curves shown in Figure 3.10 and the mechanical properties given in Table 3.2.

4.2.3. Residual stresses

The samples RS-I-690 and RS-I-890 were measured for their residual stress distributions using the non-destructive neutron diffraction method. Details of the RS measurement are presented in Chapter 3. The longitudinal residual stresses at the mid-span of these samples are compared in Figure 4.6. It is seen that the tensile residual stress peaks at the flange-web intersection, whilst the compressive residual stress is

approximately uniform across a large central portion of the flange including the flange tips and across a large central portion of the web. The magnitude of the compressive stress appears to be independent of the base metal strength, and the pattern can be represented by the model shown in Figure 3.23, with the average tensile and compressive stress values summarised in Table 4.2.

4.2.4. Geometric imperfection

The out-of-plumb imperfections of the I-beam were inspected using a laser level having an accuracy of ± 0.3 mm/m to create a cross baseline and a right-angle ruler having a smallest scale division of 0.5 mm to measure the distance from the flange tips to the base line; the concept was adopted from Xiong *et al.* (2016). Details of the set-up and locations used for measuring the out-of-plumbness are illustrated in Figures 4.7 and 4.8. Readings were taken at the beam ends (d_{a1} , d_{a5}) and quarter points (d_{a2} , d_{a3} , d_{a4}) as shown. The distance from the central line connecting the flange centres at the beam ends to the flange tip at a measurement location can then be obtained from

$$D_{ai} = d_{ai} - \left[(5-i)d_{a1} + (i-1)d_{a5} \right] / 4, \quad i \in [1, \dots, 5]. \quad (4.1)$$

Repeating the measurements for the three other sides of the top and bottom flanges leads to (D_{bi} , D_{ci} , D_{di}), with the average out-of-plumbness at a cross-section calculated from

$$D_1 = (D_{ai} + D_{bi} + D_{ci} + D_{di}) / 4, \quad i \in [1, \dots, 5]. \quad (4.2)$$

The largest deviation at the inspected cross-sections $D_{i,\max}$ was taken as the magnitude of the out-of-plumb imperfection given in Table 4.3 for all specimens. Based on this

measurement technique, the imperfection varied from 1.75 mm to 2.5 mm, which were smaller than the limit of span/1000 or 3 mm specified in AS4100.

The flange and web tilt imperfections were not inspected in this experiment and the tolerance limits specified in AS4100 were employed in the subsequent numerical modelling.

4.2.5. Buckling test set-up

In order to generate and apply a pair of external bending moments at the two ends of a segment under test, two arrangements corresponding to a three-point and a four-point loading test were considered in Figures 4.9 and 4.10 respectively. Four-point loading was used to generate uniform moment (UM) ($\beta = -1$) and three-point loading to generate linear moment gradient (MG) ($\beta = 0$) with details of the load parameters provided in Table 4.3.

The loading and restraint system was developed from the studies of Dux and Kitipornchai (1983) and Xiong et al. (2016). The loads were transferred from the computer-controlled hydraulic actuators onto the beam through special loading boxes which allowed the beam to rotate freely about the major and minor axes and to warp and move downward, but which restrained the beam against lateral deflection and twist.

The loading box is depicted in Figure 4.11 with the assembling process shown in Figure 4.12, the movement of the box being guided by a set of two universal columns which were assembled into a frame system and firmly braced as seen in Figures 4.9 and 4.10.

Rollers were utilised at the contact positions to minimise friction. Similarly, the end supports shown in Figure 4.13 were such that beam end twist and lateral deflection were

prevented but warping and rotation about the major and minor axes as well as movement in the axial direction were allowed.

The hydraulic actuators of capacity 500 kN were set to load control and then to displacement control. Load control was operated firstly at a rate of 6 kN/min until 80% of the estimated critical load was reached, following which displacement control at 0.5 mm/min was used until buckling. The unloading rate was 2 mm/min. Prior to the actual test, loading to 20% of the estimated critical load was undertaken to ensure that the setup functioned correctly.

4.2.6. Instrumentation

Linear variable differential transformers (LVDTs) and strain gauges (SGs) were utilised for the displacement and strain measurements. The layout and location of the LVDTs along the beam and the SGs mounted on the I-section are shown in Figures 4.14 and 4.15, respectively.

In addition, two pairs of draw-wire transducers (DW) were employed to track the deformation of the beam in space due to the coupling of the lateral and twist displacements. One pair was used to measure the movement of the centroid and the other to track the top flange. Figure 4.16 shows the arrangement and location of the DW transducers.

4.3. Test results and discussion

The evolutions of the load-displacement relationships are plotted in Figure 4.17 and the buckling moment M_m and failure modes are given in Table 4.3. The test set-up

successfully allowed the local and global buckling responses of the HSS I-beam specimens to be investigated.

In general, under the same initial configuration and loading, specimens with the higher steel grade (I-890) had higher buckling resistances (Figures 4.17a to 4.17f) than those with the lower steel grade (I-690). It is also seen from Table 4.3 and Figure 4.23 that the non-dimensional buckling resistances of the BISPLATE-100 beams are slightly higher than those of the BISPLATE-80 beams.

Specimens I-890-3 and I-890-4 in Figures 4.17f and 4.17g show that the buckling strength increases with an increase of the flange width because of the increase of the minor axis second moment of area and of the warping constant. On the other hand, as the web depth decreases (I-890-4 vs I-890-5) in Figures 4.17g and 4.17h, the buckling strength decreases, but I-890-5 with the ultra-compact web buckled at a noticeably greater transverse deflection.

The compression flange strain versus mid-span bending moment of the beams is plotted in Figure 4.18, which shows that all specimens (except I-690-2 and I-890-2) buckle well below attaining their first yield bending moment $M_y = f_y Z_x$ (Z_x being the section elastic modulus). Comparing SG-1 and SG-3 shows that as the beam deflects out-of-plane, the strains in the compression flange in one flange tip reduce to become tensile, while those in the other flange tip increase rapidly.

The specimen buckling modes are shown in Figure 4.19, with distinct lateral-torsional buckling (LTB) and flange local buckling (FLB) being identified. The LTB mode under UM was slightly different to that under MG. In the case of FLB shown in Figure 19c, beams I-690-2 and I-890-2 responded elastically before the yield moment M_y was

attained. This is consistent with the bending moment versus bottom flange transverse displacement plotted in Figures 4.17c and 4.17d. The onset of yielding occurs below M_y because of the effects of residual stresses, and these can lead to early bifurcation of the strength curve from the linear part owing to inelastic buckling. The effects of residual stresses are less pronounced for the higher strength steel I-890-2 compared with I-690-2 as the yield point is closer to the nominal yield moment M_y , as in Figures 4.18c versus 4.18d. In particular, in specimen I-690-2 yielding occurs around $-3600 \mu\epsilon$ and FLB around $-5800 \mu\epsilon$, while in I-890-2 yielding occurs around $-4500 \mu\epsilon$ and FLB around $-7000 \mu\epsilon$.

In the beams under linear bending moment gradient, e.g. I-690-1 and I-890-1, lateral-torsional buckling occurred, and the lateral deflection evolved symmetrically about the mid-span (Figure 4.19b). The deformations of a cross-section (including the centroid and top flange centre) distant $L/6$ from the mid-span versus loading for specimens I-690-1 and I-890-1 are shown in Figures 4.17a and 4.17b, respectively. Regardless of the effect of the out-of-plumb imperfection (which in I-890-1 was little less than that of I-690-1), the effect of the residual stresses on the buckling resistance of specimen I-690-1 (of lower grade steel) was more significant than that of specimen I-890-1 (of higher grade steel). This is because the compressive residual stresses in the two specimens had similar magnitudes as shown in Figure 4.7. The compressive residual stresses were independent of the steel grade, leading to the partial yielding at the critical cross-section earlier in the case of the member made of the lower grade steel (I-690-1). Similar results can be seen in the global buckling behaviour of the specimens under uniform bending moment. Again, the higher buckling resistance was obtained in specimen I-890-3 compared to specimen I-690-3 (Figures 4.17e and 4.17f). It is noticeable that the maximum compressive strain at a flange-tip at the buckling moment was $-3860 \mu\epsilon$ for

specimen I-690-3 (Figure 18e) and $-5100 \mu\epsilon$ (Figure 18f) for specimen I-890-3. These strains were approximately equal to the strains at which partial yielding of specimens I-690-2 and I-890-2 commenced. Similarly, the maximum compressive strains at the critical load in specimens I-890-4 and I-890-5 were $-4150 \mu\epsilon$ and $-4270 \mu\epsilon$ respectively. Accordingly, it can be concluded that for the compact or non-compact beams, when the compression flange starts to yield, the beam fails by inelastic lateral buckling if it has insufficient lateral restraint. On the other hand, if the beam is restrained against lateral deflection, it exhibits higher strength due to the onset of strain-hardening until the full plastic moment or flange local buckling is attained.

High-strength steel becomes more brittle with an increase of steel grade and tensile fracture has been observed in some tests for the flexural strength of HSS beams (McDermott, 1969; Lee *et al.*, 2012). Accordingly, whether the buckling deformation of the beams having yield strengths exceeding 690 MPa is accompanied by tensile fracture is questionable. In this experiment, no tensile fracture occurred at buckling and during postbuckling deformation of the specimens.

4.4. Numerical study

4.4.1. Finite element model

To augment the experimental data, 3-dimensional finite element models (FEMs) for thin-walled I-beams were constructed using ABAQUS software (2014) and calibrated against the tests. Two numerical models, viz. a full-scale test simulation (FEM-1) and a simple generic approach (FEM-2) with a variable effective length L_e were considered as shown in Figure 4.20.

For the simpler generic treatment for lateral-torsional buckling, appropriate constraints adapted from (Bradford and Liu, 2016) were imposed at the end supports to avoid stress concentrations and undesirable localised deformations due to the concentrated moment applied there. The displacements of a position along the web (W) are related to the displacements of the web centroid (Wc) as

$$\phi_x^W = \phi_x^{Wc} \quad (4.3)$$

and

$$u_z^W = u_z^{Wc} + y\phi_x^{Wc} \quad (4.4)$$

with the displacements of a position along the top flange (TF) and bottom flange (BF) being related to the displacements of the top flange centroid (TFc) and bottom flange centroid (BFc) by

$$\phi_y^{TF} = \phi_y^{TFc}, \quad (4.5)$$

$$u_z^{TF} = u_z^{TFc} + x\phi_y^{TFc}, \quad (4.6)$$

$$\phi_y^{BF} = \phi_y^{BFc}, \quad (4.7)$$

$$u_z^{BF} = u_z^{BFc} + x\phi_y^{BFc}, \quad (4.8)$$

where u_x , u_y and u_z are the displacements in the global x , y , z directions and ϕ_x , ϕ_y , and ϕ_z the rotations about the global x , y , z axes respectively. For a generic beam that allows for flange local buckling, the counterpart constraints are

$$\phi_x^{\text{TF}} = \phi_x^{\text{TFc}}, \quad (4.9)$$

$$u_z^{\text{TF}} = u_z^{\text{TFc}}, \quad (4.10)$$

$$\phi_x^{\text{BF}} = \phi_x^{\text{BFc}}, \quad (4.11)$$

$$u_z^{\text{BF}} = u_z^{\text{BFc}}. \quad (4.12)$$

It is known that the critical segment of a braced beam gets a degree of rotational restraint about the minor axis from its adjacent segment (Trahair and Bradford, 1998; Trahair *et al.*, 2007; Trahair, 2014). Therefore, the effective length used in the simple generic model needs to be modified by a rotational restraint factor k_r , as shown in Figure 4.21. The value of k_r can be determined by the method of design by buckling analysis in which $k_r = L_{oc}/L_o$, in which L_{oc} is the length of a simply supported beam which has the same cross-section and results in a similar elastic buckling load to that of the braced beam under uniform bending. The rotational restraint factors k_r adopted in the simple generic models are given in (Trahair and Bradford, 1998; Trahair *et al.*, 2007).

Due to the absence of a significant yield plateau, a multi-linear elastic-plastic constitutive law in Figure 4.22 with von Mises' yield criterion, associated plastic flow rule and isotropic hardening was used for high-strength steels having material properties in Table 3.2. The elastic modulus was taken as $E = 200$ GPa and Poisson's ratio as $\nu = 0.25$ with respect to AS4100-1998 (2016).

The measured imperfections including the out-of-plumbness and residual stresses were integrated in the test simulation of specimens based on which the FE models were

calibrated. Where measured values for the geometric imperfections are not available, the variation of the beam geometry and its imperfection can be represented by adopting the guidance in the AS4100 specification. For this, the maximum value of the out-of-plumb magnitude of 1/1000 of the span length or 3 mm, whichever is larger, is applied in the lateral-torsional buckling modelling. The imperfection shape was taken as the fundamental eigenmode from an elastic buckling analysis. For the flange local buckling, the imperfection shape was also taken as the local elastic buckling eigenmode with the maximum magnitude being 3 mm, which is the maximum value imposed by AS4100 for sectional dimensions listed in Table 4.5.

Apart from the cross-sections having similar dimensions to the samples RS-I-690 and RS-I-890, the residual stress pattern in Figure 3.23 was used in the parametric study, with the magnitude of the tensile and compressive stresses obtained from Eqs. (3.7) to (3.9).

4.4.2. Validation of FEM

The maximum flexural load carrying capacities M_b of the specimens obtained from the FE simulations are shown and compared with the maximum experimental bending moment capacities M_m in Table 4.3. The FE results are in good agreement with the test results with an average error of 6% for both FE models, with the standard deviations of both models being 7%. The accuracy of the FE results is also demonstrated in Figure 4.23, which depicts the normalised bending moment (M/M_p) plotted against the normalised displacement curves u_x/H or u_y/H obtained from the full-scale FE model and the test results. The buckled deformations of the I-beams captured by the two FE models correlate reasonably well as shown in Figure 4.24.

The simple generic FE representation (Figure 4.20b) was employed to conduct a parametric study for beams having similar cross-sections to the test specimens as listed in Table 4.5 with the length of the beam and bending moment regime over the length (uniform bending and linear bending moment gradient) being the main variables. Comparisons between the results obtained from the generic FE model and national design standards are presented in the following section with revisions in the design standards being proposed.

4.5. Comparison of test results and FE model with design standards

4.5.1. ANSI/AISC 360-16

In the American ANSI/AISC 360-16 (2016), the nominal flexural strength M_n of doubly symmetric compact and non-compact flange I-shaped beams bent about their major axis is the least of the following three bending moment capacities.

(a) The limit state of the plastic moment given by

$$M_{nP} = M_p = f_y S_x, \quad (4.13)$$

where S_x is the plastic section modulus.

(b) The limit state of compression flange local buckling given by

$$M_{nFLB} = M_p - \left(M_p - 0.7 f_y Z_x \right) \left(\frac{\lambda_r - \lambda_{pf}}{\lambda_{rf} - \lambda_{pf}} \right), \quad (4.14)$$

where Z_x is the elastic section modulus, $\lambda_r = B/(2t_f)$, and λ_{pf} and λ_{rf} are the compact and non-compact flange slenderness limits, respectively.

(c) The limit state of lateral-torsional buckling as

$$M_{nLTB} = \begin{cases} C_b \left[M_p - (M_p - 0.7f_y Z_x) \left(\frac{L_o - L_p}{L_r - L_p} \right) \right] & L_p < L_o \leq L_r \\ M_{ob} & L_o > L_r, \end{cases} \quad (4.15)$$

where L_o is the unbraced length, L_p and L_r the unbraced length limits for the yielding and inelastic lateral-torsional buckling limit states respectively, C_b the non-uniform moment modification factor, and M_{ob} the elastic lateral-torsional buckling bending moment.

Comparisons between the test results and the ANSI/AISC 360-16 provisions are presented in Figure 4.25. It is seen that the ANSI/AISC marginally estimates the buckling strength of specimens in both loading conditions, i.e. uniform moment ($\beta = -1$ and $C_b = 1$) and linear moment gradient ($\beta = 0$ and $C_b = 1.75$). However, the ANSI/AISC curves seem to overestimate the FE predictions in the inelastic portions as seen in Figure 4.26. The test data for lateral-torsional buckling of Q460GJ ($f_y = 460$ MPa) beams provided by Xiong et al. (2016) also showed that the ANSI/AISC was unsafe in the case of moment gradient loading. Recently, Subramanian and White (2016a, 2016b, 2107) addressed that the discrepancy between experiments and FE models are due to the use of nominal values of residual stresses and geometric imperfections and that the inelastic effective length effects are not commonly considered in test simulations. Subramanian and White (2016b) also indicated that the ANSI/AISC provisions are unconservative in the inelastic lateral-torsional buckling region even for mild steel beams under moment gradient loading where the ANSI/AISC curve is scaled by the modification factor C_b derived based on elastic solutions.

Accordingly, more experimental and numerical studies for inelastic buckling of high-strength steel beams are needed before a revision to ANSI/AISC can be suggested.

4.5.2. Eurocode 3

In the EC3 (2005), the nominal flexural-torsional buckling moment capacity M_b is calculated from

$$M_b = \chi_{LT} M_s, \quad (4.16)$$

where M_s is the nominal section bending moment capacity, χ_{LT} the reduction factor for flexural-torsional buckling given by

$$\chi_{LT} = \frac{1}{\Phi_{LT} + \sqrt{\Phi_{LT}^2 - \beta \bar{\lambda}_{LT}^2}} \leq 1, \quad (4.17)$$

with $\bar{\lambda}_{LT} = \sqrt{M_s / M_{ob}}$ being the modified slenderness and

$$\Phi_{LT} = 0.5 \left[1 + \alpha_{LT} (\bar{\lambda}_{LT} - \bar{\lambda}_{LT,0}) + \beta \bar{\lambda}_{LT}^2 \right]. \quad (4.18)$$

EC3 provides two tiers of design with counterpart sets of coefficients for use with these equations. These two methods include a simple but conservative one for general members, and a less conservative method for rolled sections and equivalent welded sections. For the simple general method, $\bar{\beta} = 1.0$ and $\bar{\lambda}_{LT} = 0.2$, while for the less conservative method, $\bar{\beta} = 0.75$ and $\bar{\lambda}_{LT} = 0.4$. The value of the imperfection factor α_{LT} is a function of the height-to-width ratio H/B ratio and the type of cross-section. In the less conservative method, for further taking the effect of the moment distribution into account, the reduction factor χ_{LT} is modified according to

$$\chi_{LT,mod} = \chi_{LT}/f \leq 1 \quad (4.19)$$

with

$$f = 1 - 0.5(1 - k_c) \left[1 - 2.0(\bar{\lambda}_{LT} - 0.8)^2 \right] \leq 1 \quad (4.20)$$

and the correction factor $k_c = 1/\sqrt{\alpha_m}$, where α_m is the moment modification factor.

The experimental results and the EC3 model are compared in Figure 4.27, and the generic FE model and EC3 are compared in Figure 4.28. The most conservative beam curve for rolled sections and equivalent welded sections, viz. EC3 (d) ($\bar{\beta} = 0.75$ and $\bar{\lambda}_{LT} = 0.4$) provides a good approximation to the buckling resistance of the HSS beams under uniform bending moment when the beam slenderness $\bar{\lambda}_{LT}$ is less than unity. For a beam slenderness greater than this, the EC3 estimation of the bending moment capacity is conservative for both bending moment regimes, i.e. uniform and a linear gradient. The gap between the EC3 predictions and the bending moment capacity M_b of the HSS beams becomes more evident in the case of bending moment gradient.

4.5.3. AS4100

In the Australian AS4100-1998 (2016), the nominal buckling bending moment capacity of I-section beams is obtained from

$$M_b = \alpha_m \alpha_s M_s, \quad (4.21)$$

where α_m is the moment distribution modification factor and α_s the slenderness reduction factor that can be obtained from

$$\alpha_s = 0.6 \left(\sqrt{\lambda_s^4 + 3} - \lambda_s^2 \right) \leq 1, \quad (4.22)$$

where $\lambda_s = \sqrt{M_s/M_{oa}}$ is the modified slenderness and M_{oa} the reference elastic buckling bending moment excluding the effect of non-uniform moment distribution.

The comparisons of the test results and the generic FE model predictions with the AS4100 specifications are provided in Figures 4.29 and 4.30 respectively. It is seen that the Australian design provisions can be used to estimate the bending moment capacity of the stocky ($\lambda_s \leq 1.0$) HSS beams with reasonable accuracy. However, the AS4100 procedure is overly conservative for the bending moment capacity of intermediate and slender ($\lambda_s > 1.0$) HSS beams.

4.6. Revision to AS4100 for high-strength steels

In order to reduce the gap between the AS4100 model and the generic FE results and to provide a more accurate prediction of the bending moment capacity for intermediate and slender beams, a modification to the slenderness reduction factor formula is proposed by incorporating a coefficient γ_m into the expression for α_s according to

$$\alpha_s = \left[\sqrt{\gamma_m^2 \lambda_s^4 + \left(1 - \frac{0.6}{\gamma_m} \right) \lambda_s^2 + 1.08} - \gamma_m \lambda_s^2 \right] \leq 1. \quad (4.23)$$

The coefficient γ_m accounts for material characteristics of high strength steels.

The bending moment capacity in Eq. (4.21) then takes the form

$$M_b = \alpha_m \alpha_s M_s \leq \min \{ M_{ob}, M_s \}. \quad (4.24)$$

For the HSS beams with nominal yield stress greater than 690 MPa, the suggested value for γ_m is 0.7, whereas with $\gamma_m = 0.6$ the Eq. (4.23) returns to the original Eq. (4.22) which is applicable for flexural members made of mild steel. The good correlation between the bending moment capacity M_b obtained from the modified model (Eqs. (4.23) and (4.24)) and the generic FE results is evident from the M_b/M_s versus λ_s plotted in Figures 4.31 and 4.32. In the case of uniform bending, the modified curve provides a lower bound for the results of generic FE model, which is the most critical loading case. However, in the case of linear bending moment gradient, the new model approximates the mean of the generic FE results with acceptable accuracy.

It is noteworthy that use of the material coefficient γ_m provides the AS4100 slenderness reduction factor α_m with versatility in adapting new steel grades. The value of γ_m addressing the variation of material properties is an interest for future studies.

4.7. Conclusions

An experimental study of the buckling behaviour of welded high-strength steel (HSS) I-section beams was carried out. Eight I-beams fabricated from BISPLATE-80 and BISPLATE-100 were tested under conditions of uniform bending and linear bending moment gradient. The special design of the test set-up for buckling of the I-beams was presented in detail, along with the results of material tests and imperfection measurements including residual stresses within the cross-section and the out-of-plumb magnitudes. The test design successfully captured the buckling response of the welded HSS I-beams, including their lateral-torsional buckling and flange local buckling failure modes. The versatility of the devised testing rig under different loading scenarios was also demonstrated. Finite element (FE) modelling of the HSS beams was carried out using ABAQUS software and good agreement between the FE and test results was

achieved. The FE models were then used to extend the experimental data by varying the beam slenderness and the adequacy of existing standard design provisions for predicting the bending moment capacity of HSS beams were evaluated. The following conclusions were drawn from the results of the laboratory experiments and the FE simulations.

- BISPLATE-100 beams have slightly higher normalised buckling resistances compared to BISPLATE-80 beams due to the less pronounced effects of the residual stresses in the higher-strength steel sections.
- The buckling strength of an I-section is related to the flange and web slenderness. Accordingly, an optimal cross-section for maximising the loading resistance and minimising material use can be obtained and should be considered in design practice.
- Because of the residual stresses, the onset of yielding can commence before attainment of the yield moment, leading to a non-linear response of the beam. The bending strength of the beam still increases due to the onset of strain-hardening until reaching the flange local buckling moment.
- The flexural-torsional buckling is related to partial yielding of the critical cross-section as the instability occurred when the stresses in the compression flange were non-linear.
- Tensile rupture did not occur in any of the specimens during the buckling tests.
- The ANSI/AISC 360-16 marginally approximates the buckling strength of HSS specimens but overly estimates the FE predictions. On the other hand, based on extended numerical data, the less conservative beam curve (d) of EC3 provides a good approximation of the buckling resistance of HSS stocky beams under uniform bending, but it is conservative in the cases of intermediate and slender beams, as

well as when the moment is distributed non-uniformly. The AS4100 closely estimates the bending strength of HSS stocky beams in both loading scenarios, but it too is conservative when the beam slenderness is greater than unity.

- A revision to the AS4100 has been proposed by introducing a coefficient γ_m related to the material characteristics of the steel into the slenderness reduction factor formula. The value $\gamma_m = 0.7$ is recommended for flexural members fabricated from HSS with nominal yield stresses greater than 690 MPa, while $\gamma_m = 0.6$ is applicable for mild steel flexural members.

Table 4.1: Specimen cross-section dimensions

No.	Notation	f_y (MPa)	H (mm)	B (mm)	t_f (mm)	t_w (mm)	b_f/t_f	h_w/t_w
1	I-690-1	690	354	160	11.77	7.70	6.47	42.92
2	I-690-2	690	354	160	11.77	7.70	6.47	42.92
3	I-690-3	690	354	160	11.77	7.70	6.47	42.92
4	I-890-1	890	354	160	11.80	7.95	6.44	41.56
5	I-890-2	890	354	160	11.80	7.95	6.44	41.56
6	I-890-3	890	354	160	11.80	7.95	6.44	41.56
7	I-890-4	890	354	120	11.80	7.95	4.75	41.56
8	I-890-5	890	254	120	11.80	7.95	4.75	28.98

Table 4.2: Average tensile and compressive residual stresses

Sample	f_y (MPa)	H (mm)	B (mm)	t_f (mm)	t_w (mm)	σ_{rft} (MPa)	σ_{rwt} (MPa)	σ_{rfc} (MPa)	σ_{rwc} (MPa)
RS-I-690	690	353.5	159.3	11.77	7.70	647	542	-118	-48
RS-I-890	890	352.9	159.5	11.80	7.95	631	698	-109	-50

Table 4.3: Buckling strength of high-strength steel beams of uniform cross-section

No.	Specimen	Slenderness*		Load case	L (m)	L_o (m)	L_1 (m)	$D_{i,max}$ (mm)	M_p (kNm)	M_m (kNm)	M_m/M_p	Failure mode
		Flange	Web									
1	I-690-1	NC	C	MG	7.0	3.5	-	2.5	715	478	0.67	LTB
2	I-690-2	NC	C	UM	4.4	0.75	1.825	2.0	715	659	0.92	FLB
3	I-690-3	NC	C	UM	6.0	3.0	1.5	2.5	715	509	0.71	LTB
4	I-890-1	NC	C	MG	7.0	3.5	-	2.0	862	572	0.66	LTB
5	I-890-2	NC	C	UM	4.4	0.75	1.825	2.0	862	844	0.98	FLB
6	I-890-3	NC	C	UM	6.0	3.0	1.5	1.5	862	634	0.74	LTB
7	I-890-4	NC	C	UM	6.0	3.0	1.5	2.0	701	330	0.47	LTB
8	I-890-5	NC	C	UM	6.0	3.0	1.5	1.75	448	259	0.58	LTB

Note: * Section slenderness classified based on the actual material properties, C = compact, NC = non-compact, M_p = plastic moment, M_m = maximum bending moment according to the test, LTB = lateral-torsional buckling, FLB = flange local buckling.

Table 4.4: Validation of the finite element models

No.	Notation	L_o (m)	k_r	M_{ob2}/M_{ob1}	M_{b1}/M_m	M_{b2}/M_m
1	I-690-1	3.50	1.0	1.00	0.96	0.97
2	I-690-2	0.75	1.0	1.08	1.05	1.08
3	I-690-3	3.00	0.675	1.00	0.99	0.95
4	I-890-1	3.50	1.0	1.00	0.84	0.85
5	I-890-2	0.75	1.0	1.08	0.98	0.98
6	I-890-3	3.00	0.675	1.00	0.93	0.90
7	I-890-4	3.00	0.675	1.00	0.90	0.88
8	I-890-5	3.00	0.675	1.00	0.89	0.88
Average				1.02	0.94	0.94
Standard deviation				0.03	0.07	0.07

Note: M_{ob1} and M_{ob2} are elastic buckling moments of specimens obtained from FEM-1 and FEM-2 models respectively, M_{b1} and M_{b2} are the maximum flexural load carrying capacity of the specimens obtained from FEM-1 and FEM-2 models respectively.

Table 4.5: Cross-sections for parametric study

No.	H (mm)	B (mm)	t_f (mm)	t_w (mm)
1	354	160	12	8
2	354	120	12	8
3	254	120	12	8

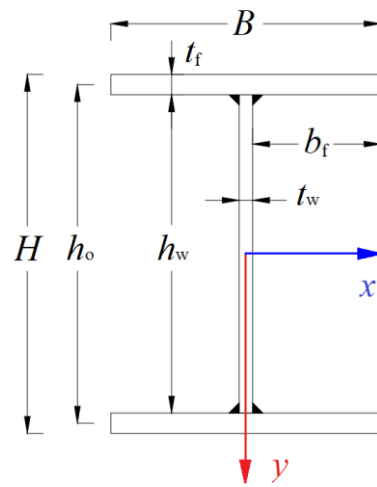


Figure 4.1: Cross-sectional dimensions of I-beams.

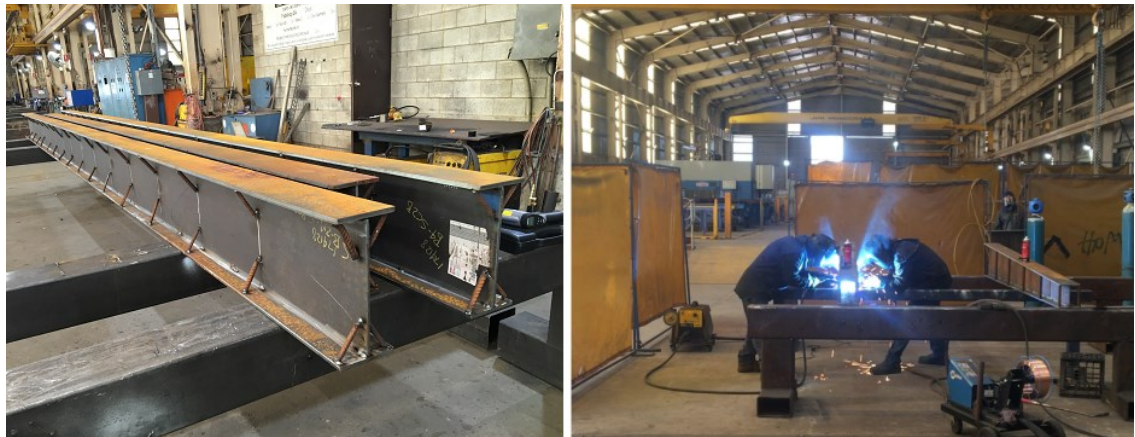


Figure 4.2: Fabrication procedure of HSS beams.



Figure 4.3: High-strength steel beam specimens.

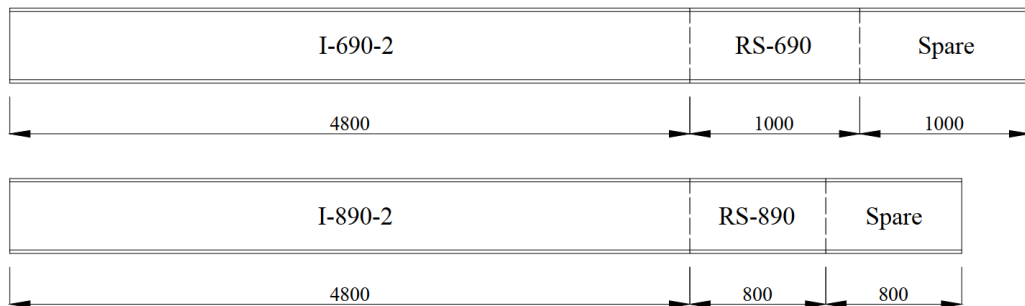


Figure 4.4: Locations of residual stress specimens RS-I-690 and RS-I-890.

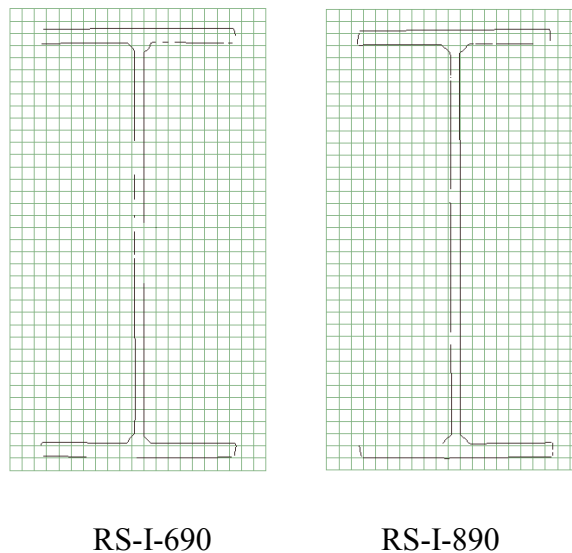


Figure 4.5: Midspan sections of residual stress specimens RS-I-690 and RS-I-890.

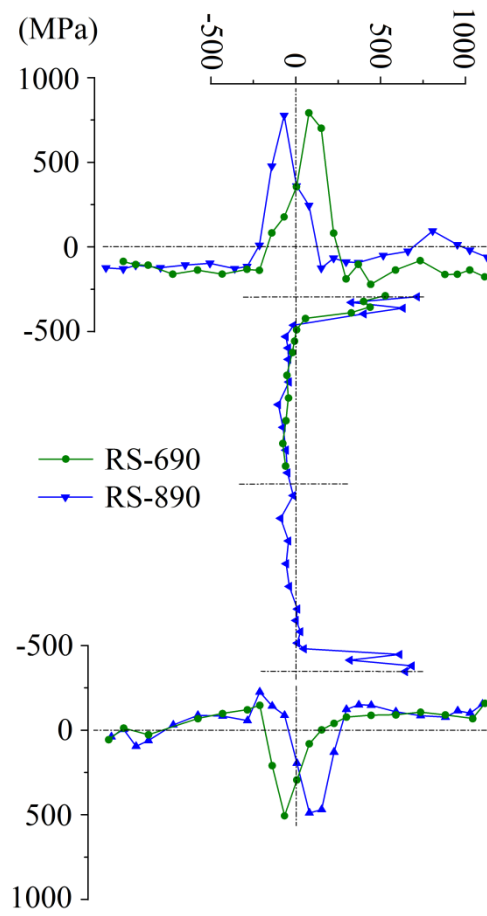


Figure 4.6: Longitudinal residual stresses in RS-I-690 vs RS-I-890.

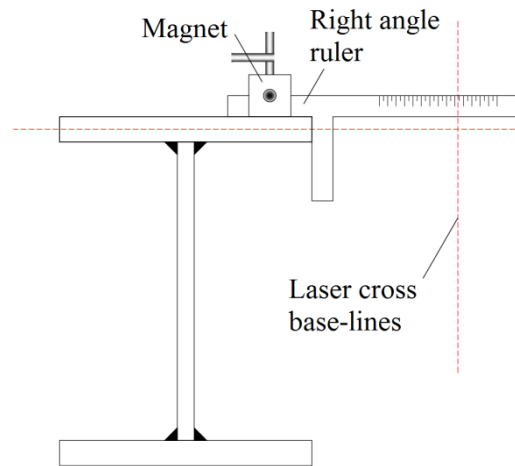


Figure 4.7: The set-up for out-of-plumbness assessment.

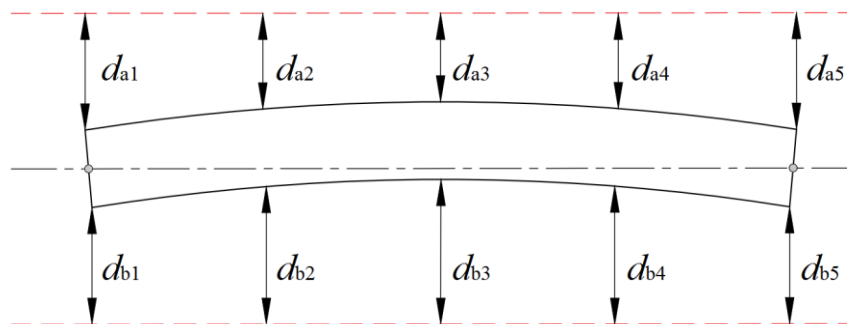
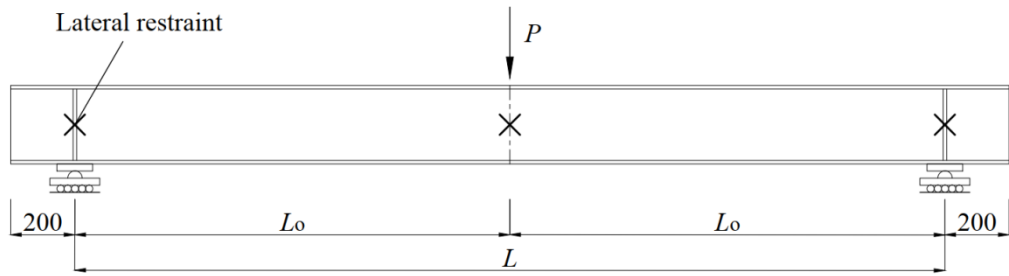
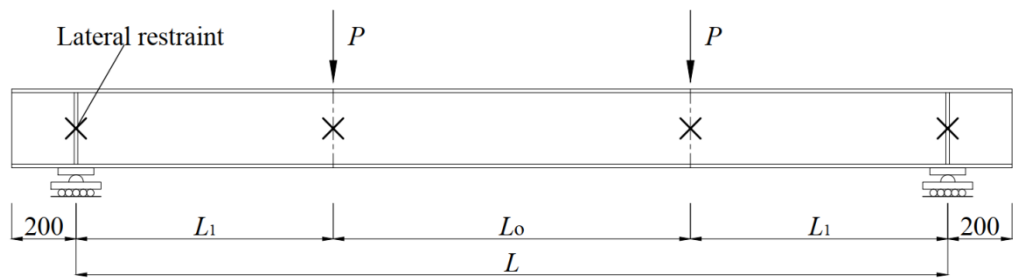


Figure 4.8: The out-of-plumbness measurement positions (Xiong *et al.*, 2016).



Three-point loading (Moment gradient $\beta = 0$)

Figure 4.9: Test arrangement for LTB of the beams under gradient bending moment.



Four-point loading (Uniform moment $\beta = -1$)

Figure 4.10: Test arrangement for the buckling of the beams under uniform bending moment.

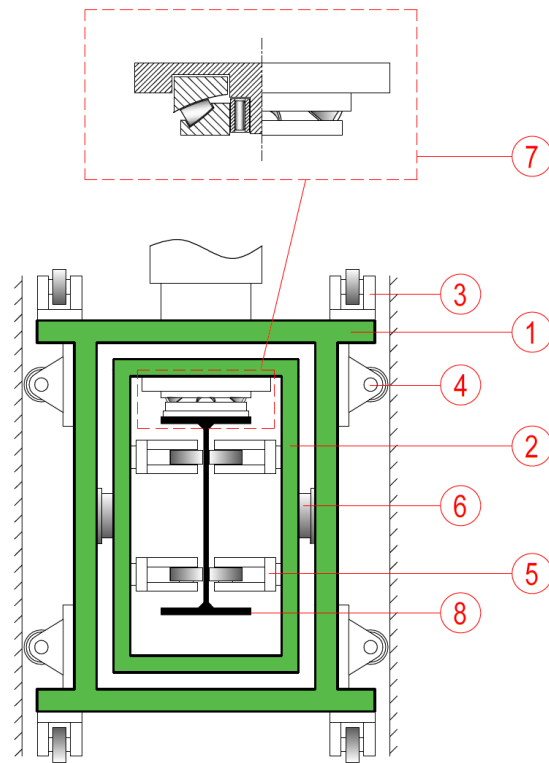


Figure 4.11: Loading box: (1) outer box, (2) inner box, (3-5) roller bearings, (6) spherical roller bearings, (7) modified spherical thrust roller bearing, and (8) I-beam specimen.



(a) The modified spherical thrust roller bearing



(b) The loading box.

Figure 4.12: The assembly of the loading box.

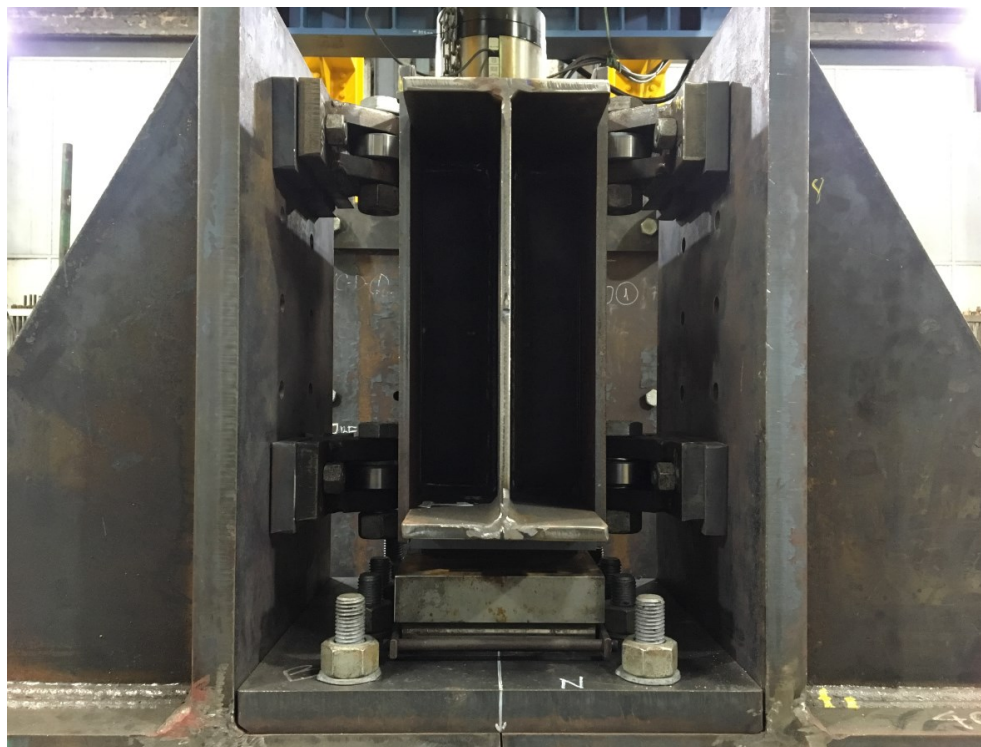
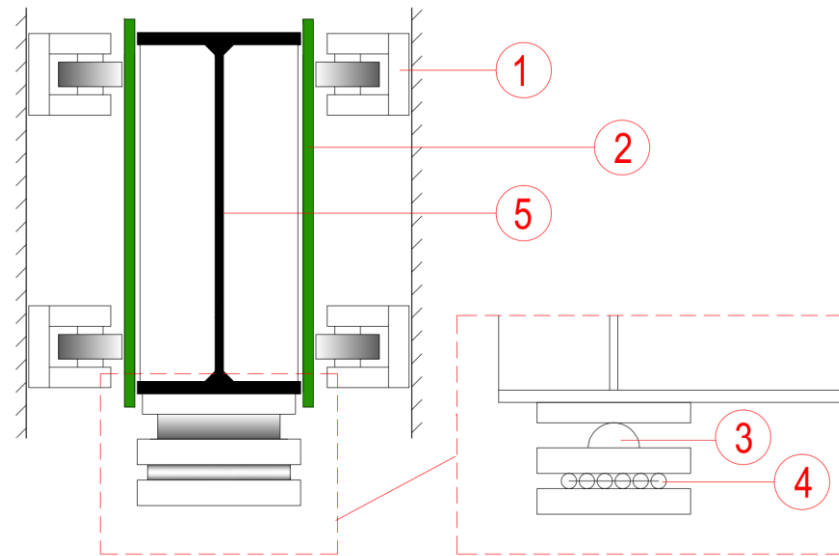
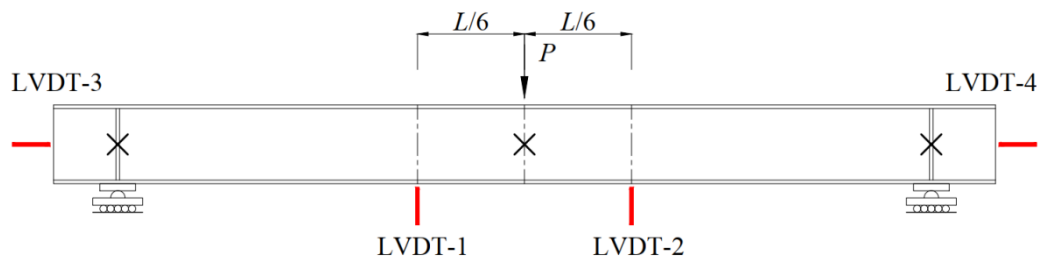
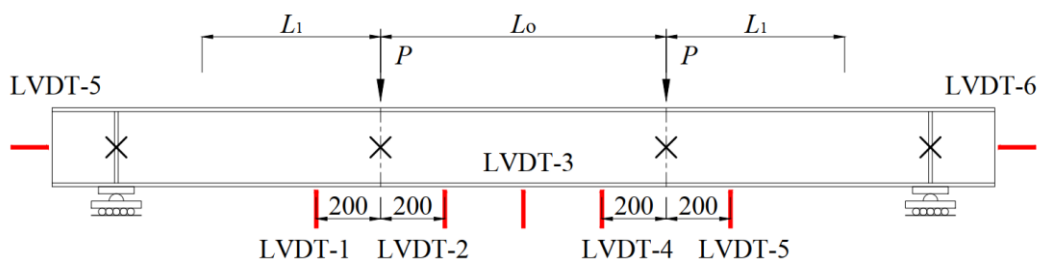


Figure 4.13: End restraint: (1) roller bearings, (2) flat plates attached to stiffeners, (3) semi-circle bar, (4) rollers, and (5) I-beam specimen.



(a) 3-point loading (Moment gradient $\beta = 0$)



(b) 4-point loading (Uniform moment $\beta = -1$)

Figure 4.14: LVDT layouts.

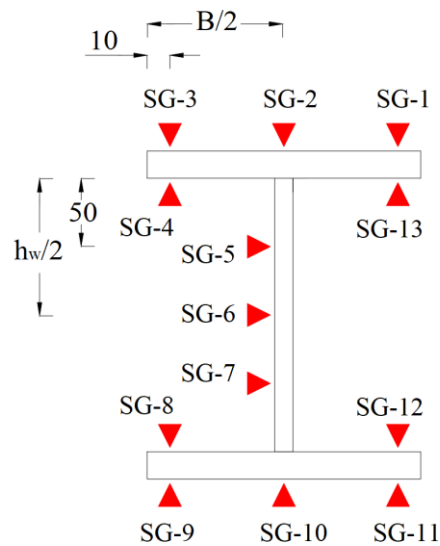
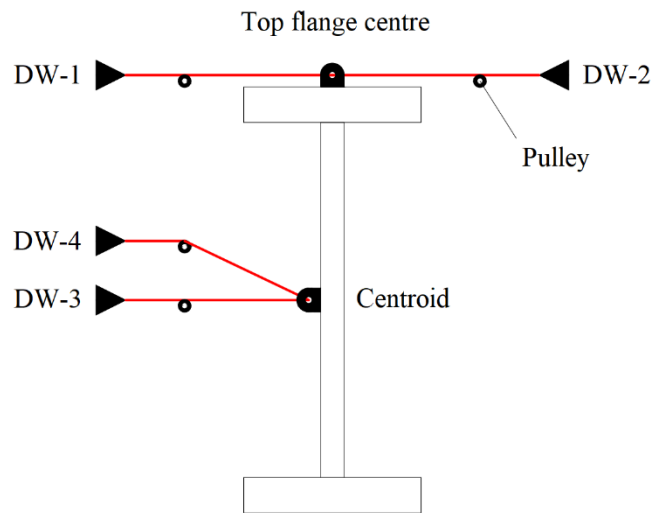


Figure 4.15: Strain gauge layout.

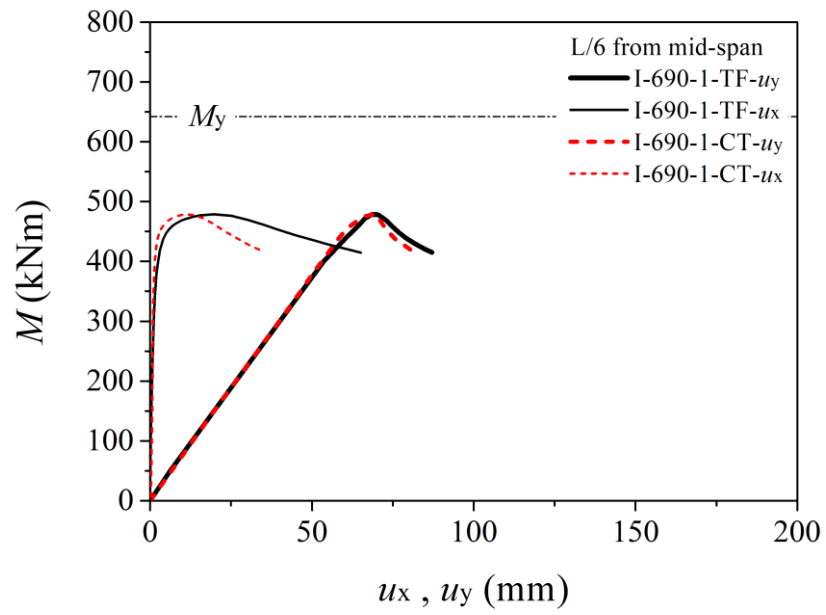


(a) Layout of draw-wire transducers set-up at initial undeformed position of the beam.

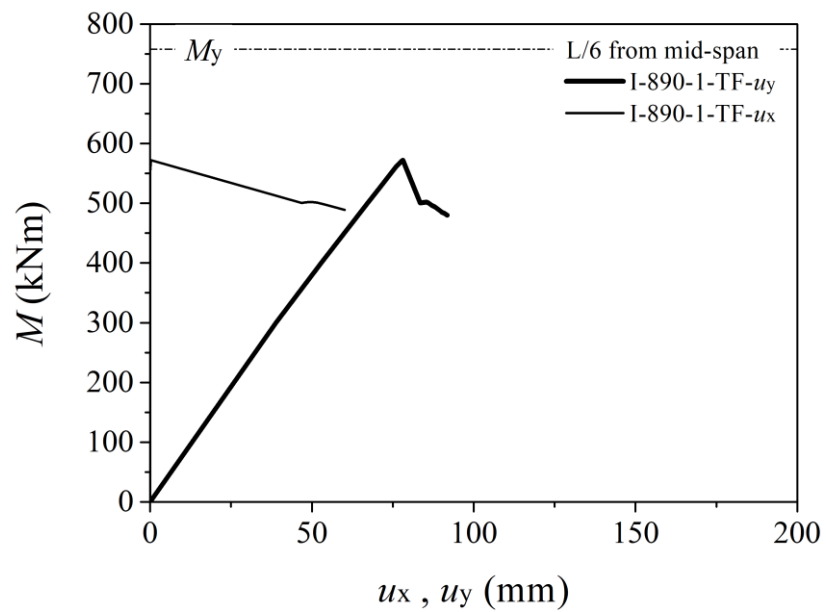


(b) Draw-wire transducers tracking the movement of the beam centroid and top-flange centre.

Figure 4.16: Draw-wire transducer arrangement.



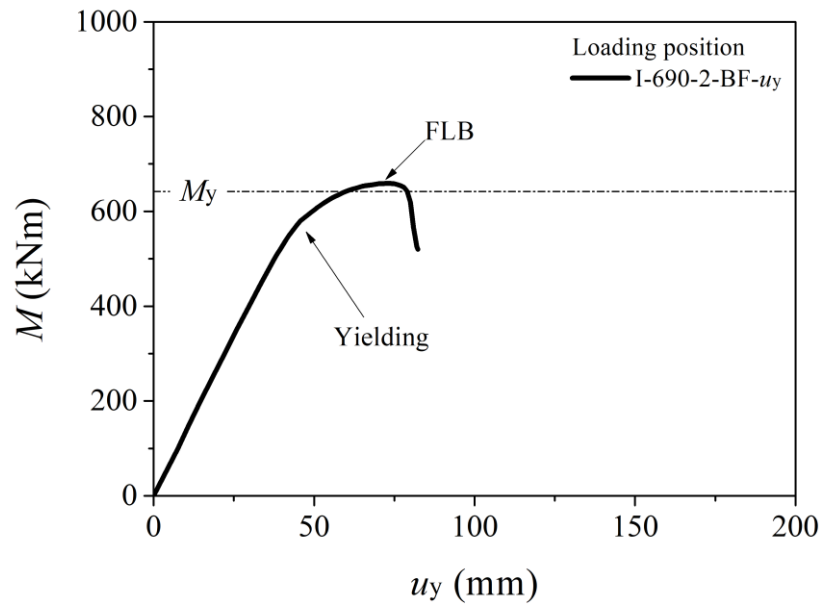
(a)



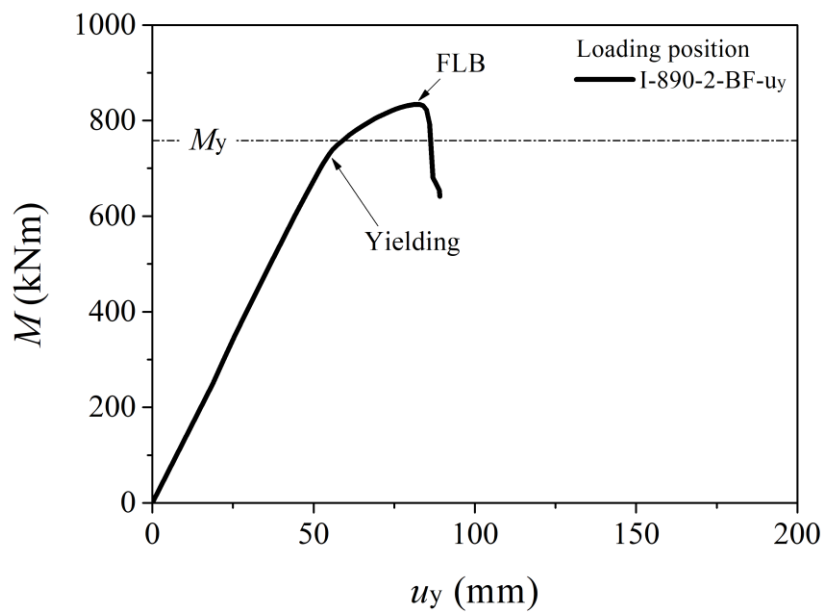
(b)

Figure 4.17: Load-displacement evolutions of I-beam specimens

(TF = top flange centre, BF = bottom flange centre, CT = centroid, u_x = displacement in x direction, u_y = displacement in y direction).

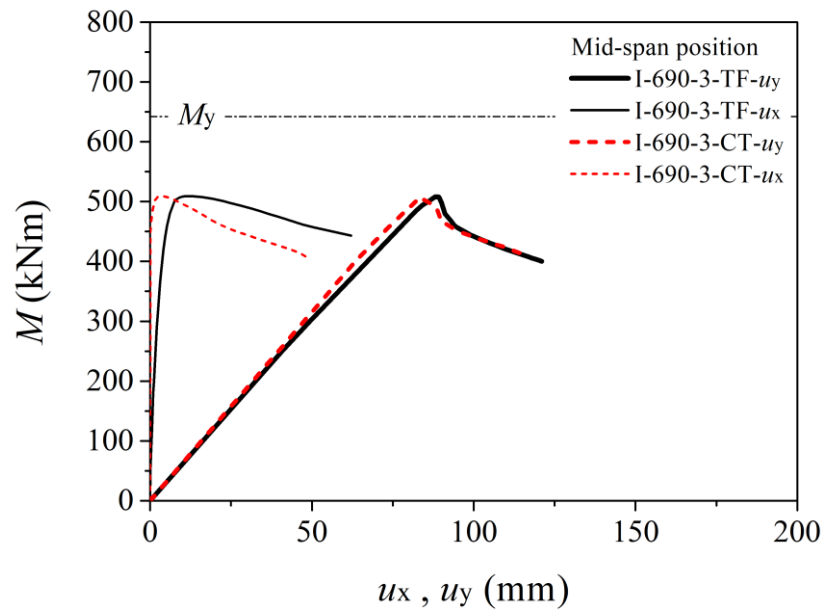


(c)

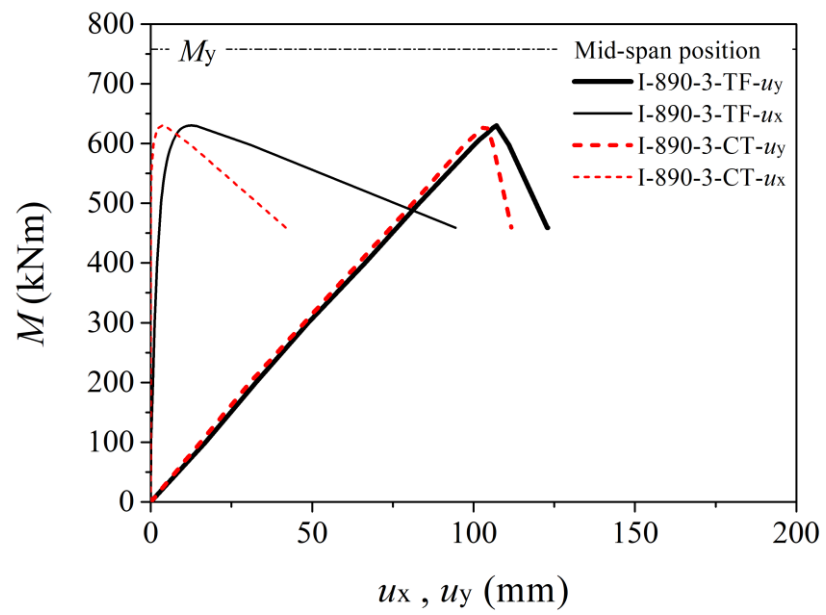


(d)

Figure 4.17 (cont.)

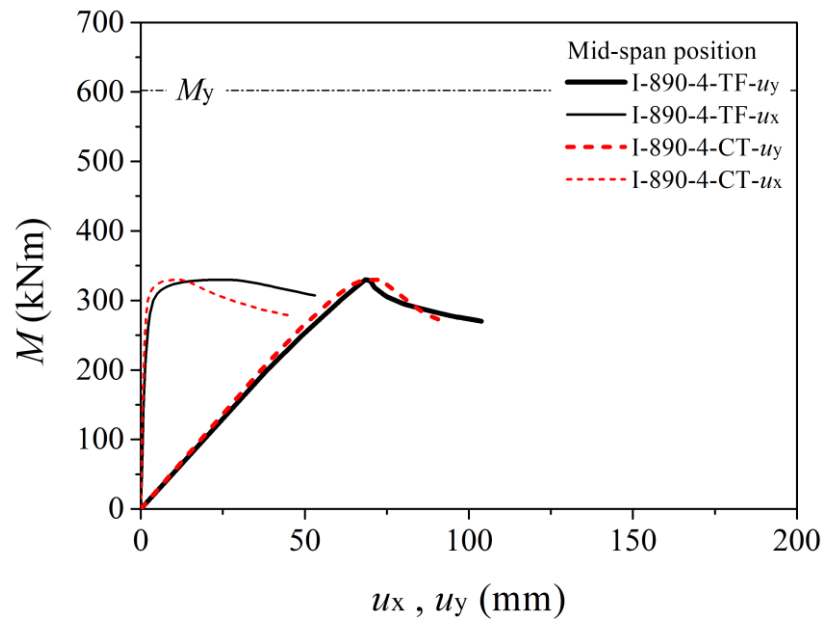


(e)

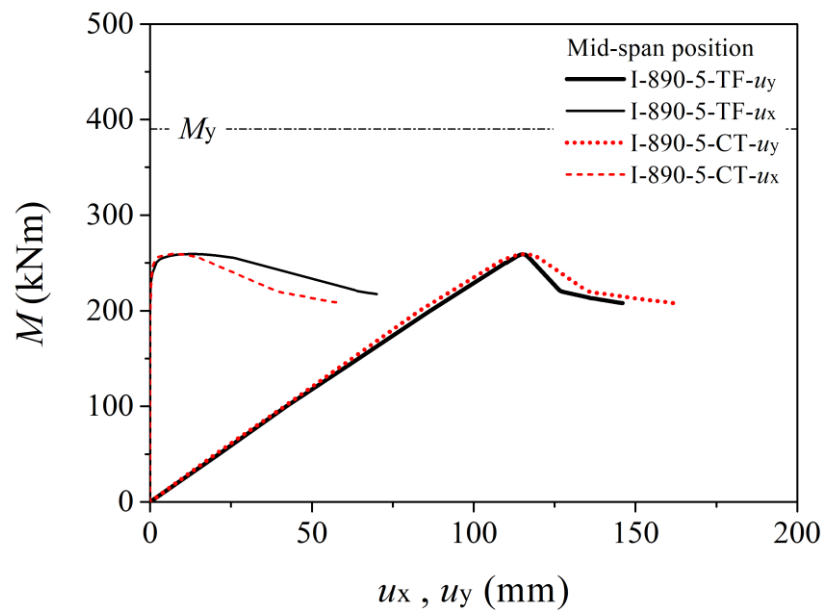


(f)

Figure 4.17 (cont.)

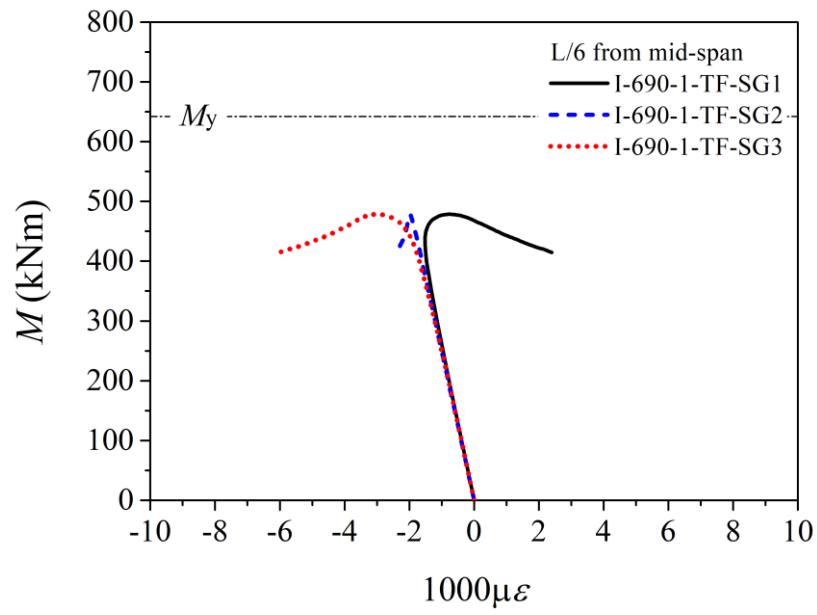


(g)

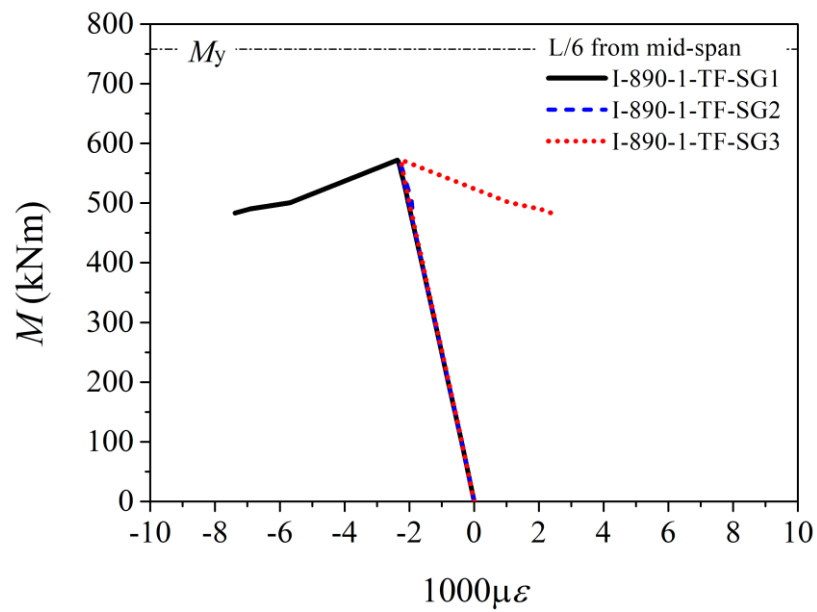


(h)

Figure 4.17 (cont.)

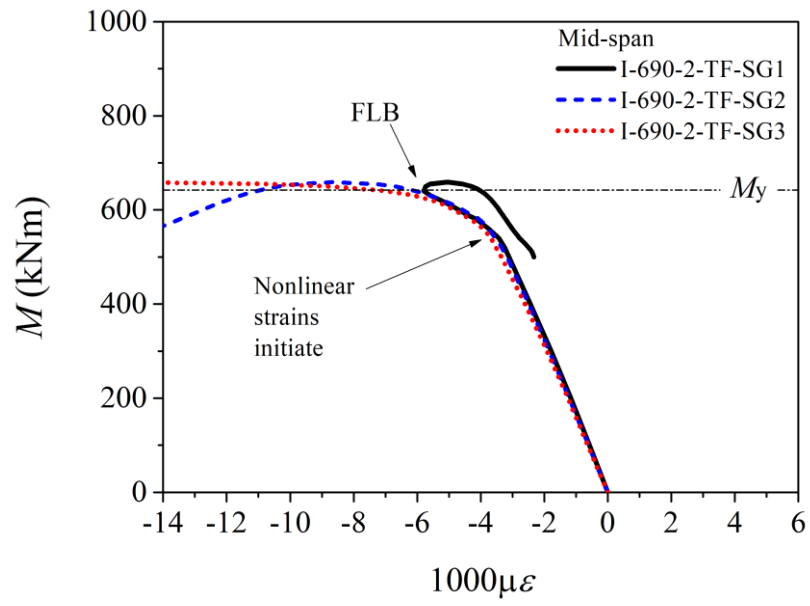


(a)

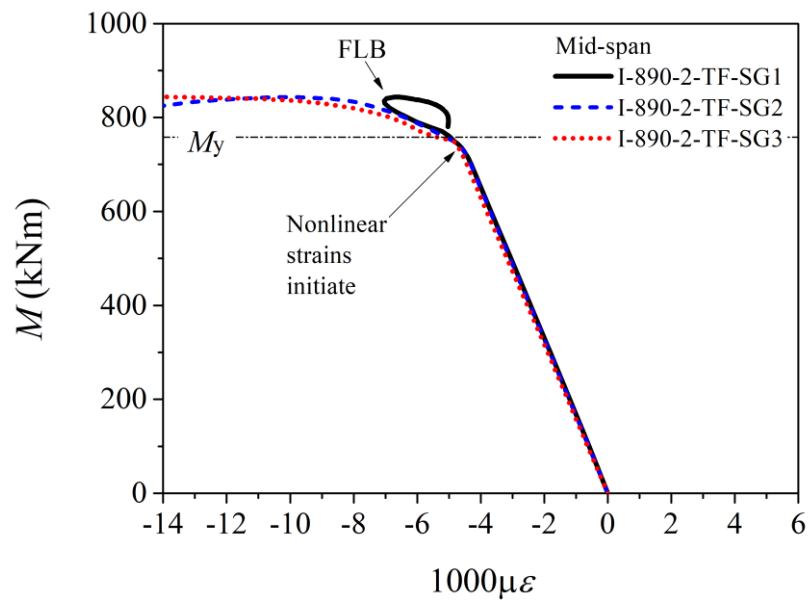


(b)

Figure 4.18: Longitudinal strain development in compression flanges.

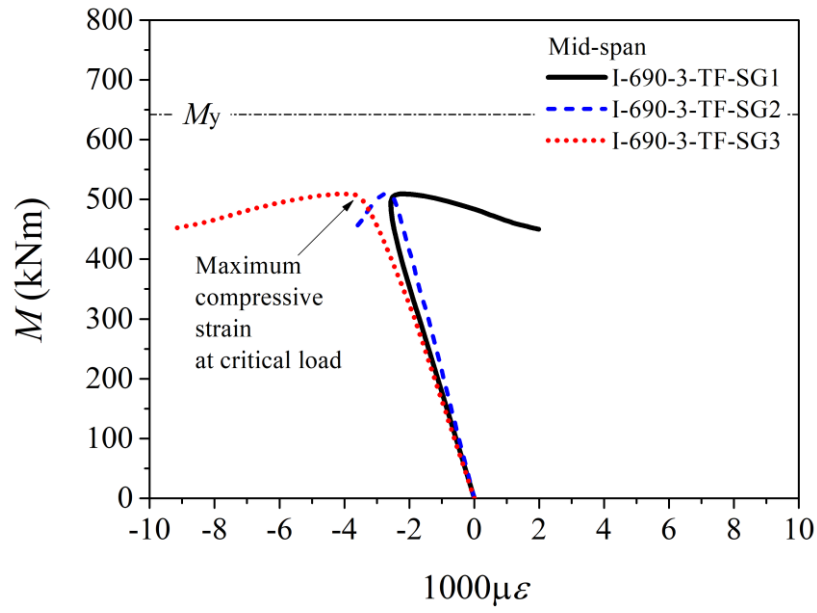


(c)

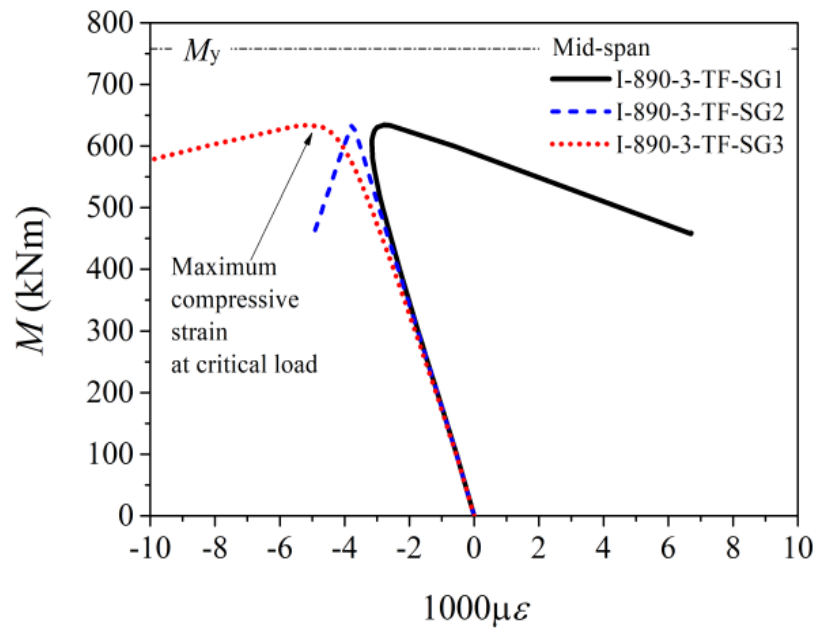


(d)

Figure 4.18 (cont.)

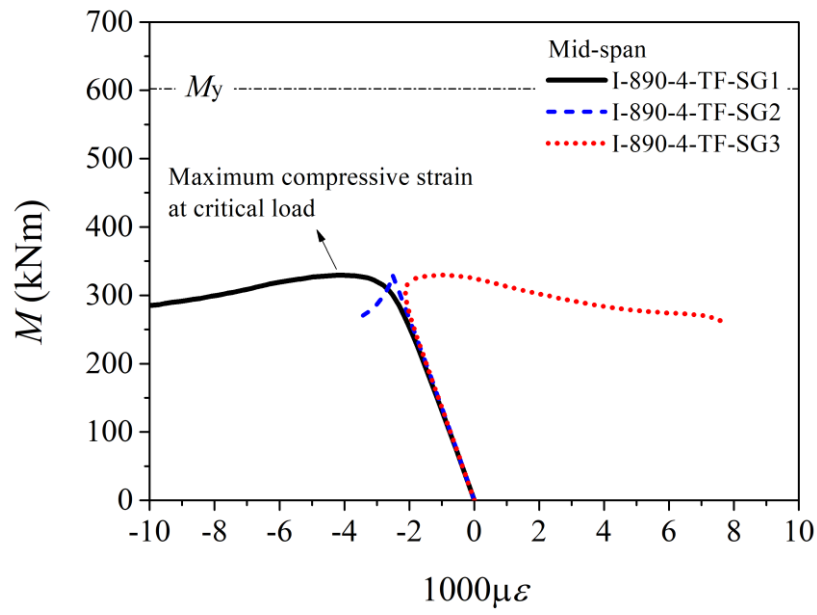


(e)

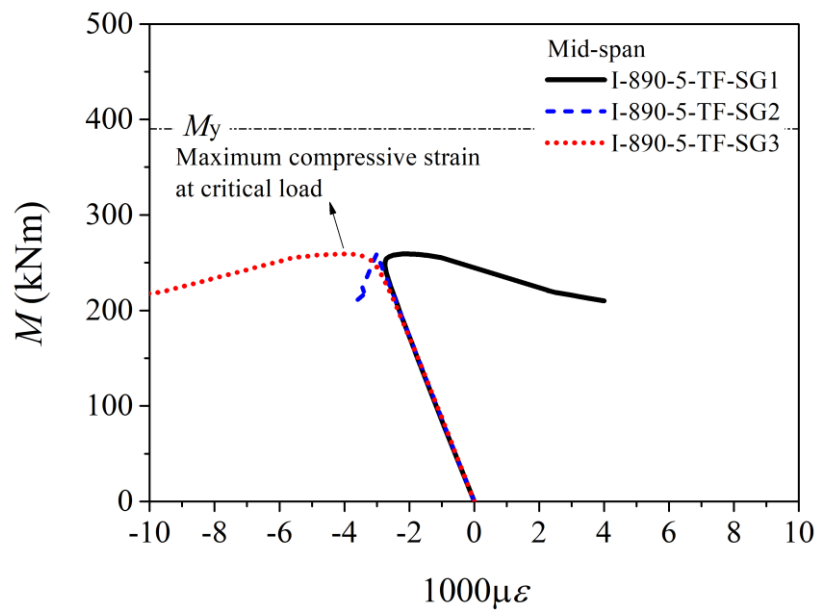


(f)

Figure 4.18 (cont.)



(g)

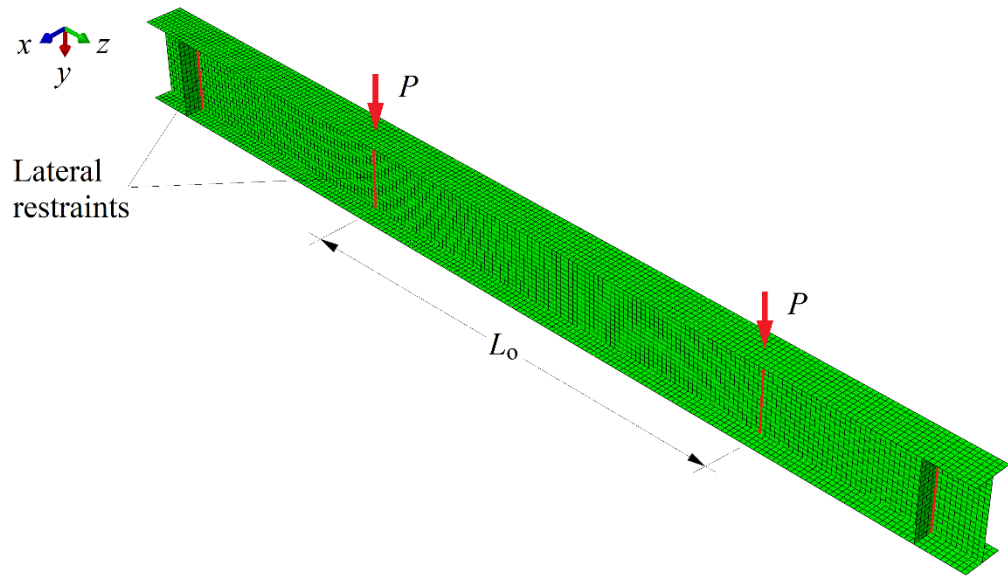


(h)

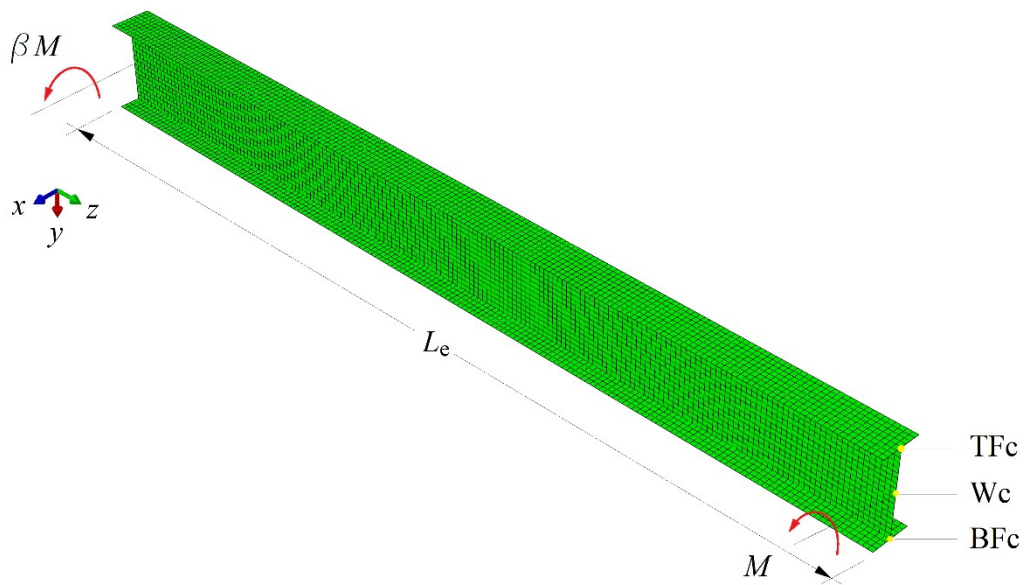
Figure 4.18 (cont.)



Figure 4.19: Buckling modes: (a) LTB of an I-beam under UM, (b) LTB of an I-beam under MG, and (c) FLB of an I-beam under UM.



(a) Test simulation model (FEM-1)



(b) Generic model (FEM-2)

Figure 4.20: Finite element models of HSS beams.

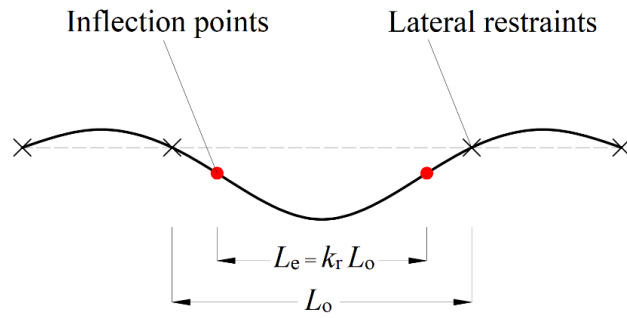


Figure 4.21: Effective length of tested span.

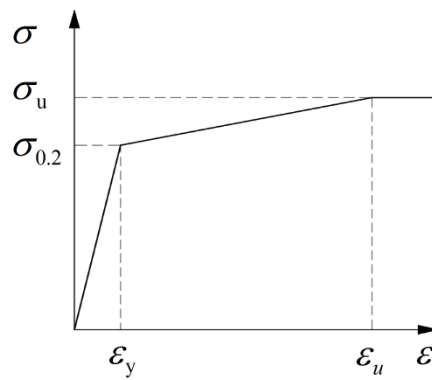
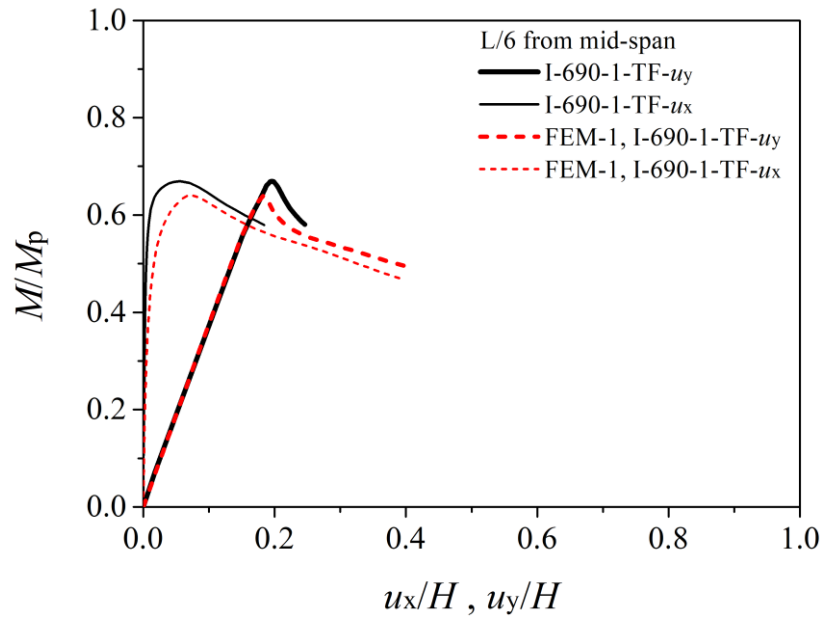
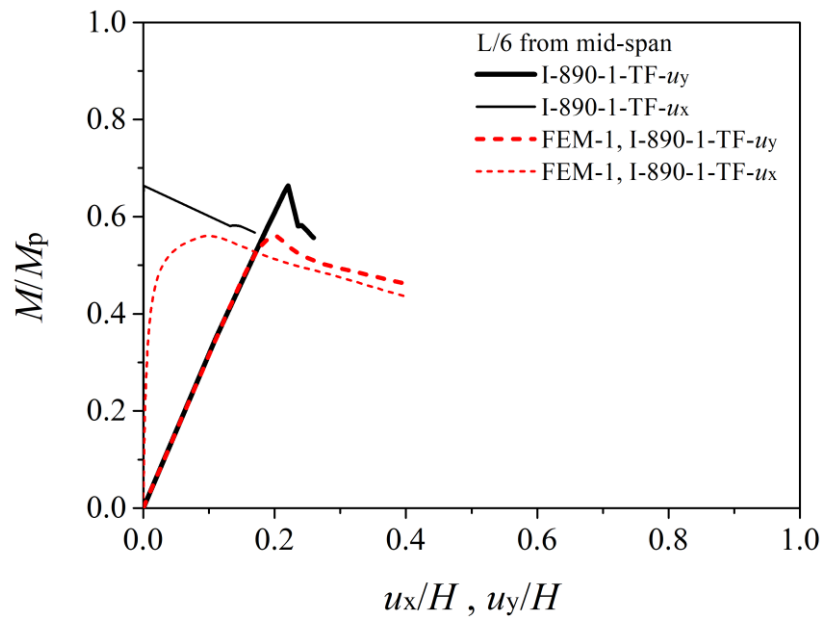


Figure 4.22: Stress-strain multi-linear relation model.

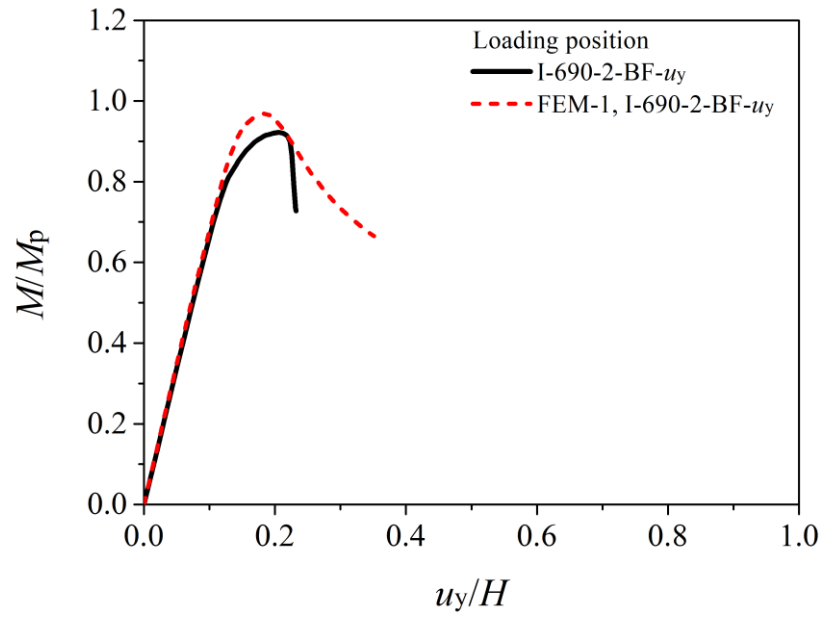


(a)

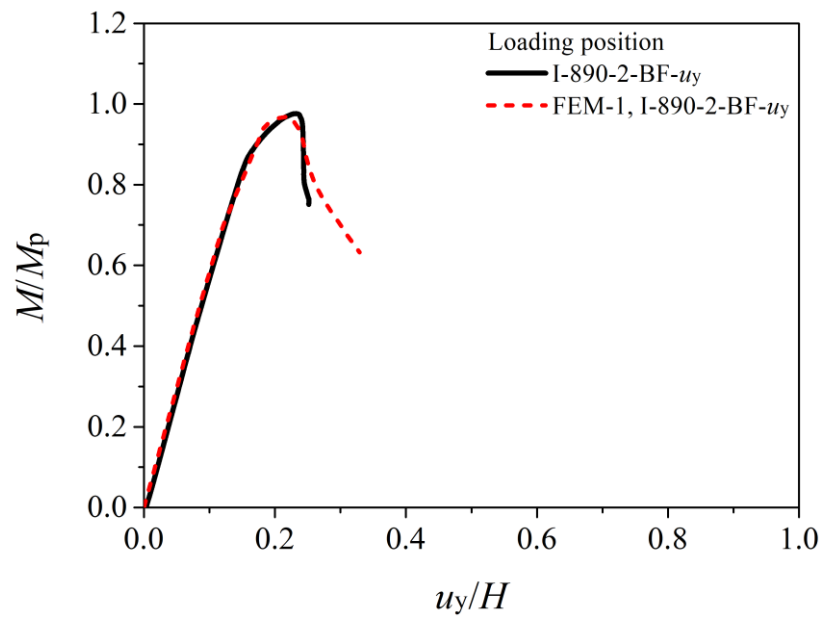


(b)

Figure 4.23: Normalised load-displacement relations.

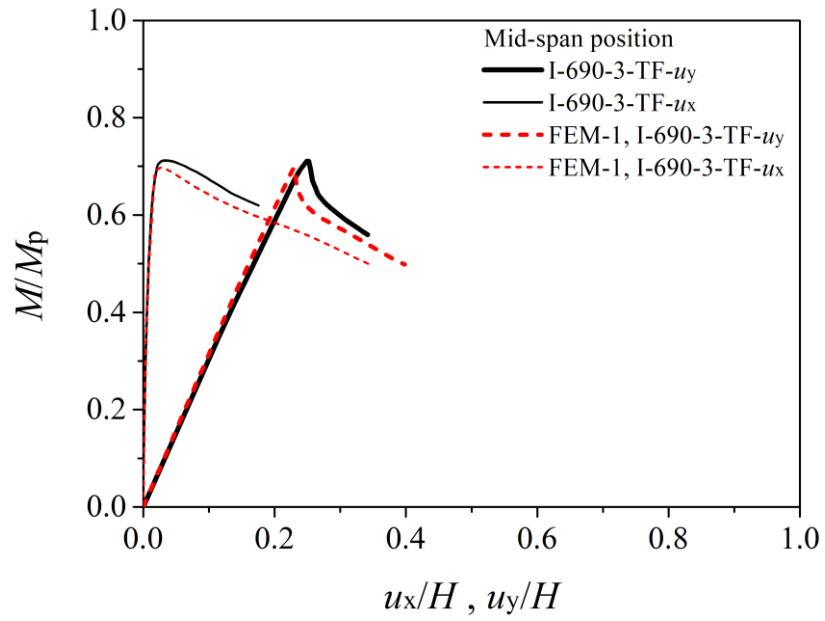


(c)

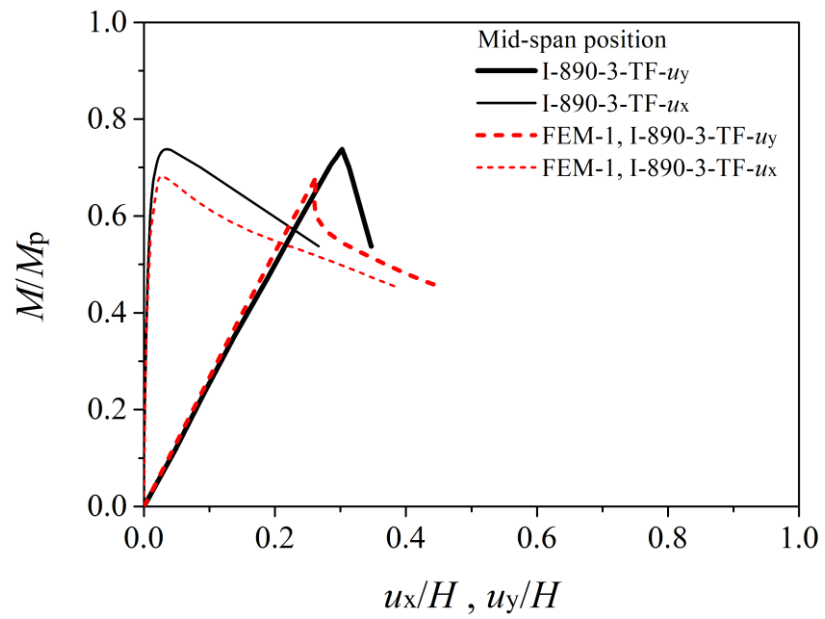


(d)

Figure 4.23 (cont.)

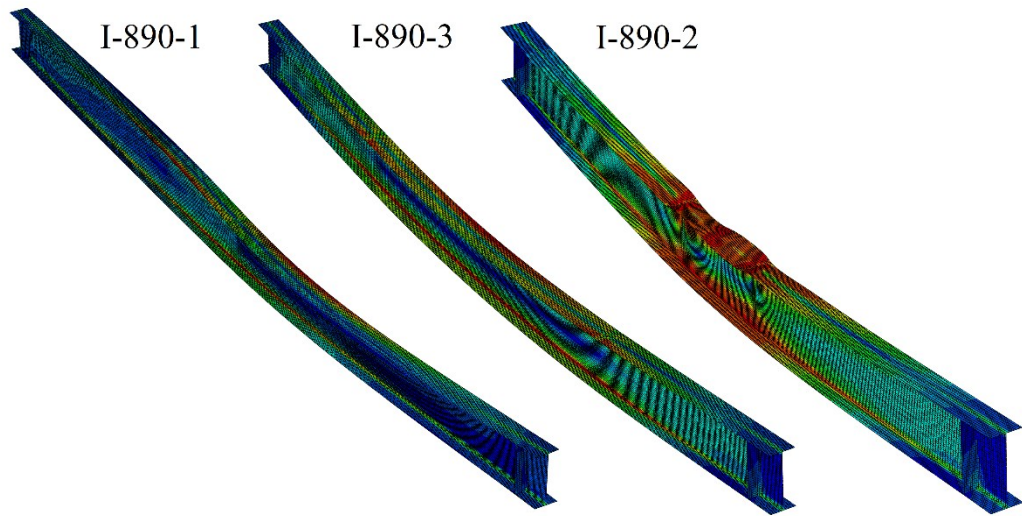


(e)

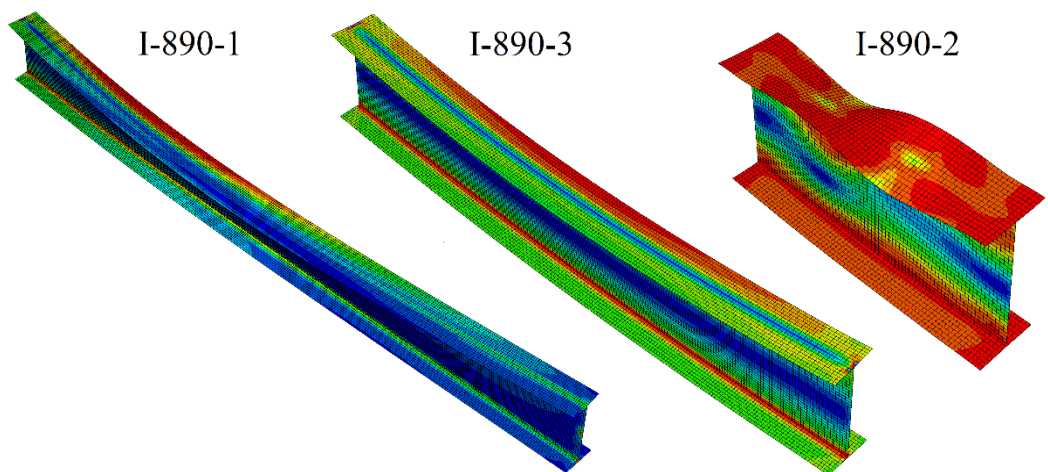


(f)

Figure 4.23 (cont.)



(a) Test simulation model (FEM-1)



(b) Generic model (FEM-2)

Figure 4.24: Deformation of the I-beam specimens at critical buckling load.

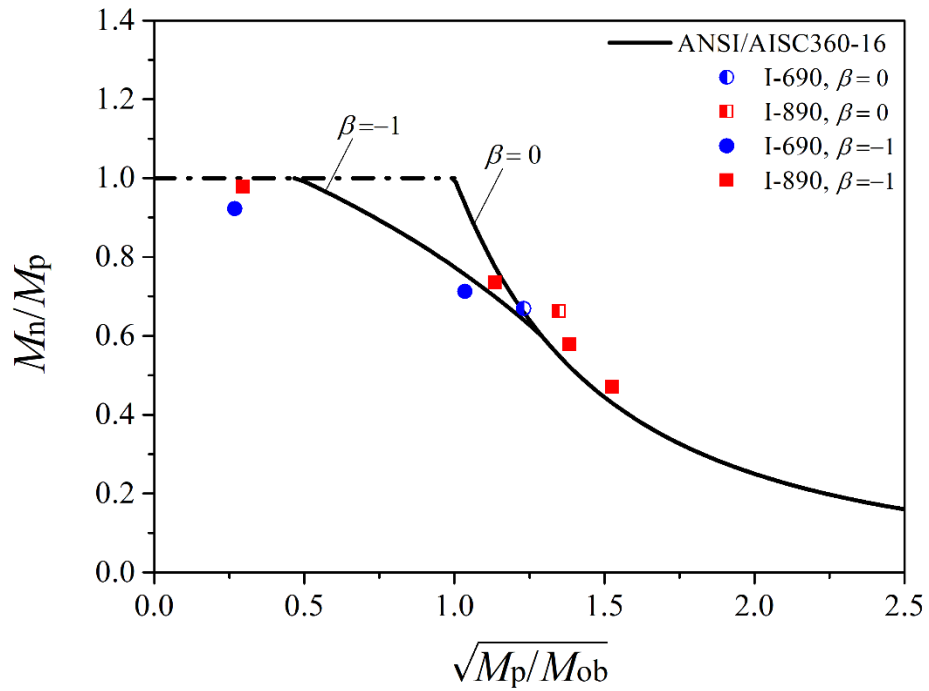


Figure 4.25: Comparison between test results and ANSI/AISC360-16 model.

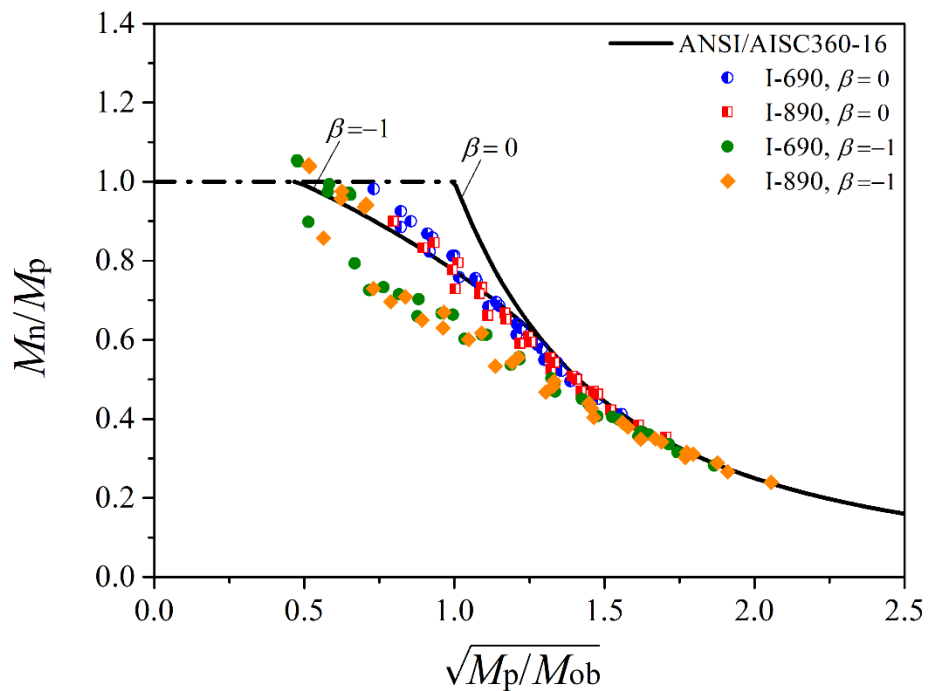


Figure 4.26: Comparison between the generic FE predictions and ANSI/AISC360-16 model.

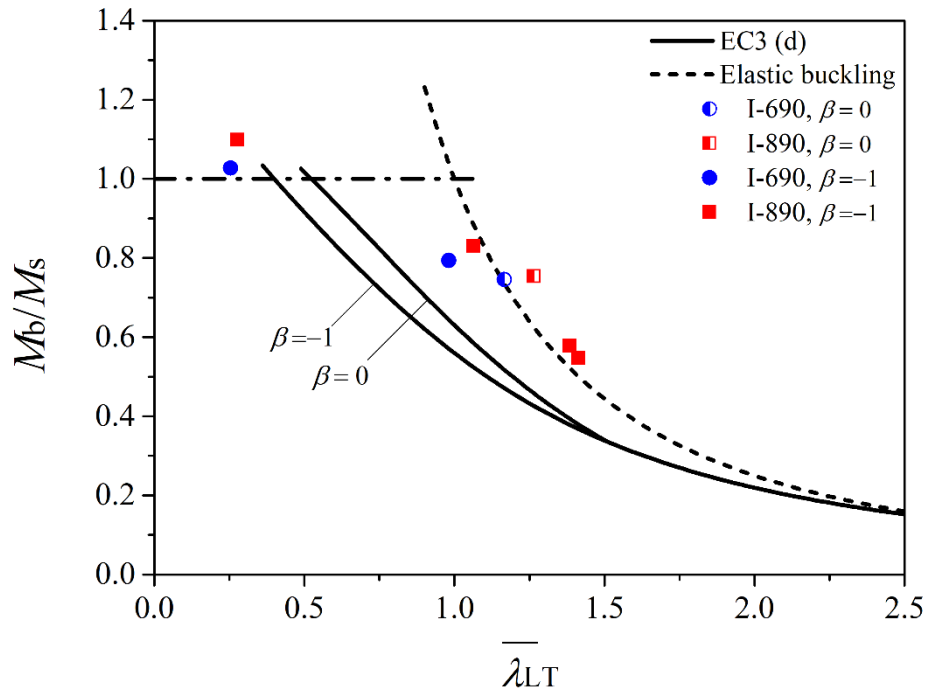


Figure 4.27: Comparison between test results and EC3 limited method.

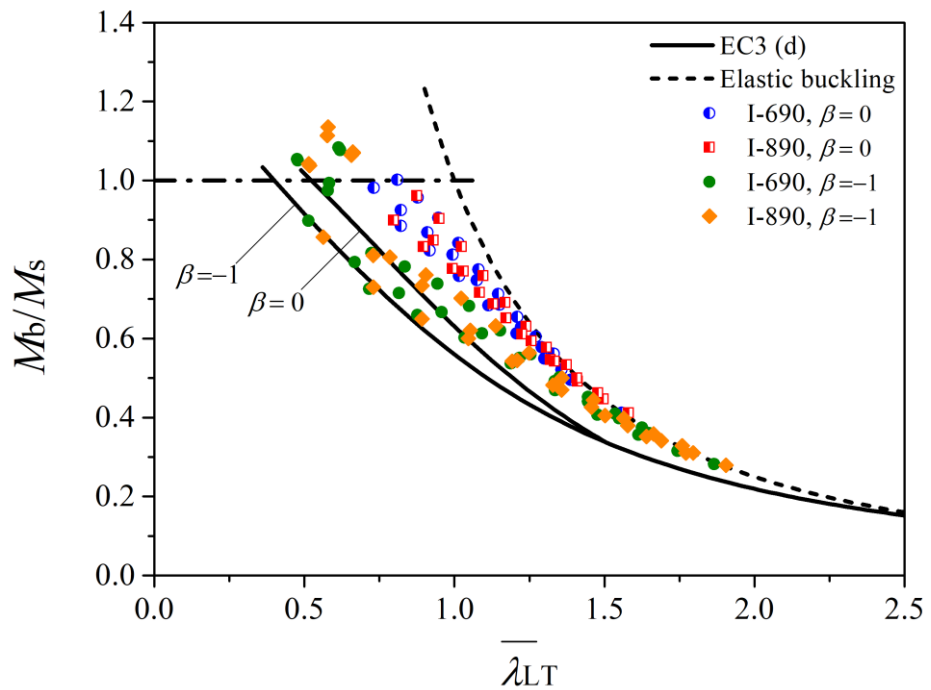


Figure 4.28: Comparison between the generic FE predictions and EC3 limited method.

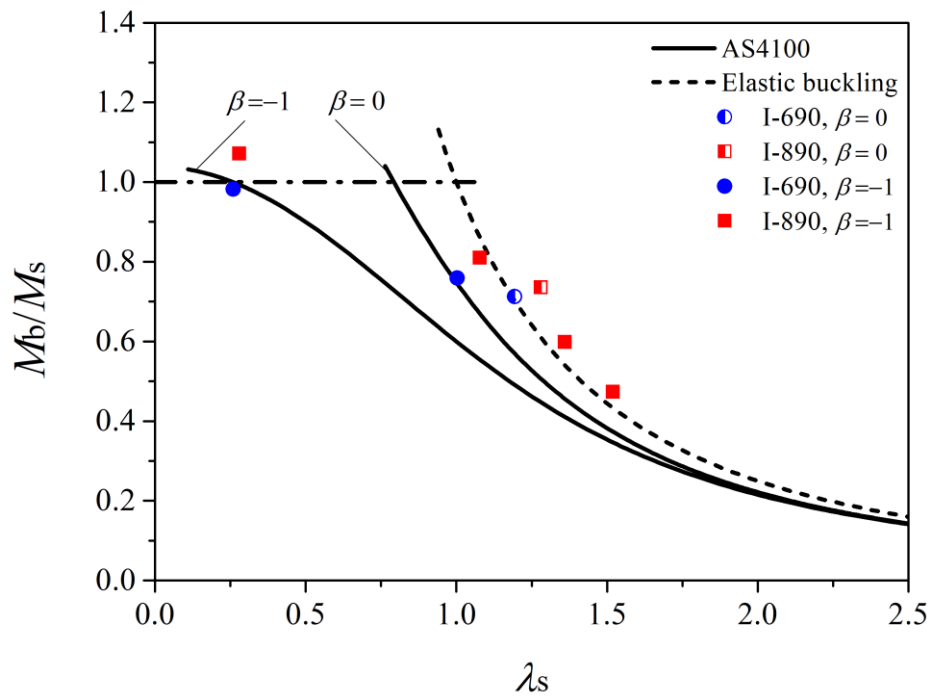


Figure 4.29: Comparison between test results and AS4100.

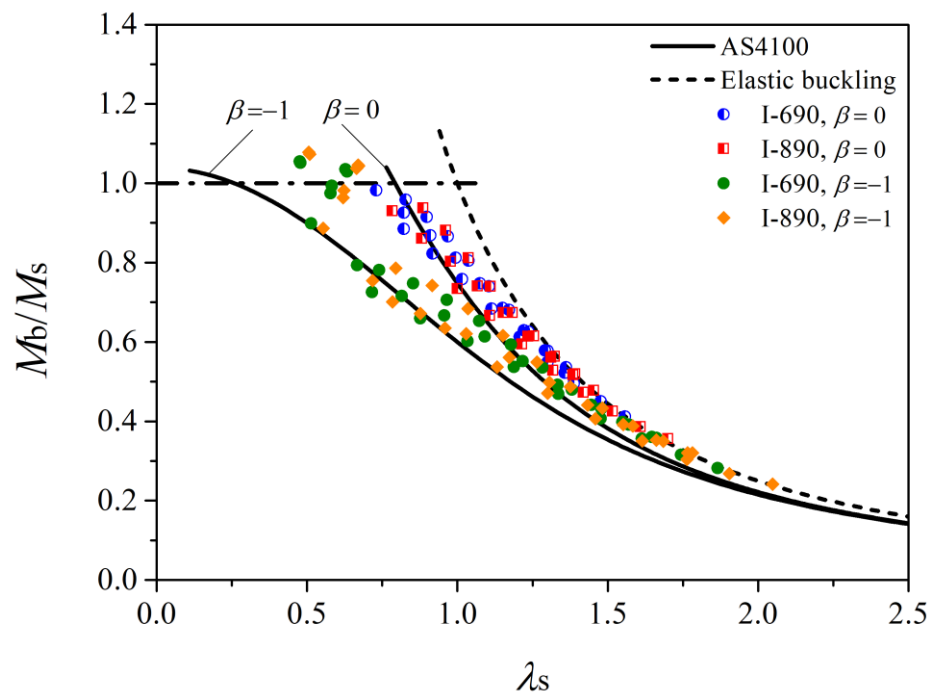


Figure 4.30: Comparison between the generic FE predictions and AS4100.

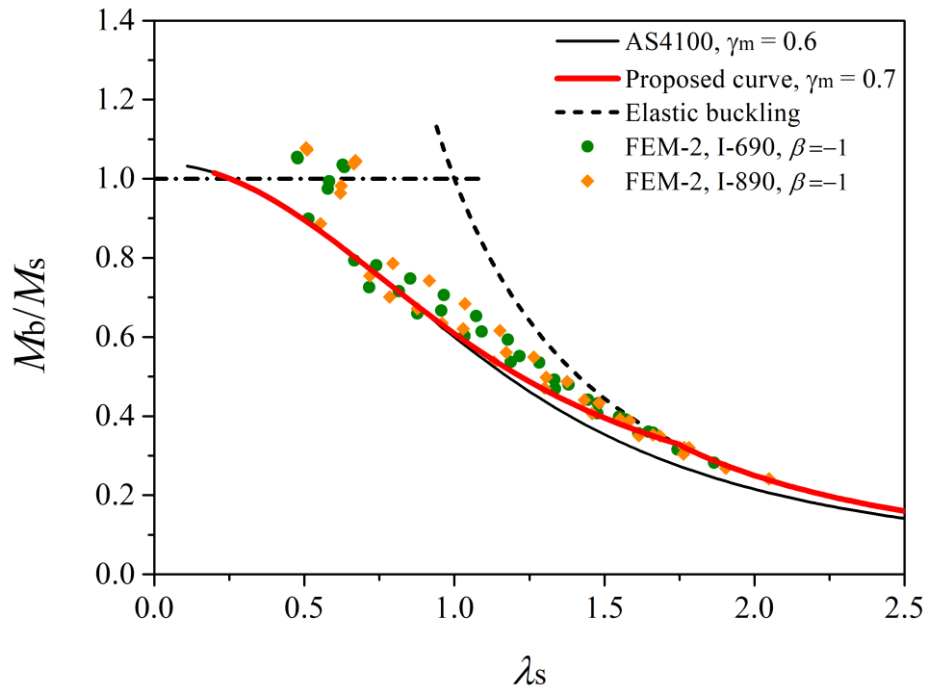


Figure 4.31: New LTB curve for the AS4100 in the case of uniform bending moment.

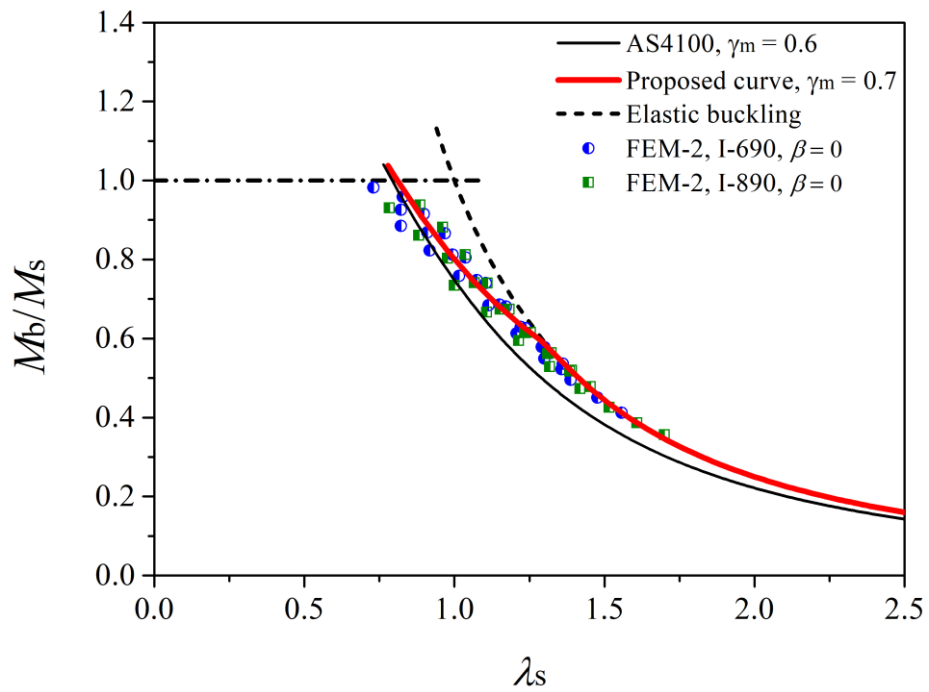


Figure 4.32: New LTB curve for the AS4100 in the case of moment gradient.

CHAPTER 5 BUCKLING OF WELDED WEB-TAPERED HIGH-STRENGTH STEEL I-BEAMS

5.1. Introduction

Structural members with non-prismatic sections are commonly used in steel construction to optimise the use of materials with respect to the nonuniform distribution of the force resultants along the structural members. Such design not only fully exploits the section capacity of the member, but it is also economic in the sense of enabling aesthetic and lightweight structures and saving resources, i.e. materials and erection costs. However, it is known that steel structural components are typically slender, and their strength is normally governed by their stability. Therefore, the structural stability of non-prismatic steel members and frames having such tapered components have been the subject of several studies. Unfortunately, very few studies on the behaviour of non-uniform cross-section members fabricated from HSS can be found in the literature, and no experimental investigation on the stability of non-prismatic members made of HSS has been reported.

In this chapter, experimental and numerical studies on the global buckling behaviour of web-tapered I-section beams fabricated from Australian BISPLATE-100 HSS plates with the normal yield stress $f_y = 890$ MPa are presented. The specimens consisted of three beams tested in a uniform moment loading condition and one beam tested in a moment gradient condition. All four specimens were designed to develop a lateral-torsional buckling mode. Based on the test results, a numerical study was conducted, in

which a three-dimensional ABAQUS (2014) finite element (FE) model has been constructed and parametric studies have been carried out. The national standard provisions in EC3 (2005) and AS4100-1998 (2016) are reviewed for web-tapered HSS I-beams with respect to the experimental results and extended data from the FE simulations.

5.2. Experimental program

5.2.1. Specimen preparation

Four full-scale web-tapered I-beams were fabricated from BISPLATE-100 HSS plates having a nominal yield strength of $f_y = 890$ MPa. Nominal 12 mm and 8 mm thick plates were used for the flanges and the webs respectively. The geometry of the specimens is outlined in Figure 5.1 and the actual dimensions of the specimens are given in Table 5.1. The taper constant $\alpha_w = h_{o2}/h_{o1}$ (smallest depth/largest depth) varies from 0.5 to 0.7 and the variation of flange slenderness ($\lambda_f = b_f/t_f$) and web slenderness ($\lambda_w = h_w/t_w$) is also provided in Table 5.1.

Specimen TB-890-2 is shown specifically in Figure 5.2. The specimens were designed such that the web-tapered middle segment was the tested span, while the prismatic end-segments were used as lever arm to generate and apply external bending moments at the two ends of the middle segment. Furthermore, the estimated buckling resistance of the tapered part of the specimen was considerably lower than the flexural strength of the small prismatic end-segment so that the failure of the specimens was governed by the instability of the middle tapered segment.

The BISPLATE-100 parent plates were flame-cut and welded together following the AS/NZS1554.4 (2010) guidelines. Gas metal arc welding with the specifications given

in Table 3.3 was employed. Before the welding, the flange components had been bent to the designed angle at the intersection position of the tapered and prismatic segments. The flange and web were then aligned and preassembled by tack welds and steel rods. The weld regions were preheated to about 150 °C prior to the welding which was simultaneously applied on opposite sides at the flange and web junction in order to reduce the distortion caused by the unbalance of heat transfer. Transverse stiffeners were only provided at the beam supports which were 200 mm away from the beam ends. The weld filler material has a nominal yield stress of 660 MPa and tensile stress of 760 MPa according to the relevant specification (AWS A5.28/A5.28M:2005, 2015). The welding of all specimens was examined using a magnetic particle inspection (MPI) process with no rejectable surface discontinuities being detected.

5.2.2. Material properties

The tensile test samples were cut directly from the virgin BISPLATE-100 plates using laser cutting along the rolled directions with the material characteristics presented in Section 3.3.2. The typical stress-strain curves of BISPLATE-100 coupons are shown in Figure 3.10 and the mechanical properties given in Table 3.2.

5.2.3. Residual stresses

A web-tapered beam (RS-TB-890) as illustrated in Figure 3.5 was prepared for determining the characteristics of the residual stress distribution in the BISPLATE-100 tapered sections using the neutron diffraction method. Details of the measurement method and the residual stress patterns in welded HSS I-sections are presented in Chapter 3. The fabrication procedure for the residual stress specimen was similar to that of the buckling test samples without the prismatic segments.

As indicated in Figure 3.5, three cross-sections along the axial direction of the beam were investigated for their residual stress distributions. The residual stresses induced in the top-flange of the smallest section RS-TB-890-1 and in the web of all three sections were measured and the longitudinal stresses are shown in Figure 5.3. It is seen that the tensile residual stress peaked in the heat-affected zone (HAZ), i.e. the flange-web intersections, whilst the compressive residual stress was approximately uniform outside the HAZ. Also, the magnitude of the compressive stresses in the web increases relatively along the taper direction. The residual stress patterns in the cross-sections investigated can be represented by the idealised model shown in Figure 3.23 with the average magnitude of the tensile and compressive residual stresses in the flange and web summarised in Table 5.2.

5.2.4. Geometric imperfections

The out-of-plumb imperfection of the tapered beams was measured using the set-up described in Section 4.2.4 which was adapted from Xiong et al. (2016). The magnitudes of the out-of-plumb imperfections $D_{i,max}$ are given in Table 5.3 for all specimens. The measured imperfections were between 2.0 and 2.5 mm, which were smaller than the limit of 1/1000 of the span length or 3 mm imposed by the AS4100-1998 (2016).

5.2.5. Buckling test set-up

The test arrangement for lateral-torsional buckling of the tapered beams is illustrated in Figure 5.4, in which transverse loading was applied at the prismatic-taper intersections to generate external bending moments at the two ends of the middle tapered segment. Two loading scenarios with a uniform bending moment condition ($\alpha_L = 1, \beta = -1$) and a

moment gradient condition ($\alpha_L = 0, \beta = -1/3$) were considered. Details of the loading parameters are given in Table 5.3.

The loading and restraint system was developed with respect to the studies of Dux and Kitipornchai (1983) and Xiong et al. (2016). The hydraulic actuators applied the load onto the beam through special loading boxes that allowed free rotation of the beam about the major and minor axes, and which also allowed free warping and downward movement of the beam but restrained the beam against lateral deflection and twist. A picture of loading box is shown in Figure 5.5. Because the loading boxes were hung on the top flange of the beam at the prismatic-taper intersections, a layer of high compressive strength plaster with a nominal compressive strength of 100 MPa was firstly applied beneath the steel loading plate to support and align it in the horizontal plane. After the plaster cured, the boxes were then placed on the steel plate. The movements of the boxes were guided by a set of two universal columns which were assembled into a frame system and firmly braced as shown in Figure 5.5. In order to minimise friction, rollers were utilised at contact positions between the components. The end-support shown in Figure 5.6 is similar to the support of uniform beams so that the beam end twist and lateral deflection were prevented but warping and rotation about the major and minor axes, as well as movement in the axial direction, were allowed.

The 500 kN hydraulic actuators were set to run first in a force-controlled and subsequently in a displacement-controlled mode. The force-control stage of the loading was operated at a rate of 3 kN/min until reaching 80% of the estimated critical load, followed by the displacement control at a rate of 0.3 mm/min until buckling. The unloading rate was 2 mm/min. To ensure that the set-up functioned correctly, prior to the actual test, the specimens were loaded up to 20% of the estimated critical load.

It should be noted that when two actuators were running at the same movement rate under the displacement control, transverse loads were generated with different magnitudes due to the variation of the beam stiffness in the axial direction. Because of this, in the case of uniform moment loading condition ($\alpha_L = 1, \beta = -1$), which required $P_1 = P_2$, the imbalance of transverse loads was compensated at every loading deviation $\Delta P = 10$ kN, with $\Delta P = |P_1 - P_2|$.

5.2.6. Instrumentation

Linear variable differential transformers (LVDTs) were employed for the displacement measurements and strain gauges (SGs) for strain measurements. The layout and location of the LVDTs and the SGs mounted on a cross-section are depicted in Figures 5.7 and 5.8, respectively. Due to the spatial restraint beneath the loading boxes, LVDT-1 and LVDT-2 were put aside and the mean of their readings was taken as the transverse displacement of specimens at the load level P_1 . A similar arrangement was used for measuring the displacement of specimens at the load level P_2 .

5.3. Test results and discussion

Specimen TB-890-1 was subjected to moment gradient ($\alpha_L = 0, \beta = -1/3$), while the other three specimens were loaded by a uniform bending moment ($\alpha_L = 1, \beta = -1$). The evolutions of the load-displacement relationships are plotted in Figure 5.9 and the buckling moments M_m at which lateral-torsional buckling occurred are given in Table 5.3. The deformed shape of the buckled TB-890-2 specimen is shown in Figure 5.11. The test set-up successfully allowed the global buckling responses of the web-tapered HSS I-beams to be investigated.

For the beam TB-890-1 which was under the linear moment gradient ($\beta = -1/3$), the critical section, at which the ratio of the applied bending moment to the plastic moment is greatest (EC3, AS4100), was the largest tapered section (the depth of the critical section $H_{cr} = H_1$). The buckling moment $M_m = 358$ kNm was significantly less than the nominal yield bending moment $M_{y,cr} = 602$ kNm and the nominal plastic moment $M_{p,cr} = 701$ kNm of the critical section so that the beam buckled in the elastic range. The specimen responded linearly to the load before the critical load was reached (Figure 5.9a). Since the largest twist displacement was estimated to occur at a location which was close to the mid-span and toward the largest tapered section, an array of strain gauges was mounted on the beam at three cross-sections, starting from the mid-span and then every 200 mm from the mid-span as illustrated in Figure 5.7. The compression flange strains versus the bending moment M are plotted in Figure 5.10. It can be seen that as the beam deflects sideways, the strains SG-1 in one flange tip reduce to become tensile, while the strains SG-3 in the other flange tip increase rapidly. The maximum compressive strains at the critical load were approximately $-4520 \mu\epsilon$, at which yielding occurred in the compression flange of the BISPLATE-100 HSS beam and subsequently inelastic lateral buckling occurred as demonstrated in Section 4.3.

For the specimens under uniform bending moment ($\beta = -1$), the critical section was the smallest tapered section (the depth of critical section $H_{cr} = H_2$). The test results showed that as the taper constant α_w increased, the buckling resistance of the tapered beams increased. It is noteworthy that the buckling of these tapered beams was in the inelastic range as the maximum applied moments were greater than the nominal yield moments $M_{y,cr}$ of the critical sections as shown in Figure 5.9, especially for the beam TB-890-2 whose buckling load even reached the nominal plastic moment $M_{p,cr}$ of its critical section, leading to the non-linear responses of the beam TB-890-2 when the applied

load passed the yield moment $M_{y,cr}$ as seen in Figure 5.9b. Accordingly, it is noted the lateral buckling of these specimens occurred not due to the yielding of smallest tapered sections which were fully restrained, but rather related to the yielding of compression flange of the section which had the largest twist displacement. While a few recent studies have proposed the first yield criterion approaches for the buckling strength of the non-prismatic steel members (Marques *et al.*, 2012; Marques *et al.*, 2013; Tankova *et al.*, 2018a; Tankova *et al.*, 2018b), the present experiments show that more experimental and analytical investigations are needed to evaluate the effects of load and restraint arrangements, material and geometric imperfections, and the variation of the steel materials on the buckling resistance of tapered steel beams.

No tensile fracture was observed during the testing of all specimens. The experimental results were used as the basis to calibrate a finite element (FE) model for tapered HSS I-beams as follows, which was used to conduct a parametric study and provide further discussion of the buckling behaviour of tapered HSS beams.

5.4. Numerical study

5.4.1. Finite element model

To augment the experimental data, a 3-dimensional finite element model (FEM) for thin-walled web-tapered HSS I-beams was constructed using ABAQUS software (2014) as shown in Figure 5.12 and the FEM was calibrated against the test results. A multi-linear elastic-plastic constitutive model (Figure 4.22) was applied for modelling the behaviour of the HSS material, associated with von Mises' yield criterion, plastic flow rule and isotropic hardening as is assumed for mild steel but with different limits. The

material constants assumed were the elastic modulus $E = 200$ MPa and Poisson's ratio $\nu = 0.25$.

The variation of the beam geometry and its imperfection can be represented a unique out-of-plumb imperfection shape taken as the eigenmode from an elastic buckling analysis with respect to the AS4100-1998 specification (2016). The measured out-of-plumb magnitudes in Table 5.3 are used in the test simulations of the specimens, and the nominal limit specified in AS4100, which is the larger value of span/1000 or 3 mm, is used in the parametric study.

The residual stress distribution in Figure 5.3 can be integrated in the FE models of specimens TB-890-1, TB-890-2, and TB-890-3 whose geometry is similar to the residual stress sample RS-TB-890. Alternatively, the residual stresses induced in HSS I-section beams can be represented by the pattern shown in Figure 3.23 with the magnitude of the tensile and compressive stresses obtained from Eqs. (3.7) to (3.11).

5.4.2. Validation of FEM

The critical bending moments M_b of the tapered beams obtained from the FE simulations are given in Table 5.3 and compared with the maximum experimental bending moment capacity M_m . The FE predictions are in good agreement with the test results with an average error of 7%, and standard deviation of 3%. The FE prediction for buckling load of the specimen TB-890-1 subject to moment gradient is close to the test result, and the FE models of the other specimens loaded in uniform bending moment slightly underestimate the buckling loads. The accuracy of the FE model is also demonstrated in Figure 5.13, which depicts the normalised bending moment (M/M_{p1}) plotted against the normalised displacement (u_y/H_1) obtained from the FE

model and the test results, where M_{p1} and H_1 are the plastic moment and the depth of the largest tapered section, respectively. The buckled deformations of the beam TB-890-2 captured by the FE model correlate reasonably well with the test results as seen in Figure 5.11.

5.4.3. Parametric study

The FE model was employed to conduct parametric studies of two tapered beams, viz. FE-TB-890-1 and FE-TB-890-2, representing the specimens TB-890-1 and TB-890-2, respectively. The FE models have the largest tapered sections, similar to the largest tapered sections of the specimens TB-890-1 and TB-890-2. The web-taper constant α_w , the length of the beam and the bending moment regime over the length (uniform bending and moment gradient) were the main variables. The effects of the taper constant α_w , the residual stresses and the flange compactness (represented by the flange-width) on the buckling resistance of the HSS tapered beams are discussed in the following subsections.

5.4.3.1. Effects of web-taper constant

The critical buckling moments M_b obtained from the FE model normalised with the plastic moment of the largest taper section M_{p1} were plotted against the beam parameter $K = \pi / \sqrt{(EI_w / GJL^2)}$ calculated for the largest taper section in Figure 5.14. The value of K represents the slenderness of the beam, with small values of K indicating slender beams and large values of K indicating stocky beams (Bradford, 1988).

It is evident that the buckling resistance of the web-tapered beam increases in proportion to the value of K , meaning that stockier beams inherit higher buckling

resistances. Larger buckling strength is also obtained from beams with a higher web-taper constant α_w in both loading scenarios. Furthermore, the effect of α_w on the buckling strength is most significant for intermediate and stocky tapered beams under uniform bending ($\beta = -1$). Nevertheless, the normalised buckling resistances tend to become independent of α_w when the beam slenderness increases.

5.4.3.2. Effects of residual stresses

The effects of residual stresses on the buckling strength of web-tapered beams are shown in Figure 5.15. It is seen that the residual stresses considerably reduce the buckling resistance of the beams and the buckling strength of the web-tapered beams is mostly affected by the residual stress distribution in the flange rather than that in the web as the reduction of the buckling strength seems independent of the web-taper constant α_w .

5.4.3.3. Effects of flange-width

The variation of the buckling resistance of the tapered beams with different flange widths is shown in Figure 5.16. It is seen that the tapered beam with a wider flange has a higher normalised buckling strength. This is because the second moment of area (about the minor axis) and the warping constant of the beam increase as the flanges are wider. In addition, the coupling of flange compactness and the web-taper constant α_w is seemingly insignificant.

5.5. Comparison of test results and FE model with design standards

This section discusses the applicability of EC3 (2005) and the AS4100-1998 (2016) to web-tapered beams fabricated from BISPLATE-100 HSS plates by comparing test results and FE predictions with the design provisions.

5.5.1. Eurocode 3

The General Method for calculating the nominal lateral-torsional buckling moment capacity M_b of tapered beams subject to pure bending moment in the European code EC3 can be interpreted as

$$M_b = \chi_{op} M_{Rk}, \quad (5.1)$$

where M_{Rk} is the nominal bending moment capacity of the most critical cross-section of the tapered beam, χ_{op} is the reduction factor for lateral-torsional buckling given by

$$\chi_{op} = \frac{1}{\Phi_{LT} + \sqrt{\Phi_{LT}^2 - \bar{\beta} \bar{\lambda}_{op}^2}} \leq 1, \quad (5.2)$$

where $\bar{\lambda}_{op} = \sqrt{M_{Rk}/M_{ob}}$ is the global non-dimensional slenderness, M_{ob} is the elastic lateral buckling moment of the tapered beam, and

$$\Phi_{LT} = 0.5 \left[1 + \alpha_{LT} (\bar{\lambda}_{op} - \bar{\lambda}_{op,0}) + \bar{\beta} \bar{\lambda}_{op}^2 \right]. \quad (5.3)$$

The Limited Method for rolled sections and equivalent welded sections in EC3 is considered in this assessment in which $\bar{\beta} = 0.75$, $\bar{\lambda}_{op} = 0.4$ and the value of the imperfection factor α_{LT} is recommended with respect to the height-to-width H/B ratio

and the type of the cross-section. The effect of the moment distribution on the buckling load is taken into account by a modified reduction factor $\chi_{op,mod}$ as

$$\chi_{op,mod} = \chi_{op} / f \leq 1, \quad (5.4)$$

with

$$f = 1 - 0.5(1 - k_c) \left[1 - 2.0(\bar{\lambda}_{op} - 0.8)^2 \right] \leq 1, \quad (5.5)$$

and the correction factor $k_c = 1/\sqrt{\alpha_m}$, where α_m is the moment modification factor.

The comparison between the EC3 (2005) and test results is shown in Figure 5.17. It is seen that the beam curves EC3 (c) and EC3 (d) provide a conservative estimation of the buckling resistance of the tapered HSS specimens. The extended experimental data obtained from the FE analysis and compared with the EC3 provisions in Figure 5.18 and 5.19 shows that the EC3 curve (c) approximates the lower bound of the data for the moment gradient condition ($\beta = -1/3$).

For the uniform bending moment condition ($\beta = -1$) in Figure 5.19, the EC3 curves (c) and (d) are too conservative in estimating the buckling strength of the tapered HSS beams. The gap between the EC3 provisions and FE predictions becomes significant when the taper constant α_w decreases and the flange width increases. The effect of the flange width on the buckling resistance of the beam has been discussed previously. On the other hand, the effect of α_w on the normalised buckling strength M_b/M_{Rk} is related to the EC3 design method. In particular, when the moment is uniform, the critical section capacity M_{Rk} is calculated with respect to the smallest tapered section, but it is evident from the tests that the stability of the specimens is governed by the yielding of the

section whose twist displacement is greatest rather than the yielding of the smallest tapered section which was fully restrained. Therefore, the EC3 design method becomes conservative when the tapered segment is subject to uniform bending moment. In contrast, when the largest tapered section is the critical section for calculating the section capacity as in the case of moment gradient loading (Figure 5.18), the normalised buckling strength M_b/M_{Rk} slightly increases as the taper constant α_w increases.

5.5.2. AS4100

In the Australian standard AS4100-1998 (2016), the nominal buckling moment capacity of tapered I-section beams is obtained from

$$M_b = \alpha_m \alpha_s M_s, \quad (5.6)$$

where M_s is the critical section moment capacity, α_m the moment distribution modification factor and α_s the slenderness reduction factor that can be obtained from

$$\alpha_s = 0.6 \left(\sqrt{\lambda_s^4 + 3} - \lambda_s^2 \right) \leq 1, \quad (5.7)$$

where $\lambda_s = \sqrt{M_s/M_{oa}}$ is the modified slenderness and M_{oa} the reference elastic buckling bending moment excluding the effect of non-uniform moment distribution.

A revision to AS4100 for buckling bending load carrying capacity of HSS flexural members was proposed in Section 4.6 by incorporating a coefficient γ_m which accounts for material characteristics of high strength steels into the slenderness reduction factor formula as

$$\alpha_s = \left[\sqrt{\gamma_m^2 \lambda_s^4 + \left(1 - \frac{0.6}{\gamma_m}\right) \lambda_s^2 + 1.08} - \gamma_m \lambda_s^2 \right] \leq 1, \quad (5.8)$$

and the bending moment capacity in Eq. (5.6) then takes the form

$$M_b = \alpha_m \alpha_s M_s \leq \min \{M_{ob}, M_s\}. \quad (5.9)$$

The value of the material coefficient is recommended as $\gamma_m = 0.7$ for the HSS beams with nominal yield stress greater than 690 MPa and $\gamma_m = 0.6$ for flexural members made of mild steel.

The comparison of tests results and FE predictions with the AS4100 model and the proposed formulae for HSS beams is presented in Figure 5.20 – 5.22. In general, the Australian design provisions are conservative in estimating the buckling strength of web-tapered BISPLATE-100 HSS specimens. A marginal approximation of the AS4100 model to the FE predictions is obtained for stocky beams ($\lambda_s < 1$) under moment gradient loading ($\beta = -1/3$) as seen in Figure 5.21, whilst the proposed curve estimates the mean of FE data with acceptable accuracy.

Because the AS4100 shares the same design concept as EC3, similar effects of the web-taper constant α_w and the flange-width to the normalised buckling strength M_b/M_s can be seen in Figure 5.21 and 5.22 in which M_b/M_s increases with the decrease of α_w when the smallest section is taken as the critical section, and M_b/M_s slightly increases with the increase of α_w when the largest section is the critical section. Nevertheless, both the AS4100 model and the proposed curve underestimate the buckling strength of web-tapered HSS beams subject to uniform bending moment as seen in Figure 5.22.

5.6. Conclusions

A preliminary experimental study of the buckling behaviour of web-tapered beams fabricated from Australian BISPLATE-100 high-strength steel (HSS) plates was carried out in this study. A total of four specimens were tested under uniform bending moment and linear bending moment gradient. The special design of the test set-up for lateral-torsional buckling of the tapered I-beams was presented in detail and the results of the material tests, out-of-plumb imperfection measurements and residual stress patterns in a web-tapered beam were included. The test design successfully captured the global buckling response of the welded tapered beams subject to different loading conditions. Finite element (FE) models of the web-tapered HSS beams were constructed and good agreement between the FE predictions and test results was achieved. Parametric studies of the effects of the taper constant, residual stresses and flange-width on the buckling resistance of the tapered beam have been presented. The adequacy of the EC3 and AS4100 design provisions for predicting the buckling strength of the web-tapered HSS beams was evaluated. Based on the results of the laboratory experiments and of the FE simulations, the following conclusions can be drawn.

- The inelastic lateral-torsional buckling of a web-tapered beam is governed by yielding of the section whose twist displacement is greatest.
- The buckling strength of tapered beams is proportional to the web taper constant α_w . Moreover, the effect of α_w on the buckling strength is most significant in intermediate and stocky web-tapered beams under uniform bending moment ($\beta = -1$). Nevertheless, the normalised buckling resistances tend to become independent of α_w when the beam slenderness increases.
- The buckling resistance of web-tapered beams is noticeably affected by the residual

stress distributions in the flange rather than those in the web.

- The normalised buckling resistance increases when increasing the flange-width of web-tapered beams and the coupling of flange compactness and the web-taper constant α_w is seemingly insignificant.
- Both the EC3 and AS4100 provisions are conservative for web-tapered HSS beams subject to uniform moment bending as the smallest taper section is taken for calculating the nominal moment capacity. The beam curve (c) of the EC3 limited method approximates a lower bound of the normalised buckling strength of web-tapered HSS beams under moment gradient, whilst the mean of the FE predictions is obtained by using the proposed formula for the buckling load carrying capacity of HSS flexural members with respect to the AS4100 method.

Table 5.1: Specimen cross-section dimensions

No.	Notation	f_y (MPa)	H_1 (mm)	H_2 (mm)	B (mm)	t_f (mm)	t_w (mm)	λ_f	λ_{w1}	λ_{w2}	α_w
1	TB-890-1	890	354	184	120	11.80	7.95	4.75	41.56	20.18	0.5
2	TB-890-2	890	354	184	160	11.80	7.95	6.44	41.56	20.18	0.5
3	TB-890-3	890	354	214	160	11.80	7.95	6.44	41.56	23.95	0.6
4	TB-890-4	890	354	254	160	11.80	7.95	6.44	41.56	28.98	0.7
5	RS-TB-890	890	354	184	160	11.80	7.95	6.44	41.56	20.18	0.5

Table 5.2: Average tensile and compressive residual stresses in the tapered sample RS-TB-890

No.	Section	f_y (MPa)	H (mm)	B (mm)	t_f (mm)	t_w (mm)	σ_{rft} (MPa)	σ_{rwt} (MPa)	σ_{rfc} (MPa)	σ_{rwc} (MPa)
1	RS-890-1	890	326	160	11.8	7.95	854	-	-102	-59
2	RS-890-2	890	269	160	11.8	7.95	-	690	-	-77
3	RS-890-3	890	212	160	11.8	7.95	-	606	-	-49

Table 5.3: Buckling resistance of tapered beam specimens

No.	Specimen	Slenderness*		L (m)	L_o (m)	L_1 (m)	$D_{i,max}$ (mm)	β	H_{cr}	$M_{p,cr}$ (kNm)	M_m (kNm)	M_b (kNm)	M_b/M_m	Failure mode
		Flange	Web											
1	TB-890-1	NC	C	6.4	3.00	1.50	2.00	-1/3	H_1	701	358	351	0.98	LTB
2	TB-890-2	NC	C	7.4	3.50	1.75	2.00	-1.0	H_2	376	375	343	0.91	LTB
3	TB-890-3	NC	C	7.4	3.50	1.75	2.50	-1.0	H_2	453	417	378	0.91	LTB
4	TB-890-4	NC	C	6.4	3.00	1.50	2.00	-1.0	H_2	562	510	473	0.93	LTB
Average													0.93	
Standard deviation													0.03	

Notes: * Section slenderness classified based on the actual material properties, C = Compact, NC = Non-Compact, H_{cr} = Depth of critical section, $M_{p,cr}$ = Plastic moment of critical cross-section, M_m = Maximum buckling strength according to the test, M_b = Maximum buckling strength based on FE model, LTB = Lateral-torsional buckling.

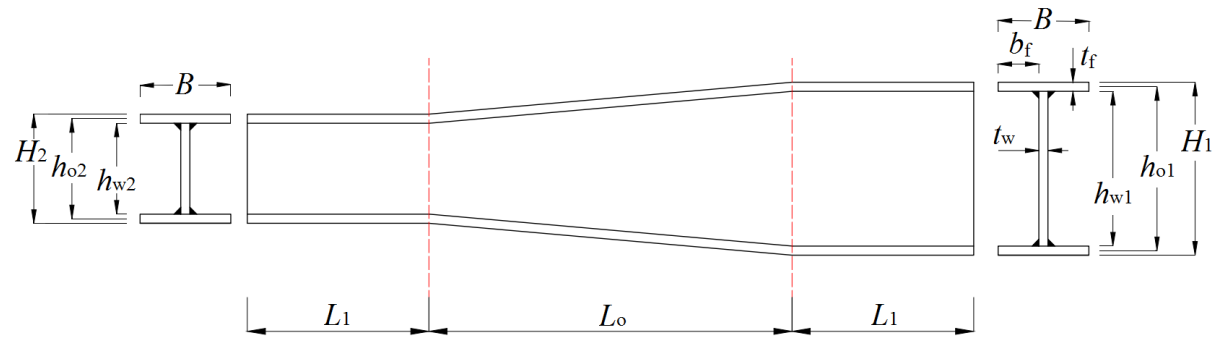


Figure 5.1: Geometry of web-tapered beams.



Figure 5.2: Specimen TB-890-2.

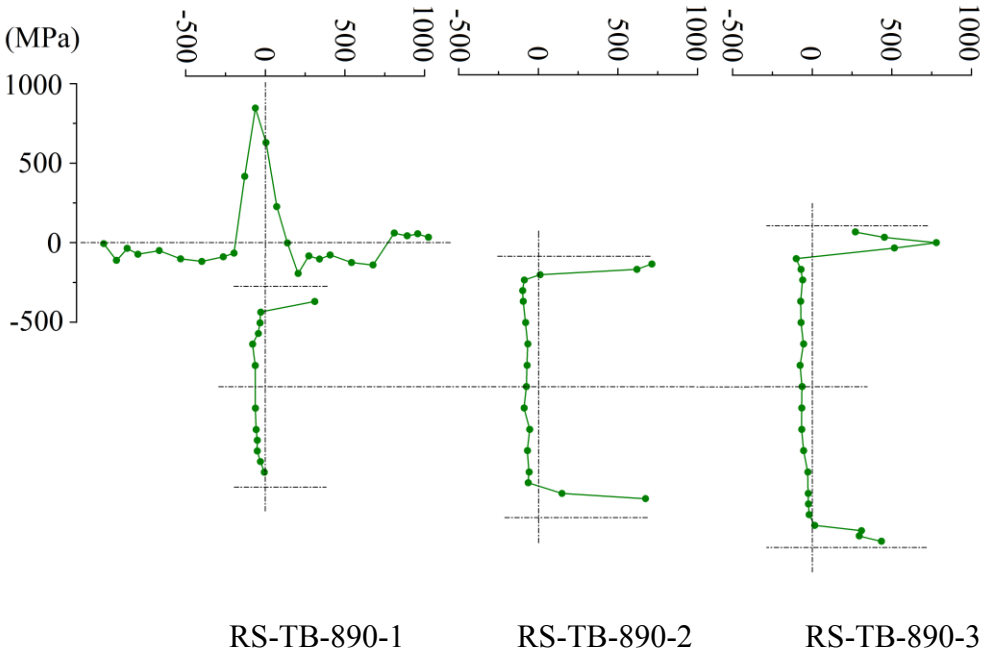
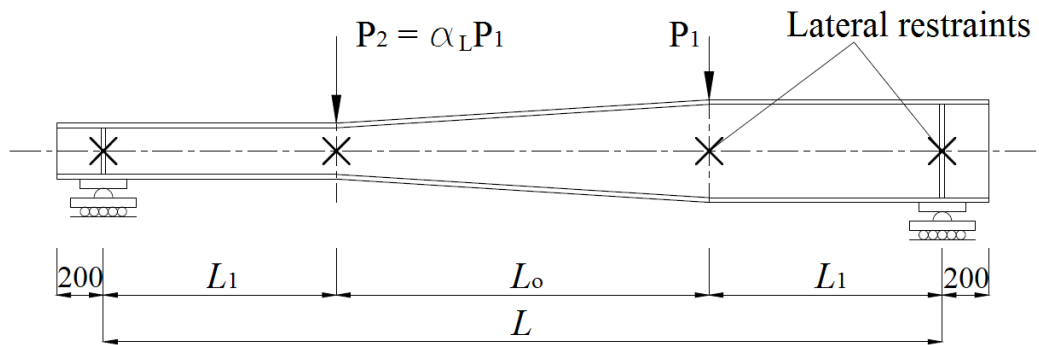
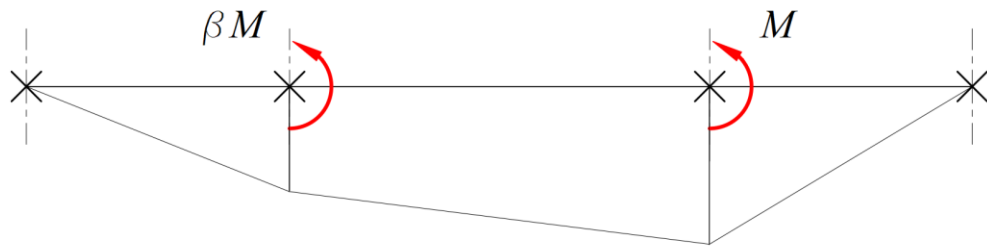


Figure 5.3: Residual stresses in the web-tapered beam RS-TB-890.



Loading arrangement



Bending moment diagram



Figure 5.4: LTB test set-up for web-tapered beams.

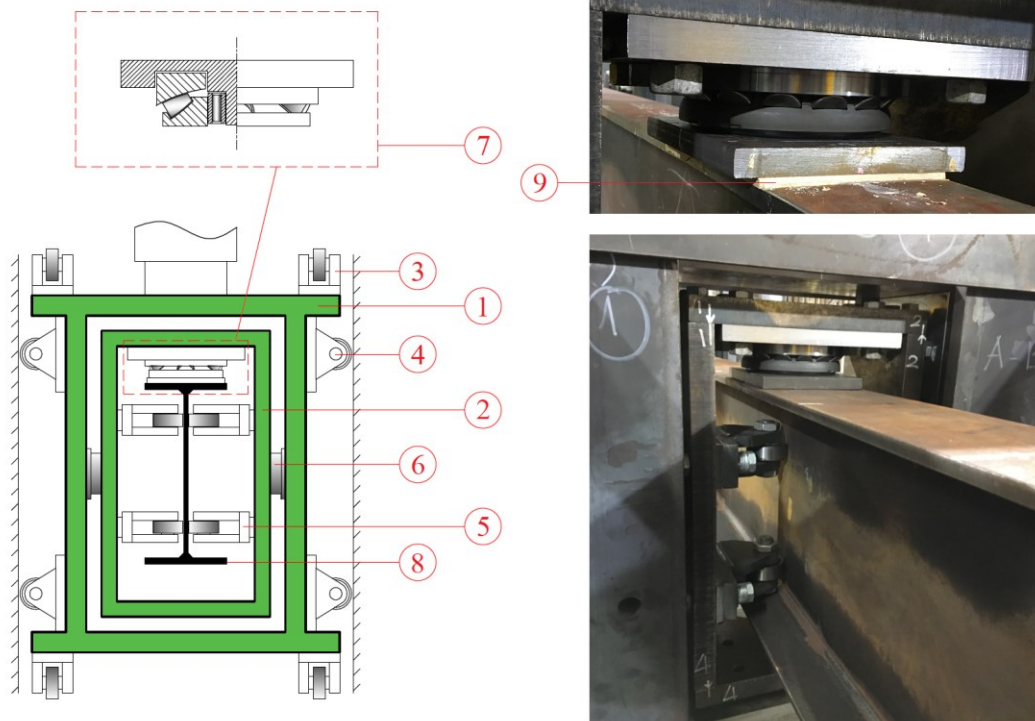


Figure 5.5: Loading box in the test of web-tapered beams.

(1) outer box, (2) inner box, (3-5) roller bearings, (6) spherical roller bearings, (7) modified spherical thrust roller bearing, (8) I-beam specimen, and (9) high compressive strength plaster.

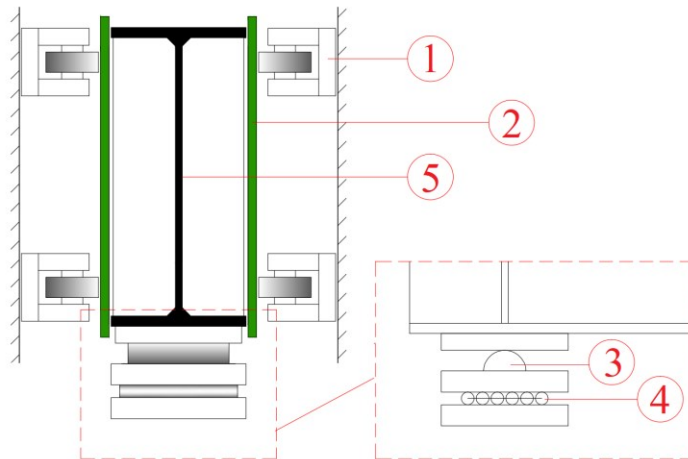


Figure 5.6: End restraint in the test of web-tapered beams

(1) roller bearings, (2) flat plates attached to stiffeners, (3) semi-circle bar, (4) rollers, and (5) I-beam specimen.

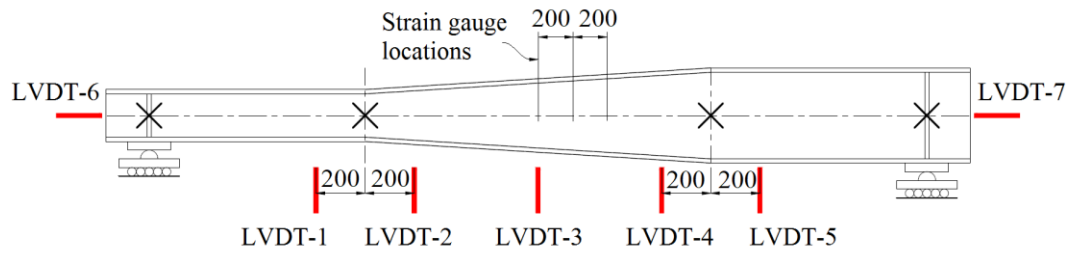


Figure 5.7: LVDT layout for web-tapered beams.

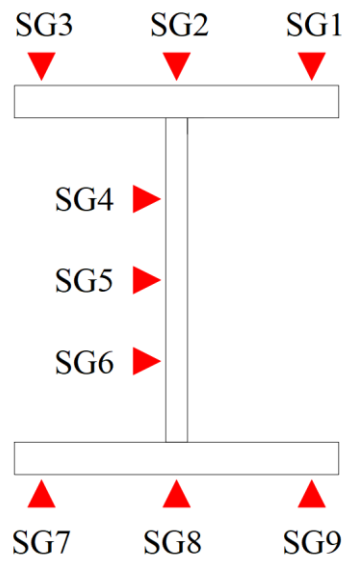
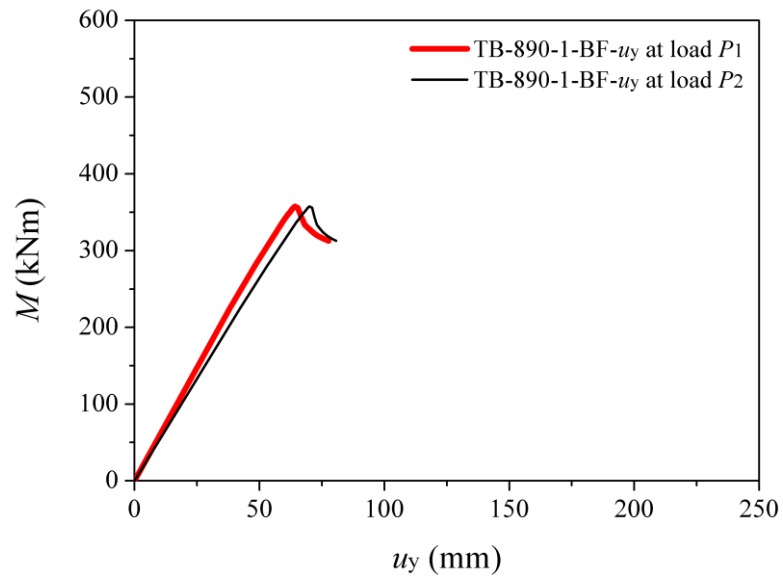
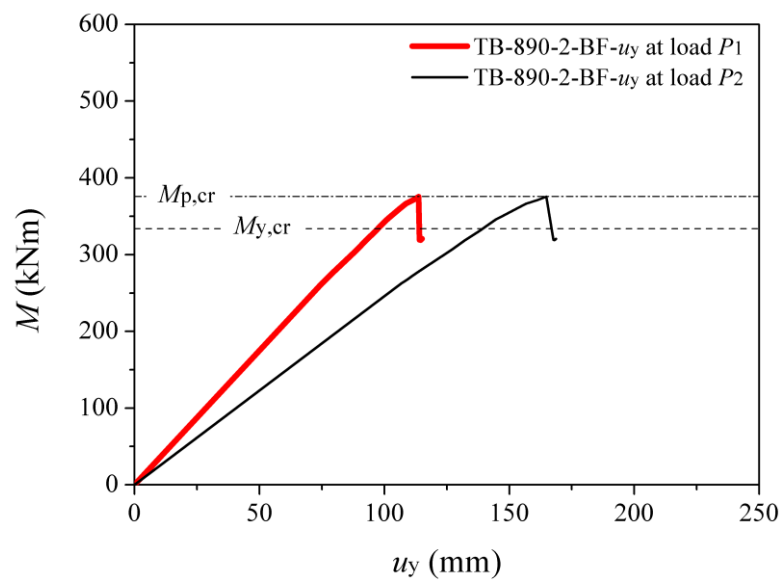


Figure 5.8: Strain gauge layout at a cross-section.



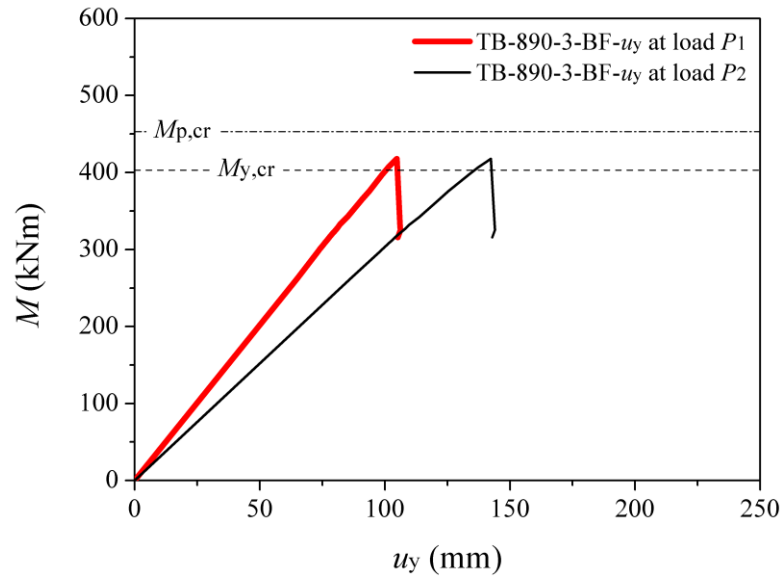
(a)



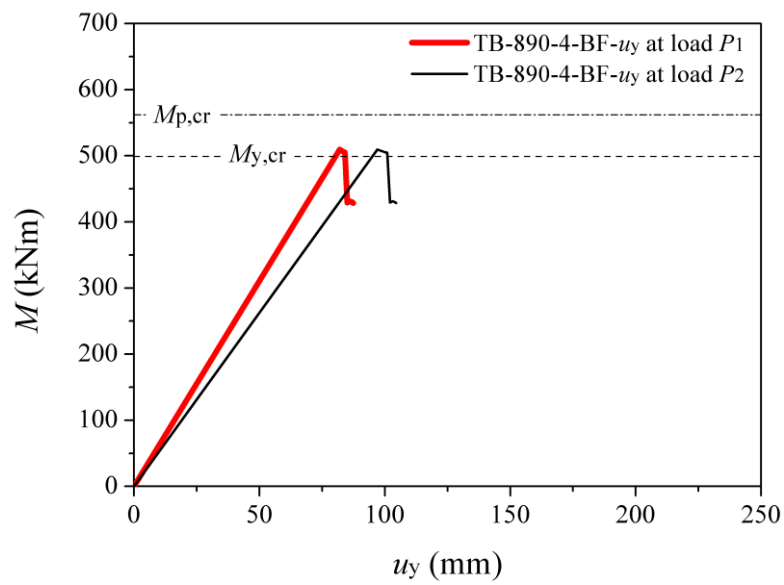
(b)

Figure 5.9: Load-displacement relations of web-tapered beams.

(BF = bottom flange centre, u_y = transverse displacement).



(c)



(d)

Figure 5.9 (cont.)

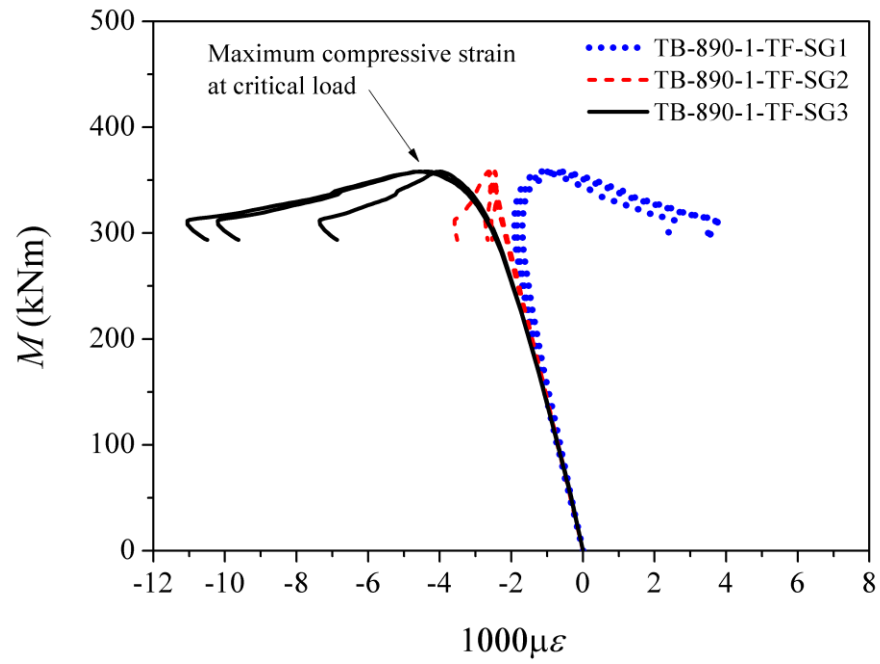


Figure 5.10: Longitudinal strain development in compression flange of the specimen

TB-890-1.

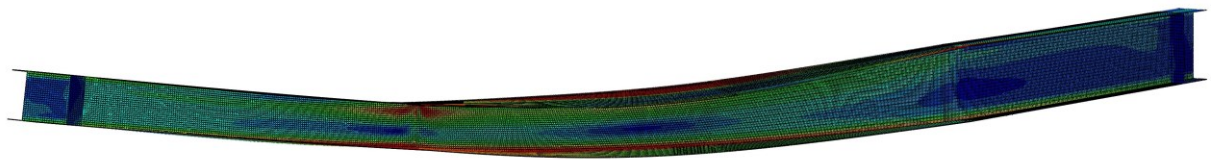
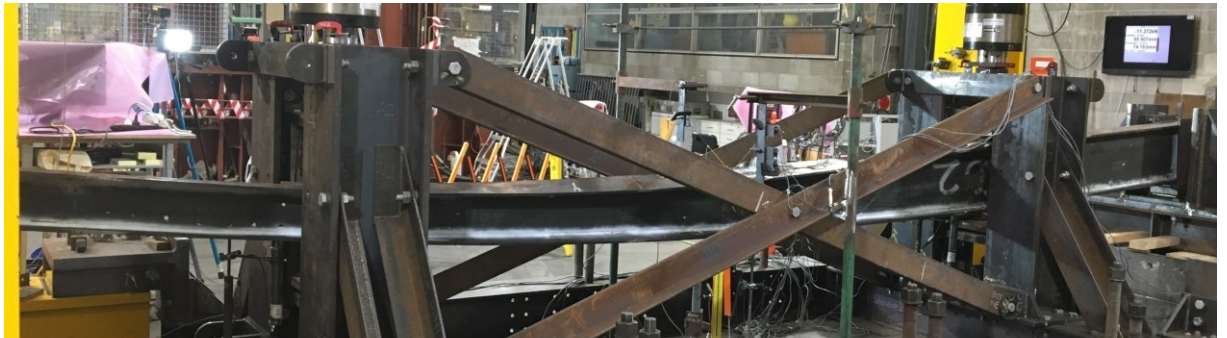


Figure 5.11: Deformed shape of the specimen TB-890-2.

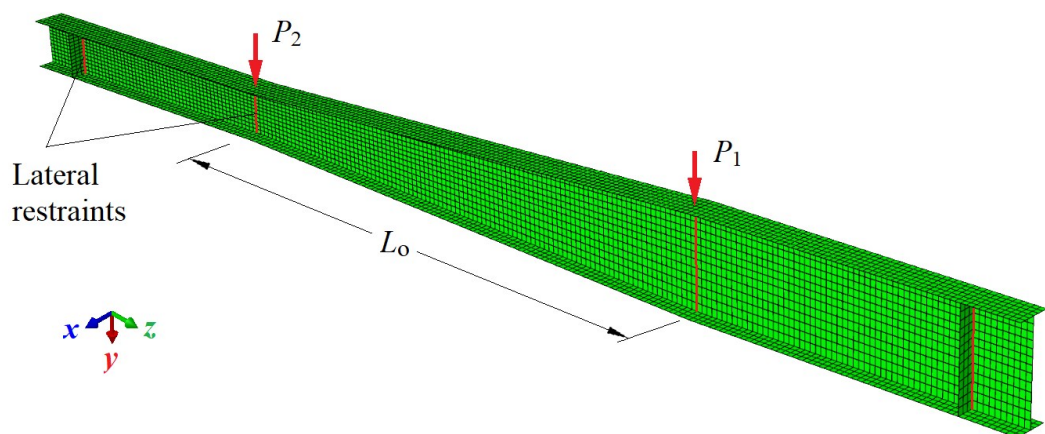
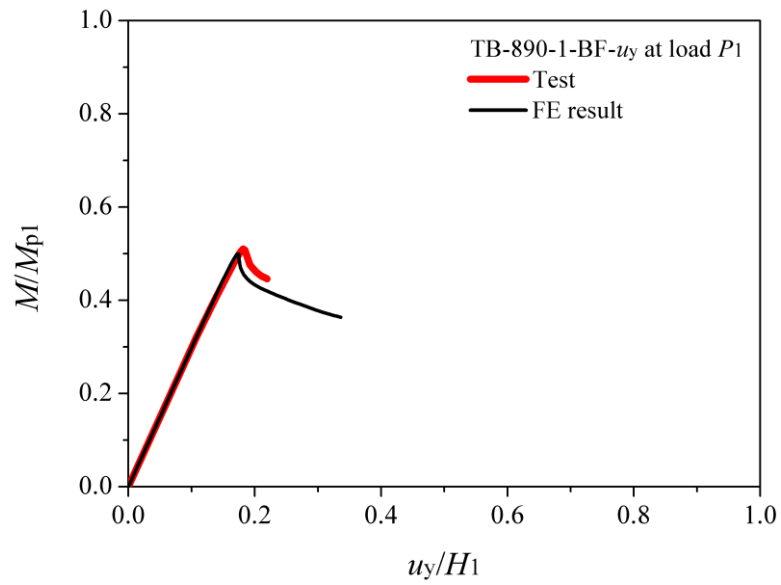
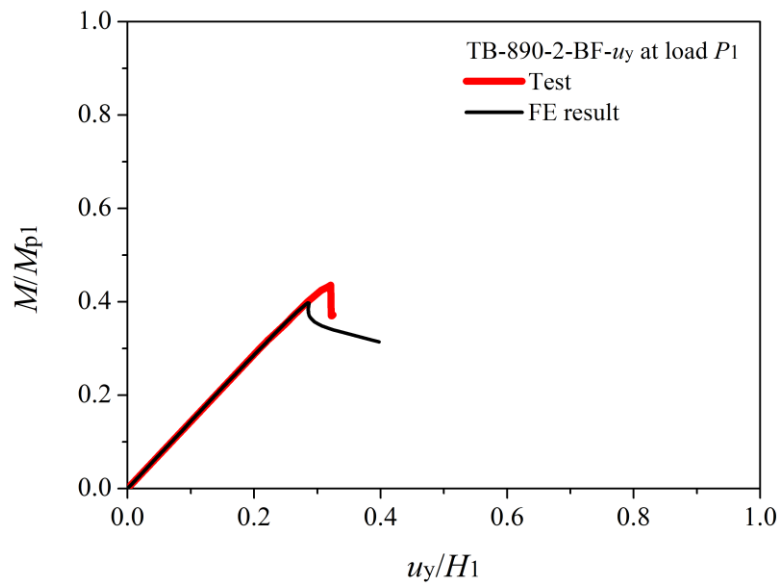


Figure 5.12: Finite element model of web-tapered beams.

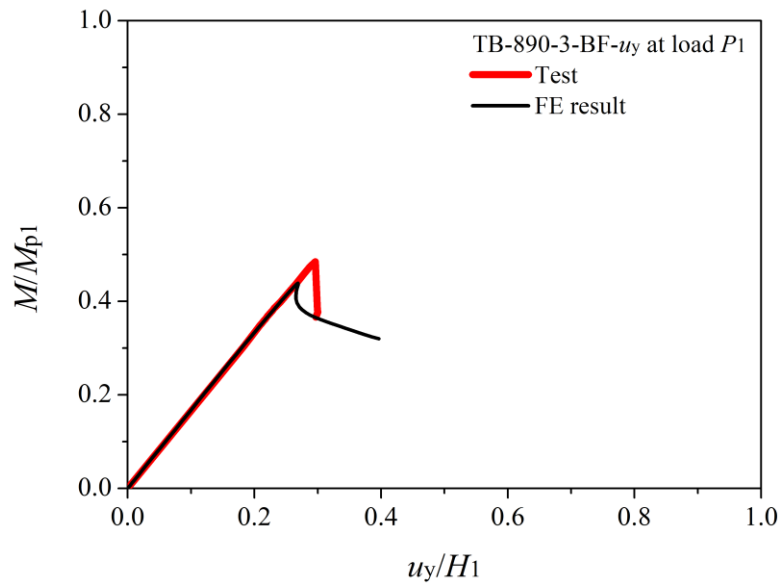


(a)

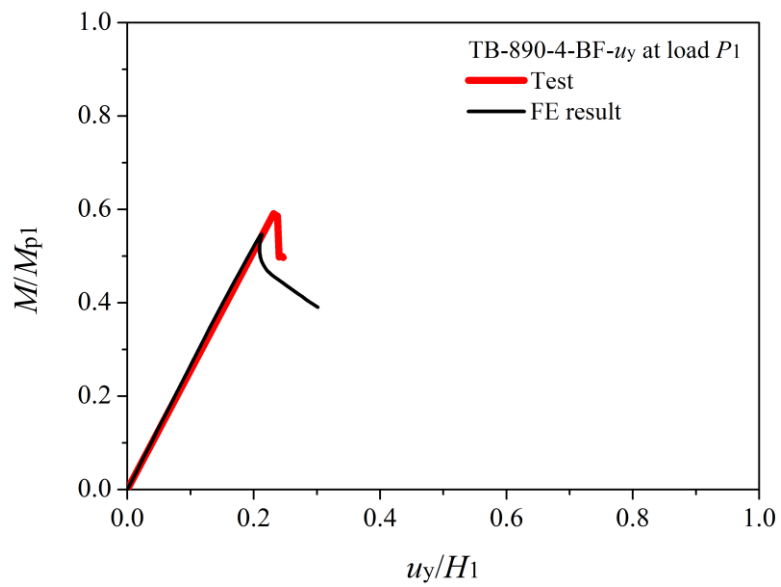


(b)

Figure 5.13: Normalised load-displacement relations of web-tapered beams.

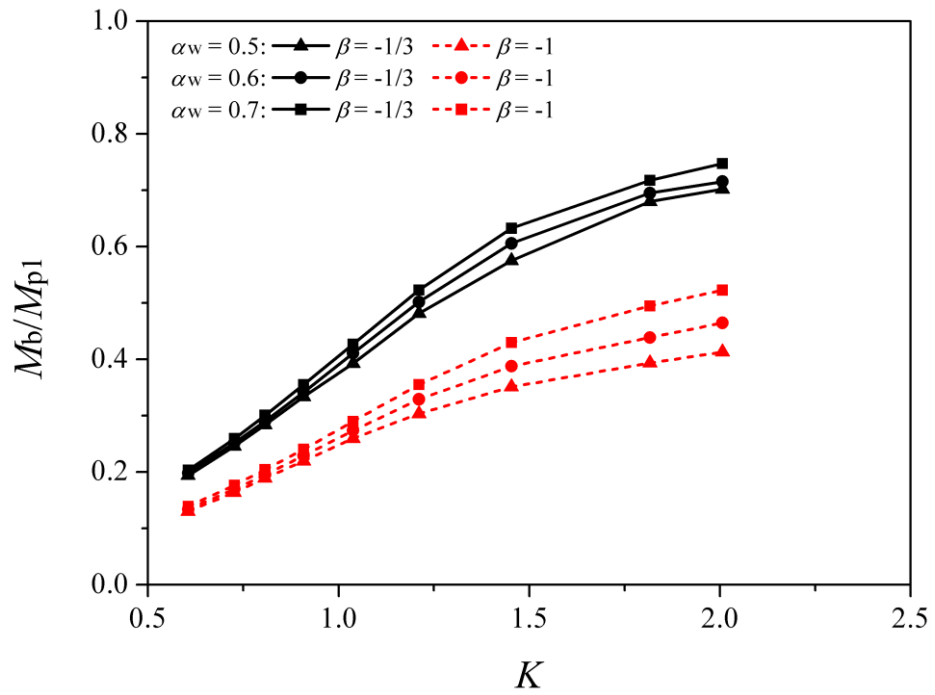


(c)

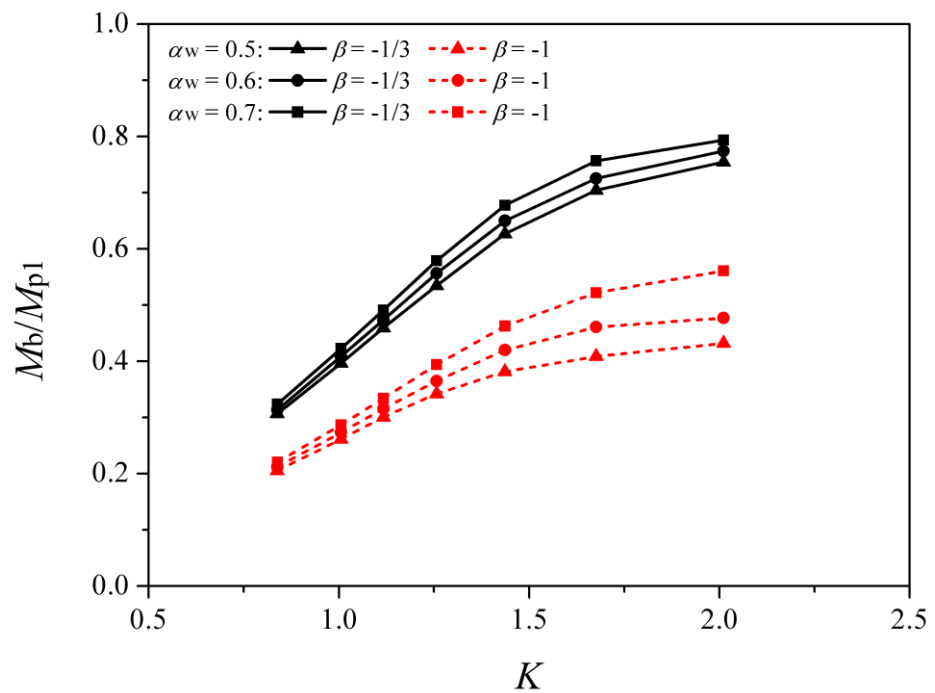


(d)

Figure 5.13 (cont.)

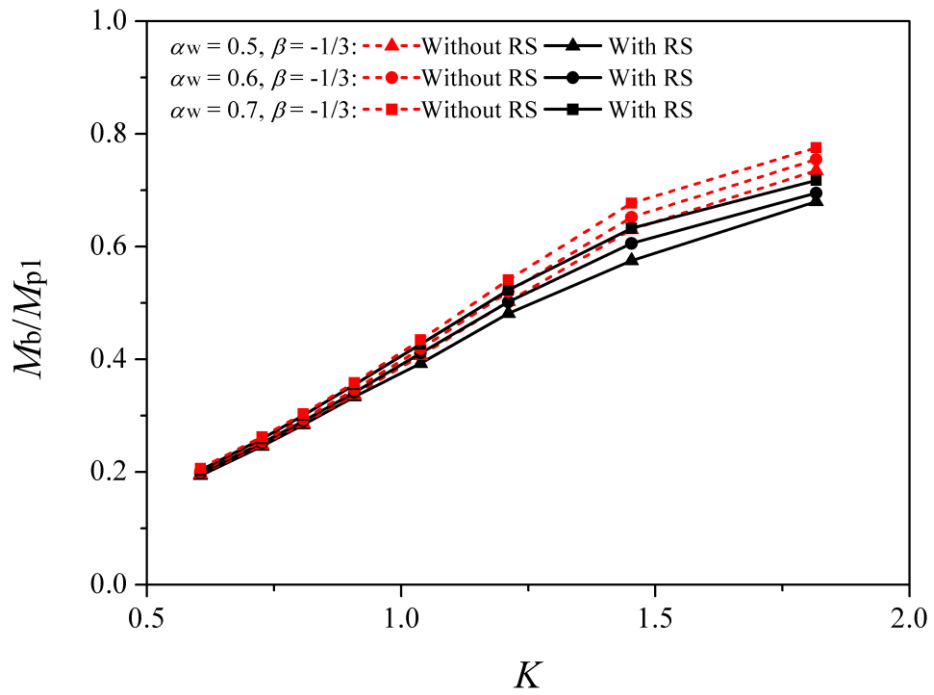


(a) FE-TB-890-1 (flange-width $B = 120$ mm)

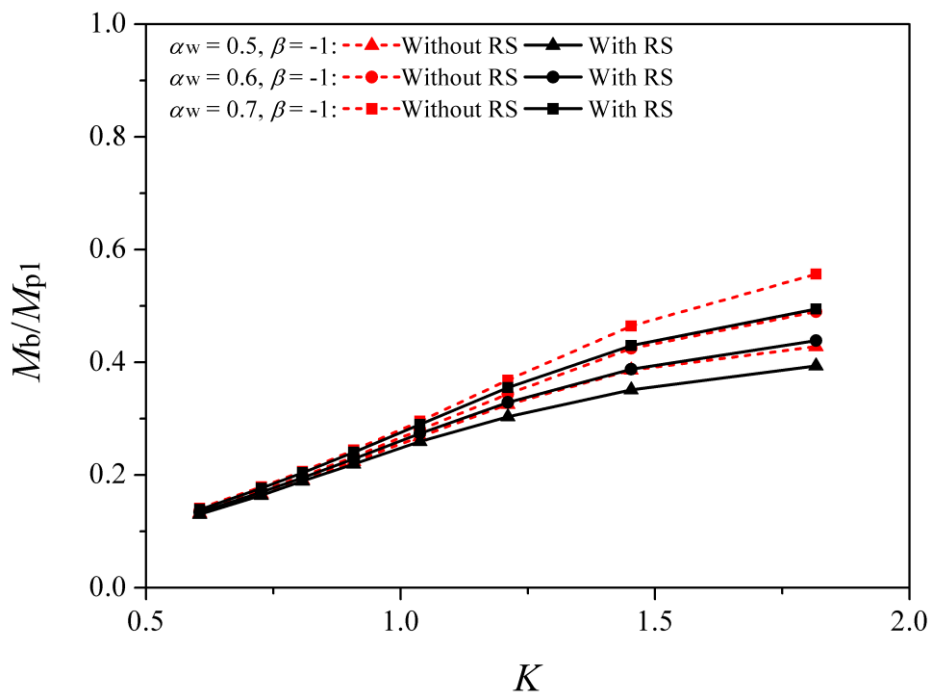


(b) FE-TB-890-2 (flange-width $B = 160$ mm)

Figure 5.14: Effects of web-taper constant α_w on buckling resistance.

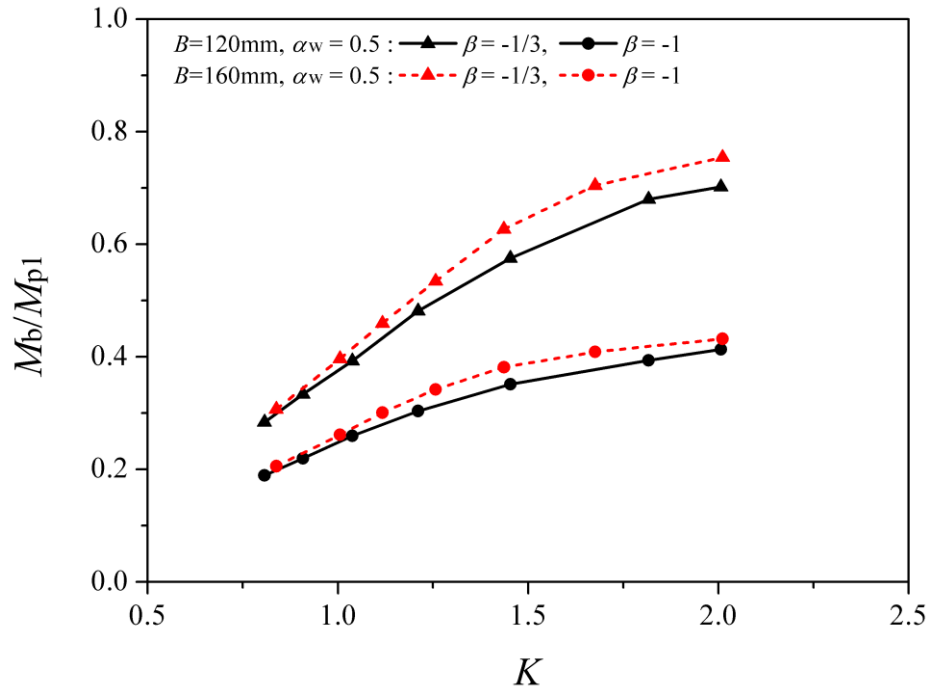


(a) FE-TB-890-1 under uniform bending moment ($\beta = -1$)

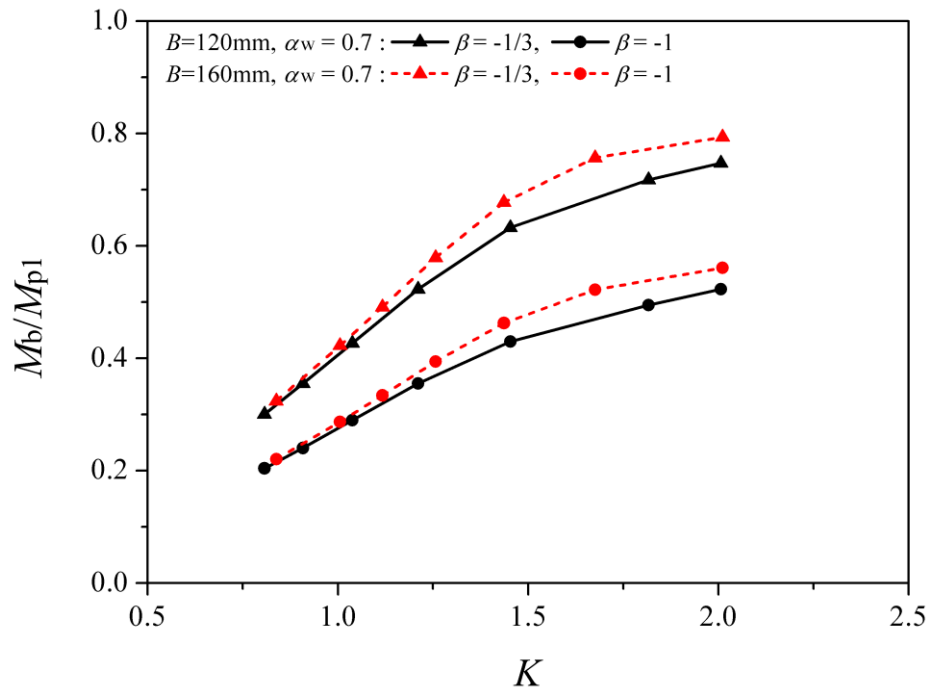


(b) FE-TB-890-1 under moment gradient loading ($\beta = -1/3$)

Figure 5.15: Effects of residual stresses on buckling resistance of web-tapered beams.



(a) Taper constant $\alpha_w = 0.5$



(b) Taper constant $\alpha_w = 0.7$

Figure 5.16: Effects of flange-width on buckling resistance of web-tapered beams.

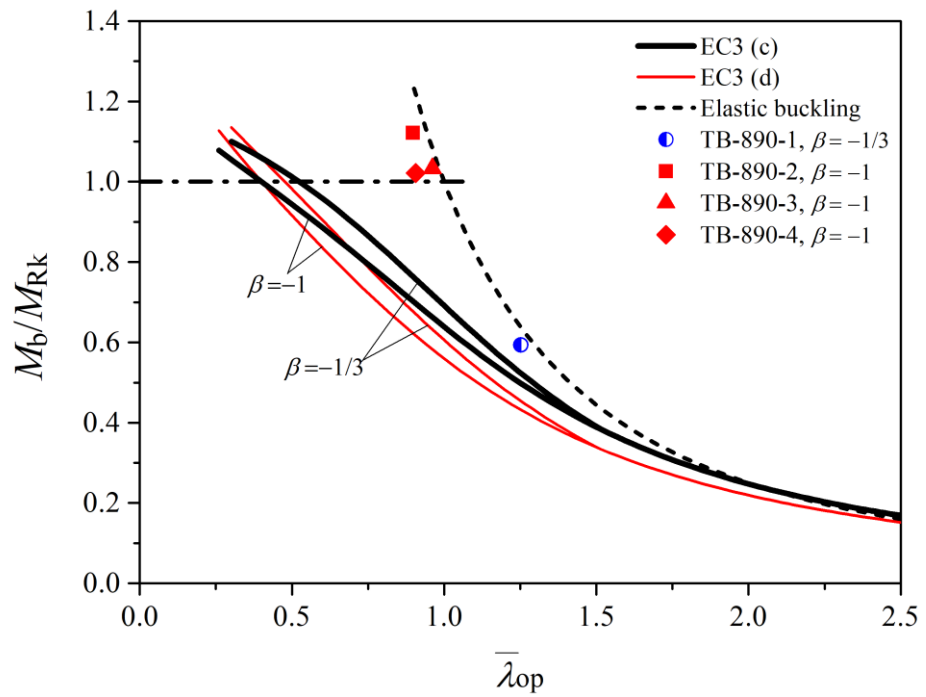


Figure 5.17: Comparison between test results and EC3 limited method.

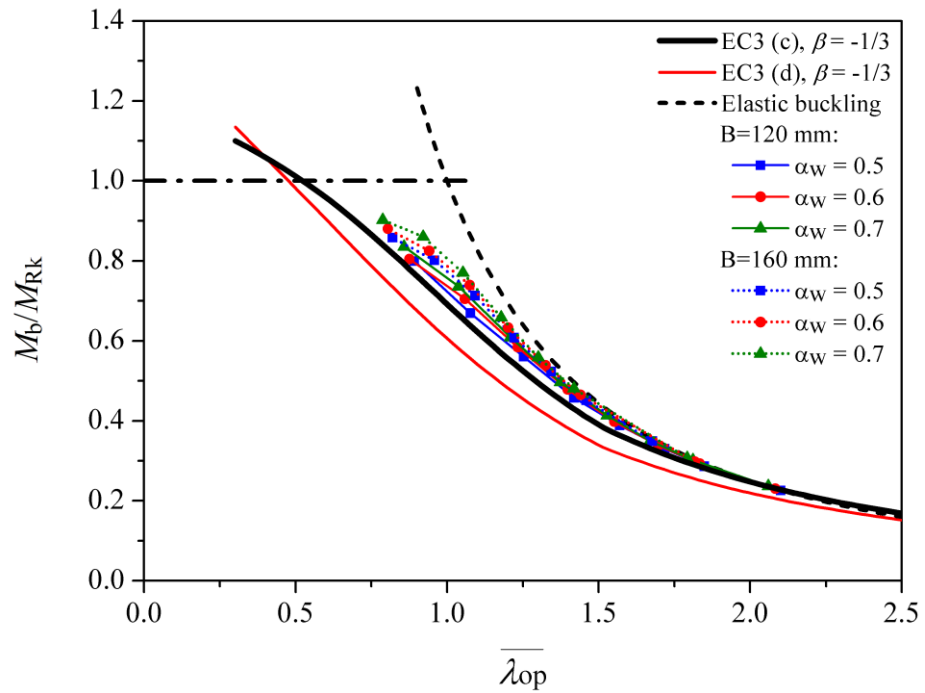


Figure 5.18: Comparison between FE predictions and EC3 limited method in the case of moment gradient loading ($\beta = -1/3$).

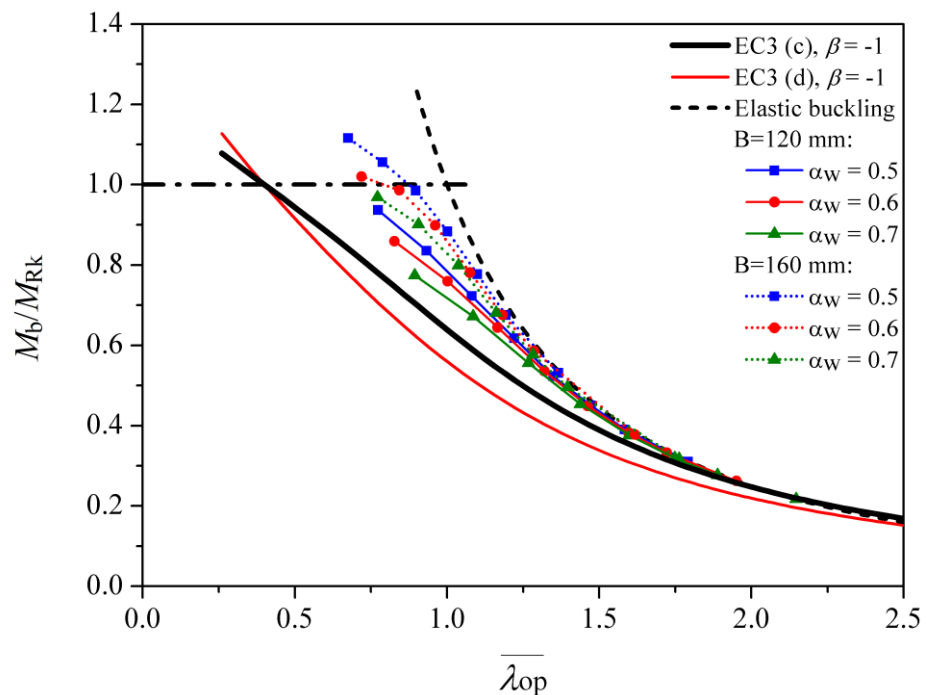


Figure 5.19: Comparison between FE predictions and EC3 limited method in the case of uniform bending moment ($\beta = -1$).

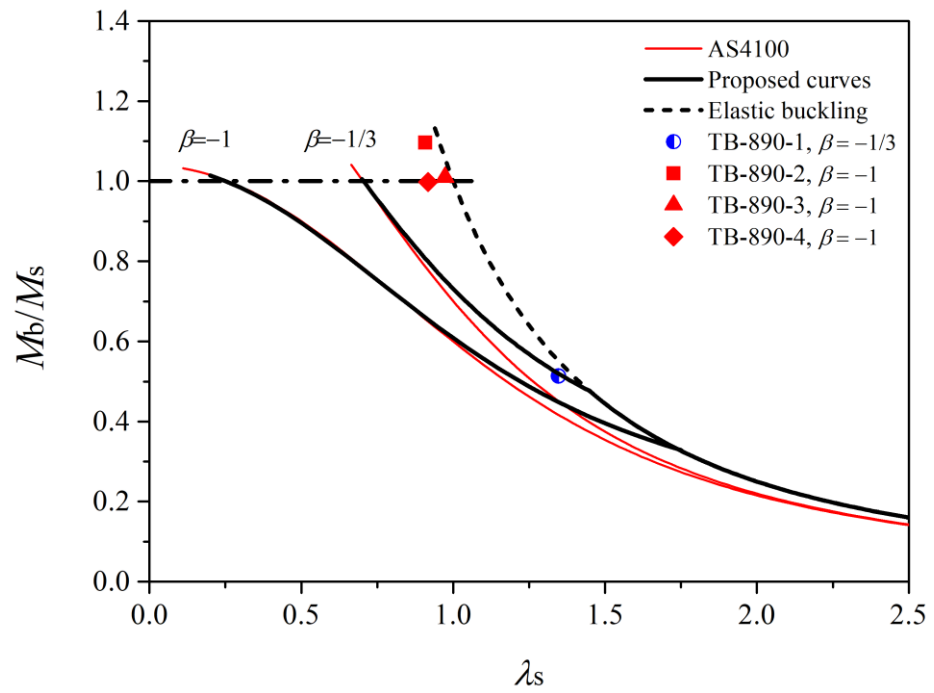


Figure 5.20: Comparison between test results and AS4100.

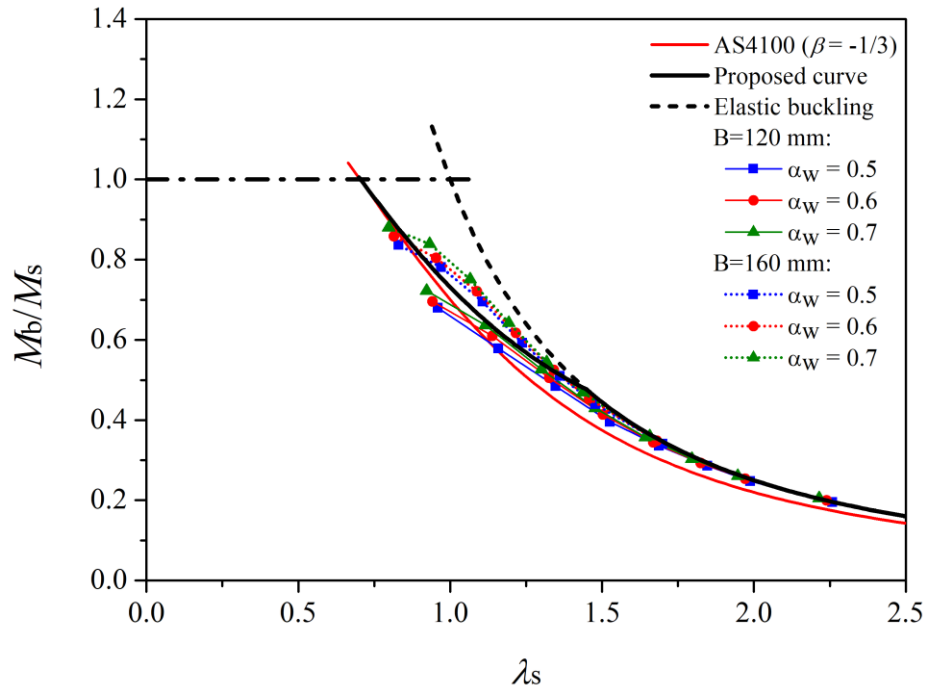


Figure 5.21: Comparison between FE predictions and AS4100 in the case of moment gradient loading ($\beta = -1/3$).

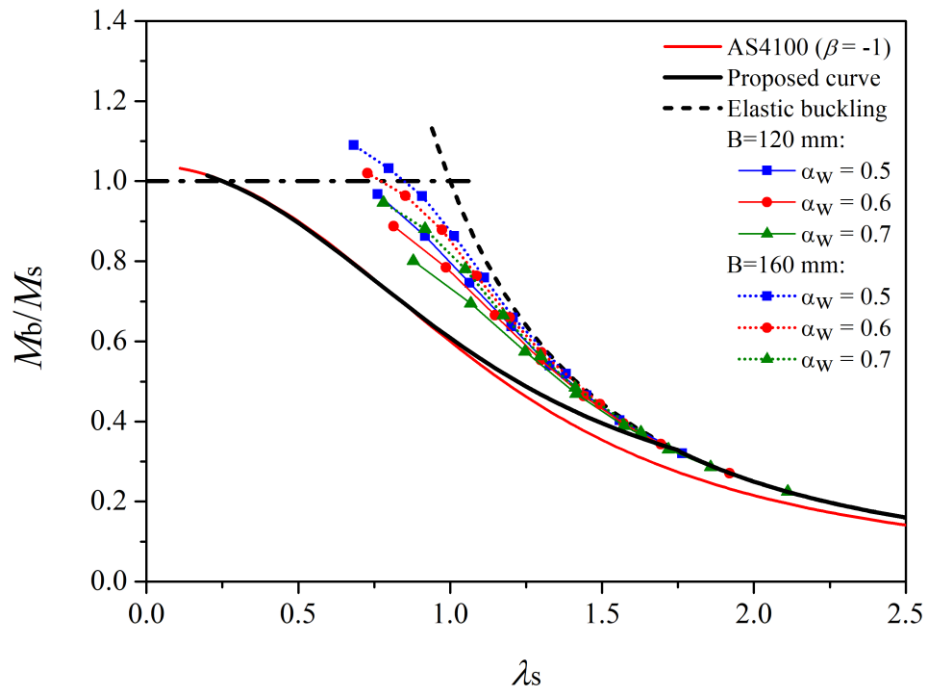


Figure 5.22: Comparison between FE predictions and AS4100 in the case of uniform bending moment ($\beta = -1$).

CHAPTER 6 SUMMARY, CONCLUSIONS AND RECOMMENDATIONS

6.1. Summary and conclusions

The thesis has investigated the buckling of I-beams of uniform cross-section and of web-tapered section fabricated from high-strength steel (HSS) plates with a yield strength in excess of 690 MPa. Chapter 3 presented the measurement of the residual stress distribution in welded HSS I-sections obtained using the neutron diffraction method. Specifically, prismatic and web-tapered beams with nominal yield strengths of 690 MPa and 890 MPa were investigated. The method is shown capable of obtaining a high spatial resolution of residual stresses with accuracy, especially the capacity to resolve the high stress gradient in the heat-affected zone thanks to the deep penetration of the neutral particles into the material. The following conclusions can be drawn.

- The peak tensile stresses at the flange-web junction were on average 70% of the measured yield stress, or 80% of the nominal yield stress of the parent material.
- The tensile stresses in the weld bead were on average 60% of the nominal yield strength of the parent steel.
- Compressive residual stresses were located outside of the heat affected zone and were independent of the steel grade. In deference to wide flange column-type sections, the residual stresses at the flange tips were compressive.

- Interaction of the flange and web were found to be insignificant regarding their residual stresses, so each of these elements could be assumed to be self-equilibrating. The effect of tapering had negligible effect on the residual stresses.

Based on the test results and augmented with further test data in the literature, a model of the residual stresses in HSS I-section flexural members was proposed, in which the compressive residual stresses were formulated as a function of the section thickness and slenderness. The proposal correlated well with test results and was particularly accurate when the beam depth exceeded the flange width, which is representative of bending members, and when used in a FE simulation, it predicted the failure modes of HSS members reported elsewhere. This proposed formulation can be used in numerical modelling for steel of grade 460 MPa and greater.

Chapter 4 presented an experimental study of the buckling behaviour of HSS I-beams of uniform cross-section. Eight homogeneous I-beams fabricated from BISPLATE-80 ($f_y = 690$ MPa) and BISPLATE-100 ($f_y = 890$ MPa) were tested under conditions of uniform bending and linear bending moment gradient. The test design successfully captured the buckling response of the welded HSS I-beams, including their lateral-torsional buckling and flange local buckling failure modes. The versatility of the devised testing rig under different loading scenarios was also demonstrated. Finite element (FE) modelling of the HSS beams was carried out using ABAQUS software and good agreement between the FE and test results was achieved. The FE models were then used to extend the experimental data by varying the beam slenderness and the adequacy of existing standard design provisions for predicting the bending moment capacity of HSS beams were evaluated. The following conclusions were drawn from the results of the laboratory experiments and the FE simulations.

- BISPLATE-100 beams have slightly higher normalised buckling resistances compared to BISPLATE-80 beams due to the less pronounced effects of the residual stresses in the higher-strength steel sections.
- The buckling strength of an I-section is related to the flange and web slenderness. Accordingly, an optimal cross-section for maximising the loading resistance and minimising material use can be obtained and should be considered in the design practice.
- Because of the residual stresses, the onset of yielding can commence before attainment of the yield moment, leading to a non-linear response of the beam. The bending strength of the beam still increases due to the onset of strain-hardening until reaching the flange local buckling moment.
- The flexural-torsional buckling is related to partial yielding of the critical cross-section as the instability occurred when the stresses in the compression flange were non-linear.
- The ANSI/AISC 360-16 marginally approximates the buckling strength of the HSS specimens but overly estimates the FE predictions. On the other hand, based on extended numerical data, the less conservative beam curve (d) of EC3 provides a good approximation of the buckling resistance of the HSS stocky beams under uniform bending, but it is conservative in the cases of intermediate and slender beams, as well as when the moment is distributed non-uniformly. The AS4100 closely estimates the bending strength of HSS stocky beams in both loading scenarios, but it too is conservative when the beam slenderness is greater than unity.

- A revision to the AS4100 has been proposed by introducing a coefficient γ_m related to the material characteristics of steel into the slenderness reduction factor formula. The value $\gamma_m = 0.7$ is recommended for flexural members fabricated from HSS with nominal yield stresses greater than 690 MPa, while $\gamma_m = 0.6$ is applicable for mild steel flexural members.

Chapter 5 presented a preliminary experimental study of the buckling behaviour of web-tapered beams fabricated from BISPLATE-100 plates. A total of four specimens were tested under uniform bending moment and linear bending moment gradient. The special test set-up successfully captured the global buckling response of the welded tapered beams subject to different loading conditions. FE models of the web-tapered HSS beams were constructed and good agreement between the numerical predictions and test results was achieved. Parametric studies of the effects of the taper constant, residual stresses and flange-width on the buckling resistance of the tapered beam have been presented. The adequacy of the EC3 and AS4100 design provisions for predicting the buckling strength of the web-tapered HSS beams was evaluated. Based on the results of the laboratory experiments and of the FE simulations, the following conclusions can be drawn.

- The inelastic lateral-torsional buckling of a web-tapered beam is governed by yielding of the section whose twist displacement is greatest.
- The buckling strength of tapered beams is proportional to the web taper constant α_w . Moreover, the effect of α_w on the buckling strength is most significant in intermediate and stocky web-tapered beams under uniform bending moment ($\beta = -1$). Nevertheless, the normalised buckling resistances tend to become independent of α_w when the beam slenderness increases.

- The buckling resistance of web-tapered beams is noticeably affected by the residual stress distributions in the flange rather than those in the web.
- The normalised buckling resistance increases when increasing the flange-width of web-tapered beams and the coupling of flange compactness and the web-taper constant α_w is seemingly insignificant.
- Both the EC3 and AS4100 provisions are conservative for web-tapered HSS beams subject to uniform moment bending as the smallest taper section is taken for calculating the nominal moment capacity. The beam curve (c) of the EC3 limited method approximates a lower bound of the normalised buckling strength of web-tapered HSS beams under moment gradient, whilst the mean of the FE predictions is obtained by using the proposed formula for the buckling load carrying capacity of HSS flexural members with respect to AS4100 method.

6.2. Recommendations for future research

During the laboratory experiments and parametric studies undertaken in this thesis, some details which may be useful for further research were identified, and several areas of high-strength steel structures can be developed in future work. The following might be of significance on the topic.

- A general formulation of the material coefficient γ_m (Section 4.6) with respect to different steel material properties is a research interest.
- The EC3 (2005) and AS4100-1998 (2016) provisions are too conservative for web-tapered beams under uniform bending moment. Alternative design methods based on the first yield criterion have been proposed (Marques *et al.*, 2012; Marques *et al.*, 2013; Tankova *et al.*, 2018b). However, further

experiments and analytical investigations are needed to evaluate the effects of load and restraint arrangements, material and geometric imperfections, and the variation of the steel materials on the buckling resistance of tapered steel beams.

- Very few studies on the stability of monosymmetric and/or hybrid flexural members fabricated from HSS plates appear in the literature, and research work is therefore needed.
- In the advanced analysis which accounts for the performance of the entire structure by involving the global frame and member instabilities the geometric (i.e. $P-\Delta$ and $P-\delta$ effects) and material (i.e. $\sigma-\varepsilon$ relation) nonlinearities are the key factors. Research efforts (Yun and Gardner, 2017; Shi *et al.*, 2016) have been undertaken to refine the constitutive models of steel materials which allow yielding and strain hardening, and the structural analysis of steel frames incorporating these proposed models have been presented (Gardner *et al.*, 2019; Kucukler and Gardner, 2018). Unfortunately, the analysis of steel frames incorporating HSS members has received little attention, and in particular no research studies of steel frames with tapered HSS members can be found.

REFERENCES

- AASHTO (2016). “AASHTO LRFD Bridge design specifications, 7th Edition”, American Association of State Highway and Transportation Officials, Washington, DC.
- Abambres M. and Quach W.-M. (2016). “Residual stresses in steel members: a review of available analytical expressions”, *International Journal of Structural Integrity* 7(1): 70-94.
- ABAQUS (2014). “ABAQUS, Version 6.14 Documentation”, Dassault Systemes Simulia Corporation, Providence, RI.
- Alipooramirabad H., Paradowska A., Ghomashchi R. and Reid M. (2017). “Investigating the effects of welding process on residual stresses, microstructure and mechanical properties in HSLA steel welds”, *Journal of Manufacturing Processes* 28: 70-81.
- Allen A., Hutchings M., Windsor C. and Andreani C. (1985). “Neutron diffraction methods for the study of residual stress fields”, *Advances in Physics* 34(4): 445-473.
- Andrade A. and Camotim D. (2005). “Lateral–torsional buckling of singly symmetric tapered beams: theory and applications”, *Journal of Engineering Mechanics, ASCE* 131(6): 586-597.
- ANSI/AISC (2016). “ANSI/AISC360-16. Specification for Structural Steel Buildings”, American Institute of Steel Construction, Chicago, IL.

ArcelorMittal <https://corporate.arcelormittal.com/news-and-media/our-stories/s31-infrastructure-of-modern-life-1h1star>.

AWS (2015). “A5.28/A5.28M:2005 (R2015) Specification for Low-Alloy Steel Electrodes and Rods for Gas Shielded Arc Welding”, American Welding Society, Miami, FL.

Ban H. and Shi G. (2017). “A review of research on high-strength steel structures”, Proceedings of the Institution of Civil Engineers-Structures and Buildings: 1-17.

Ban H., Shi G., Bai Y., Shi Y. and Wang Y. (2013a). “Residual stress of 460 MPa high strength steel welded I section: experimental investigation and modelling”, International Journal of Steel Structures 13(4): 691-705.

Ban H., Shi G., Shi Y. and Bradford M. A. (2013b). “Experimental investigation of the overall buckling behaviour of 960MPa high strength steel columns”, Journal of Constructional Steel Research 88: 256-266.

Ban H., Shi G., Shi Y. and Wang Y. (2011). “Research progress on the mechanical property of high strength structural steels”, Advanced Materials Research, Trans Tech Publ.

Barroso A., Cañas J., Picón R., París F., Méndez C. and Unanue I. (2010). “Prediction of welding residual stresses and displacements by simplified models. Experimental validation”, Materials & Design 31(3): 1338-1349.

Beg D. and Hladnik L. (1996). “Slenderness limit of class 3 I cross-sections made of high strength steel”, Journal of Constructional Steel Research 38(3): 201-217.

- Bild S. and Trahair N. S. (1989). "In-plane strengths of steel columns and beam-columns", *Journal of Constructional Steel Research* 13(1): 1-22.
- Bjorhovde R. (2004). "Development and use of high-performance steel", *Journal of Constructional Steel Research* 60(3): 393-400.
- Bradford M. A. and Cuk P. E. (1988a). "Elastic buckling of tapered monosymmetric I-beams", *Journal of Structural Engineering ASCE* 114(5): 977-996.
- Bradford M. A. (1988b). "Stability of tapered I-beams", *Journal of Constructional Steel Research* 9(3): 195-216.
- Bradford M. A. and Liu X. (2016). "Flexural-torsional buckling of high-strength steel beams", *Journal of Constructional Steel Research* 124: 122-131.
- Bradford M. A. and Trahair N. S. (1985). "Inelastic buckling of beam-columns with unequal end moments", *Journal of Constructional Steel Research* 5(3): 195-212.
- Bradford M. A. (2006). "Lateral buckling of tapered steel members", Chapter 1 of *Analysis and design of plated structures., Vol 1 Stability*. NE Shanmugam and CM Wang (eds.), Woodhead Publishing Limited, 1-25; 2006.
- British Standards Institute (2000). "BS5950-2000 Structural use of Steelwork in Building", BSI, London.
- Brown P. T. and Trahair N. S. (1968). "Finite integral solution of differential equations", *Civil Engineering Transactions, Institution of Engineers Australia* CE10:193-196.
- Brown T. G. (1981). "Lateral-torsional buckling of tapered I-beams", *Journal of the Structural Division, ASCE* 107(4): 689-697.

Dux P. F. and Kitipornchai S. (1983). "Inelastic beam buckling experiments", *Journal of Constructional Steel Research* 3(1): 3-9.

Earls C. (1999). "On the inelastic failure of high-strength steel I-shaped beams", *Journal of Constructional Steel Research* 49(1): 1-24.

EN1993-1-1:2005 (2005). "Eurocode 3: Design of Steel Structures - Part 1-1: General Rules and Rules for Building", BSI, London.

ECCS, B. (1976). "Manual on Stability of Steel Structures", European Convention for Constructional Steelwork, Brussels, Belgium.

Fitzpatrick M. E. and Lodini A. (2003). "Analysis of Residual Stress by Diffraction using Neutron and Synchrotron Radiation", CRC Press, Boca Raton, FL.

Galambos T. V., Hajjar J., Earls C. J. and Gross J. L. (1997). "Required properties of high-performance steels", Technical report NISTIR 6004. National Institute of Standards and Technology, Gaithersburg, MD.

Galambos T. V. and Ketter R. L. (1959). "Columns under combined bending and thrust", *Transactions of the American Society of Civil Engineers* 126(1): 1-23.

Green P. S., Sause R. and Ricles J. M. (2002). "Strength and ductility of HPS flexural members", *Journal of Constructional Steel Research* 58(5-8): 907-941.

Hutchings M. T., Withers P. J., Holden T. M. and Lorentzen T. (2005). "Introduction to the Characterization of Residual Stress by Neutron Diffraction", CRC Press, Boca Raton, FL.

ISO (2005). “ISO/TS21432:2005 (R2010) Non-Destructive Testing-Standard Test Method for Determining Residual Stresses by Neutron Diffraction”, International Organization for Standardization, Geneva.

Johansson B. and Collin P. (2005). “Eurocode for high strength steel and applications in construction. In: Super-high strength steels”, International Conference Super-High Strength Steels, Rome.

Kaehler R. C., White D. W. and Kim Y. D. (2011). “Frame design using web-tapered members”, American Institute of Steel Construction, Chicago, IL.

Kang, S.-B., Yang B., Zhang Y., Elchalakani M. and Xiong G. (2018). “Global buckling of laterally-unrestrained Q460GJ beams with singly symmetric I-sections”, *Journal of Constructional Steel Research* 145: 341-351.

Kato B. (1990). “Deformation capacity of steel structures”, *Journal of Constructional Steel Research* 17(1-2): 33-94.

Kern A., Niessen T., Schriever U. and Tschersich H.-J. (2005). “Production and properties of thermomechanically rolled high strength steel plates with minimum yield strengths up to 700 MPa”, *Ironmaking & Steelmaking* 32(4): 331-336.

Khan M., Paradowska A., Uy B., Mashiri F. and Tao Z. (2016). “Residual stresses in high strength steel welded box sections”, *Journal of Constructional Steel Research* 116: 55-64.

Kitipornchai S. and Trahair N. S. (1972). “Elastic stability of tapered I-beams”, *Journal of the Structural Division, ASCE* 98: 713-728.

- Kitipornchai S. and Trahair N. S. (1975). "Elastic behavior of tapered monosymmetric I-beams", *Journal of the Structural Division, ASCE* 101: 1661-1678.
- Kucukler M. and Gardner L. (2018). "Design of laterally restrained web-tapered steel structures through a stiffness reduction method", *Journal of Constructional Steel Research*, 141, 63-76.
- Lee C.-H., Han K.-H., Uang C.-M., Kim D.-K., Park C.-H. and Kim J.-H. (2012). "Flexural strength and rotation capacity of I-shaped beams fabricated from 800-MPa steel", *Journal of Structural Engineering, ASCE* 139(6): 1043-1058.
- Lee G. and Morrell M. (1975). "Application of AISC design provisions for tapered members", *Engineering Journal, AISC* 12(1): 1-13.
- Lee G. C., Morrell M. and Ketter R. L. (1971). "Design of Tapered Members", State Univ of New York Buffalo Dept of Civil Engineering, Buffalo, NY.
- Lee G. C. and Szabo B. A. (1967). "Torsional response of tapered I-girders", *Journal of the Structural Division, ASCE* 93(5): 233-252.
- Lee L. H. (1956). "Non-uniform torsion of tapered I-beams", *Journal of the Franklin Institute* 262(1): 37-44.
- Gardner L., Yun X., Fieber A. and Macorini L. (2019). "Steel design by advanced analysis: material modeling and strain limits", *Engineering*, 5(2): 243-249.
- Li T.-J., Li G.-Q. and Wang Y.-B. (2015). "Residual stress tests of welded Q690 high-strength steel box-and H-sections", *Journal of Constructional Steel Research* 115: 283-289.

Marques L., da Silva L. S., Greiner R., Rebelo C. and Taras A. (2013). “Development of a consistent design procedure for lateral–torsional buckling of tapered beams”, *Journal of Constructional Steel Research* 89: 213-235.

Marques L., Taras A., da Silva L. S., Greiner R. and Rebelo C. (2012). “Development of a consistent buckling design procedure for tapered columns”, *Journal of Constructional Steel Research* 72: 61-74.

McDermott J. F. (1969). “Plastic bending of A514 steel beams”, *Journal of the Structural Division, ASCE* 95(9): 1851-1871.

Miki C., Homma K. and Tominaga T. (2002). “High-strength and high-performance steels and their use in bridge structures”, *Journal of Constructional Steel Research* 58(1): 3-20.

Morrell M. and Lee G. (1974). “Allowable stresses for web-tapered beams with lateral restraints”, *Welding Research Council Bulletin No. 192*: 1-12.

Nishino F. and Tall L. (1970). “Experimental investigation of the strength of T-1 steel columns”, Fritz Engineering Laboratory, Department of Civil Engineering, Lehigh University, Bethlehem, PA.

Noyan I. C. and Cohen J. B. (1987). “Residual Stress: Measurement by Diffraction and Interpretation”, Springer, New York.

Odar E. and Nishino F. (1965). “Residual stresses in welded built-up T-1 shapes”, October 1965, Reprint No. 320 (67-3), Fritz Laboratory Report, Lehigh University, Bethlehem, PA

Paradowska A. M., Price J. W., Finlayson T. R., Lienert U. and Ibrahim R. (2010).

“Comparison of neutron and synchrotron diffraction measurements of residual stress in bead-on-plate weldments”, *Journal of Pressure Vessel Technology* 132(1): 011502.

Pocock G. (2006). “High strength steel use in Australia, Japan & the US”, *The Structural Engineer* 84(21): 27-31.

Prawel S., Morrell M. and Lee G. (1974). “Bending and buckling strength of tapered structural members”, *Welding Journal* 53(2): 75-84.

Rasmussen K. J. R. and Hancock G. J. (1992). “Plate slenderness limits for high strength steel sections”, *Journal of Constructional Steel Research* 23(1-3): 73-96.

Rasmussen K. J. R. and Hancock G. J. (1995). “Tests of high strength steel columns”, *Journal of Constructional Steel Research* 34(1): 27-52.

Ricles J. M., Sause R. and Green P. S. (1998). “High-strength steel: implications of material and geometric characteristics on inelastic flexural behaviour”, *Engineering Structures* 20(4-6): 323-335.

Ronagh H. and Bradford M. A. (1996). “A rational model for the distortional buckling of tapered members”, *Computer Methods in Applied Mechanics and Engineering* 130(3): 263-277.

Ronagh H., Bradford M. A. and Attard M. (2000a). “Nonlinear analysis of thin-walled members of variable cross-section. Part I: Theory”, *Computers & Structures* 77(3): 285-299.

- Ronagh H., Bradford M. A. and Attard M. (2000b). “Nonlinear analysis of thin-walled members of variable cross-section. Part II: Application”, *Computers & Structures* 77(3): 301-313.
- Schajer G. S. (2013). “Practical residual stress measurement methods”, John Wiley & Sons, New York, NY.
- Schröter F. (2006). “Trends of using high-strength steel for heavy steel structures”, Dillinger Hüttenwerke, Germany.
- Shayan S., Rasmussen K. J. R. and Zhang H. (2014). “Probabilistic modelling of residual stress in advanced analysis of steel structures”, *Journal of Constructional Steel Research* 101: 407-414.
- Shi G., Zhu X. and Ban H. (2016). “Material properties and partial factors for resistance of high-strength steels in China”, *Journal of Constructional Steel Research*, 121, 65-79.
- Shikanai N., Mitao S. and Endo S. (2008). “Recent development in microstructural control technologies through the thermo-mechanical control process (TMCP) with JFE steel’s high-performance plates”, *JFE technical report* 11(6): 1-6.
- Shiomi H. and Kurata M. (1984). “Strength formula for tapered beam-columns”, *Journal of Structural Engineering, ASCE* 110(7): 1630-1643.
- Shokouhian M. and Shi Y. (2015). “Flexural strength of hybrid steel I-beams based on slenderness”, *Engineering Structures* 93: 114-128.
- Shokouhian M., Shi Y. and Head M. (2016). “Interactive buckling failure modes of hybrid steel flexural members”, *Engineering Structures* 125: 153-166.

Standards Australia (2007). “AS1391-2007 Metallic materials-tensile testing at ambient temperature”, SA, Sydney.

Standards Australia (2010). “AS/NZS1554.4-2010 Welding of high strength quenched and tempered steels”, SA, Sydney.

Standards Australia (2016). “AS4100-1998 (R2016) Steel structures”, SA, Sydney.

Subramanian L. and White D. W. (2016a). “Reassessment of the lateral torsional buckling resistance of I-section members: Uniform-moment studies”, *Journal of Structural Engineering*, ASCE 143(3): 04016194.

Subramanian L. and White D. W. (2016b). “Reassessment of the lateral torsional buckling resistance of rolled I-section members: Moment gradient tests”, *Journal of Structural Engineering*, ASCE 143(4): 04016203.

Subramanian L. and White D. W. (2017). “Resolving the disconnects between lateral torsional buckling experimental tests, test simulations and design strength equations”, *Journal of Constructional Steel Research* 128: 321-334.

Suzuki T., Ogawa T. and Ikarashi K. (1994). “A study on local buckling behavior of hybrid beams”, *Thin-Walled Structures* 19(2-4): 337-351.

Tankova T., da Silva L. S. and Marques L. (2018a). “Buckling resistance of non-uniform steel members based on stress utilization: General formulation”, *Journal of Constructional Steel Research* 149: 239-256.

Tankova T., Martins J. P., da Silva L. S., Marques L., Craveiro H. D. and Santiago A. (2018b). "Experimental lateral-torsional buckling behaviour of web tapered I-section steel beams", *Engineering Structures* 168: 355-370.

Taylor J. (1997). "Introduction to Error Analysis, the Study of Uncertainties in Physical Measurements", University Science Books, New York.

Trahair N. S. (2014). "Interaction buckling of tapered beams", *Engineering Structures* 62: 174-180.

Trahair N. S. (2017). "Lateral buckling of tapered members", *Engineering Structures* 151: 518-526.

Trahair N. S. and Ansourian P. (2016). "In-plane behaviour of web-tapered beams", *Engineering Structures* 108: 47-52.

Trahair N. S. and Bradford M. A. (1998). "Behaviour and Design of Steel Structures to AS4100, Third edition - Australian", Taylor and Francis, London.

Trahair N. S., Bradford M. A., Nethercot D. and Gardner L. (2007). "The Behaviour and Design of Steel Structures to EC3", CRC Press, London.

Trahair N. S. and Kitipornchai S. (1971). "Elastic lateral buckling of stepped I-beams", *Journal of the Structural Division, ASCE* 97(10): 2535-2548.

Wang Y.-B., Li G.-Q. and Chen S.-W. (2012). "Residual stresses in welded flame-cut high strength steel H-sections", *Journal of Constructional Steel Research* 79: 159-165.

Willms R. (2009). "High strength steel for steel constructions", Nordic Steel Construction Conference-NSCC, Malmo, Sweden.

Withers P. J. and Bhadeshia H. K. D. H (2001). “Residual stress. Part 1–measurement techniques”, *Journal of Materials Science and Technology* 17(4): 355-365.

Xiong G., Kang S.-B., Yang B., Wang S., Bai J., Nie S., Hu Y. and Dai G. (2016). “Experimental and numerical studies on lateral torsional buckling of welded Q460GJ structural steel beams”, *Engineering Structures* 126: 1-14.

Yang B., Kang S.-B., Xiong G., Nie S., Hu Y., Wang S., Bai J. and Dai G. (2017). “Experimental and numerical study on lateral-torsional buckling of singly symmetric Q460GJ steel I-shaped beams”, *Thin-Walled Structures* 113: 205-216.

Yang B., Nie S., Xiong G., Hu Y., Bai J., Zhang W. and Dai G. (2016). “Residual stresses in welded I-shaped sections fabricated from Q460GJ structural steel plates”, *Journal of Constructional Steel Research* 122: 261-273.

Yang B., Xiong G., Nie S., Elchalakani M. and Zhu Q. (2018). “Experimental and model investigation on residual stresses in Q460GJ thick-walled I-shaped sections”, *Journal of Constructional Steel Research* 145: 489-503.

Yang Y.-B. and Yau J.-D. (1987). “Stability of beams with tapered I-sections”, *Journal of Engineering Mechanics ASCE* 113(9): 1337-1357.

Young B. (1972). “Residual stress in hot-rolled members”, *International Colloquium on Column Strength, IABSE, Paris*.

Yun X. and Gardner L. (2017). “Stress-strain curves for hot-rolled steels”, *Journal of Constructional Steel Research*, 133, 36-46.

Zhang L. and Tong G. S. (2008). "Lateral buckling of web-tapered I-beams: A new theory", *Journal of Constructional Steel Research* 64(12): 1379-1393.

Zhu Q., Nie S., Yang B., Xiong G. and Dai G. (2017). "Experimental Investigation on Residual Stresses in Welded Medium-Walled I-shaped Sections Fabricated from Q460GJ Structural Steel Plates", *World Academy of Science, Engineering Technology, International Journal of Civil, Environmental, Structural, Construction Architectural Engineering* 11(11): 1452-1461.

Ziemian R. D. (2010). "Guide to Stability Design Criteria for Metal Structures", John Wiley & Sons, New York.